



저작자표시-비영리-변경금지 2.0 대한민국

이용자는 아래의 조건을 따르는 경우에 한하여 자유롭게

- 이 저작물을 복제, 배포, 전송, 전시, 공연 및 방송할 수 있습니다.

다음과 같은 조건을 따라야 합니다:



저작자표시. 귀하는 원저작자를 표시하여야 합니다.



비영리. 귀하는 이 저작물을 영리 목적으로 이용할 수 없습니다.



변경금지. 귀하는 이 저작물을 개작, 변형 또는 가공할 수 없습니다.

- 귀하는, 이 저작물의 재이용이나 배포의 경우, 이 저작물에 적용된 이용허락조건을 명확하게 나타내어야 합니다.
- 저작권자로부터 별도의 허가를 받으면 이러한 조건들은 적용되지 않습니다.

저작권법에 따른 이용자의 권리는 위의 내용에 의하여 영향을 받지 않습니다.

이것은 [이용허락규약\(Legal Code\)](#)을 이해하기 쉽게 요약한 것입니다.

[Disclaimer](#)

**Ph.D. Dissertation of Engineering**

**High-Voltage High-Frequency  
Pulsed Field Ablation for the Treatment of  
Locally Advanced Solid Tumor**

국소진행성 고형암 치료를 위한  
고전위 고주파 전기 펄스 자극

**February, 2022**

**by**

**Seung Jeong**

**Graduate School of Seoul National University  
Biosystems Engineering**

# High-Voltage High-Frequency Pulsed Field Ablation for the Treatment of Locally Advanced Solid Tumor

Advisor: Prof. Jong Hoon Chung

Submitting a Ph.D. Dissertation  
of Public Administration

February 2022

Graduate School of Seoul National University  
Biosystems Engineering

Seung Jeong

Confirming the Ph.D. Dissertation written by  
Seung Jeong

Chair	<u>Ghiseok Kim</u>	(Seal)
Vice Chair	<u>Jong Hoon Chung</u>	(Seal)
Examiner	<u>Hoon Seonwoo</u>	(Seal)
Examiner	<u>Kyoung-Je Jang</u>	(Seal)
Examiner	<u>Pankaj Garg</u>	(Seal)

## Abstract

Pulsed field ablation (PFA), a focal tissue ablation method, uses short high electric pulses resulting in cell death in target tissue by irreversibly permeabilizing the cell membrane. Unlike other focal ablation modalities such as radiofrequency ablation (RFA), microwave, high intensity focused ultrasound (HIFU), and cryoablation, PFA is a non-thermal ablation sparing extracellular matrix (ECM), vasculature, nerves, and ductal networks, which results in rapid tissue regeneration and preservation of tissue function. Therefore, PFA is presented to be an alternative instead of other thermal focal ablation modalities or adjuvant therapy of chemotherapy for locally advanced solid tumor (LAST) such as locally advanced pancreatic cancer (LAPC), locally advanced prostate cancer (LAPRC), and hepatocellular carcinoma (HCC). Most of the research was focused on clinical and preclinical trials with low-frequency pulsed field ablation (LF-PFA). However, few studies have been approached from a tissue engineering perspective based on decellularization and recellularization to investigate tissue scaffold fabrication and tissue regeneration using high-frequency pulsed field ablation (HF-PFA).

In this dissertation, we developed a method to evaluate the electroporated area by PFA in an *in-vitro* model to prescreen the optimal conditions to successfully ablate LAST without margin live cells. Also, we fabricated HF-PFA derived tissue scaffold in the *in-vitro* 3D culture model and utilized the perfusion bioreactor system to observe tissue regeneration on the decellularized scaffold. HF-PFA generator and electrodes system were manufactured by The Standard Co., Ltd (Gunpo-si, Korea). Cell apoptosis of human prostate cancer tissue was studied using HF-PFA. Finally, the decellularization and tissue regeneration process after HF-PFA were reconfirmed in the *in-vivo* experiment using

prostate tissue of canine. The hypothesis underlying my research is that HF-PFA can (i) fabricate decellularized tissue scaffold to ablate LAST with cell apoptosis, and (ii) provide the environments for rapid and proper tissue regeneration.

The main results of my dissertation research can be summarized as follows. First, a novel evaluation method was developed to evaluate electroporated areas caused by HF-PFA on the potato model. It takes about 12 hours to evaluate the HF-PFA ablated areas using a common method of polyphenol oxidation. Using our 2,3,5-triphenyltetrazolium chloride (TTC) method, the electroporated areas can be assessed within 3 hours and reversibly electroporated areas also can be observed, which makes it possible to predict the HF-PFA affected zone in the drug delivery or gene transfection research field. The various HF-PFA conditions such as voltage, pulse number, pulse width, pulse interval for *in-vitro*, *in-vivo* studies were indirectly performed and prescreened using the TTC method on the potato model. Second, an *in-vitro* 3D culture model of cancer cells was constructed using agarose gel to investigate the tissue scaffold and regeneration ability of HF-PFA based on a tissue engineering perspective. Decellularization was induced by HF-PFA on the gel and regeneration was induced by perfusion bioreactor with adipose-derived mesenchymal stem cells (ADMSC). Decellularization was evaluated using a live and dead cell assay kit with a fluorescence microscope and hematoxylin and eosin (H&E). Nerve regeneration was evaluated using immunocytochemistry (ICC) of Tuj1. Third, cell apoptosis of human prostate cancer tissue was studied using HF-PFA. Human prostate cancer tissues were induced on the skin of the nude mouse and HF-PFA was performed on the cancer tissue with monopolar electrodes. The cell apoptosis markers, cleaved caspase-3, and BCL-2 were upregulated after HF-PFA with the weight of cancer tissue decreasing over time. HF-PFA had an effect to induce cell apoptosis and reduce the mass of cancer

tissue. Finally, the decellularization and tissue regeneration process after HF-PFA were investigated in the *in-vivo* experiment using prostate tissue of canine. Cell apoptosis and decellularization process was maximized 4 hours after HF-PFA and the recellularization was observed 7 days after HF-PFA. The prostate tissue was almost regenerated with minor fibrosis at 4 weeks.

In the results, HF-PFA successfully fabricated decellularized tissue scaffold to ablate LAST with cell apoptosis and provided the environments for rapid and proper tissue regeneration. Therefore, HF-PFA can be utilized in the field of tissue engineering and regenerative medicine and promotes the rapid and accurate ablation of LAST in clinical surgery to enhance the quality of life.

**Keywords:** High-frequency Pulsed field ablation, Locally advanced solid tumor, Decellularization, Tissue regeneration

**Student Number:** 2013-23254

# Table of contents

<b>Abstract</b>	iii
<b>Table of contents</b>	vi
<b>Nomenclature</b>	viii
<b>List of Tables</b>	x
<b>List of Figures</b>	xi
<b>Chapter 1. Introduction</b> .....	1
1.1 Background.....	1
1.2 Objectives .....	2
<b>Chapter 2. Pulsed field ablation for treatment of locally advanced solid tumor</b> .....	4
2.1 Background of pulsed field ablation.....	4
2.1.1 Historical background .....	5
2.1.2 Theoretical background .....	7
2.2 Pulsed field ablation for tissue engineering.....	10
2.3 Clinical applications of pulsed field ablation for treatment of locally advanced solid tumor.....	12
2.3.1 Locally advanced pancreatic cancer .....	12
2.3.2 Locally advanced prostate cancer.....	15
2.3.3 Locally advanced hepatocellular carcinoma.....	17
<b>Part I: DESIGNING EVALUATION METHOD OF PULSED FIELD ABLATED AREA</b> .....	19
<b>Chapter 3. Evaluation of electroporated area using 2,3,5-triphenyltetrazolium chloride in a potato model</b> .....	20
3.1 Summary.....	20
3.2 Introduction .....	21
3.3 Materials and Methods .....	22
3.4 Results .....	26
3.5 Discussion.....	30
<b>Part II: HIGH-FREQUENCY PULSED FIELD ABLATION FOR IN-VITRO 3D TISSUE SCAFFOLD</b> .....	51
<b>Chapter 4. Fabrication of decellularized 3D tissue scaffold using high-frequency pulsed field ablation</b> .....	52

4.1 Summary.....	52
4.2 Introduction .....	53
4.3 Materials and Methods .....	54
4.4 Results .....	57
4.5 Discussion.....	60
<b>Part III: HIGH-FREQUENCY PULSED FIELD ABLATION FOR IN-VIVO TISSUE SCAFFOLD.....</b>	<b>72</b>
<b>Chapter 5. Decellularization of the human prostate cancer using high-frequency pulsed field ablation.....</b>	<b>73</b>
5.1 Summary.....	73
5.2 Introduction .....	74
5.3 Materials and Methods .....	75
5.4 Results .....	79
5.5 Discussion.....	80
<b>Chapter 6. Decellularization of the beagle prostate using high-frequency pulsed field ablation and tissue regeneration.....</b>	<b>88</b>
6.1 Summary.....	88
6.2 Introduction .....	89
6.3 Materials and Methods .....	91
6.4 Results .....	96
6.5 Discussion.....	100
<b>Chapter 7. Conclusions.....</b>	<b>122</b>
<b>Abstract (Korean).....</b>	<b>124</b>
<b>References.....</b>	<b>127</b>



## Nomenclature

LAST	Locally advanced solid tumor
LAPC	Locally advanced pancreatic cancer
PDAC	Pancreatic ductal adenocarcinoma
LAPRC	Locally advanced prostate cancer
HCC	Hepatocellular carcinoma
PEF	Pulsed electric field
msPEF	Millisecond pulsed electric field
$\mu$ sPEF	Microsecond pulsed electric field
nsPEF	Nanosecond pulsed electric field
PFA	Pulsed field ablation
LF-PFA	Low-frequency pulsed field ablation
HF-PFA	High-frequency pulsed field ablation
RFA	Radiofrequency ablation
HIFU	High intensity focused ultrasound
IRE	Irreversible electroporation
RE	Reversible electroporation
NTIRE	Nonthermal irreversible electroporation
H-FIRE	High-frequency irreversible electroporation
TMP	Transmembrane potential
ECM	Extracellular matrix
TTC	2,3,5-triphenyltetrazolium chloride
MRI	Magnetic resonance imaging
TEM	Transmission electron microscopy
ADMSC	Adipose derived mesenchymal stem cell
FACS	Fluorescence-activated cell sorting

PI	Propidium iodide
VSMC	Vascular smooth muscle cell
SMA	Smooth muscle actin
ECG	Electrocardiography
BrdU	Bromodeoxyuridine
H&E	Hematoxylin and eosin
IHC	Immunohistochemistry

## List of Tables

Table 2.1	Overall survival after pulsed field ablation for locally advanced pancreatic cancer	18
Table 2.2	Clinical and preclinical studies of pulsed field ablation for locally advanced prostate cancer	20
Table 2.3	Clinical and preclinical studies of pulsed field ablation for locally advanced hepatocellular carcinoma	22
Table 3.S1	Conductivity change rate before and after IRE treatment on potato at various voltage conditions depending on the frequency	50
Table 4.1	Geometrical parameters of the 3D gel with the electrodes and physical parameters of the pulsed field ablation model for COMSOL simulation	70
Table 4.2	Material properties of the 3D gel for COMSOL simulation	71
Table 5.1	Electrical ablation conditions for the HF-PFA of human prostate cancer tissue on the nude mouse skin	83
Table 6.1	Electrical conditions of HF-PFA to ablate the beagle prostate tissue	104
Table 6.2	Geometrical parameters of the beagle prostate with the electrodes and physical parameters of the HF-PFA for COMSOL simulation	107
Table 6.3	Material properties of the beagle prostate for COMSOL simulation	108

# List of Figures

Figure 1.1	Schematic representation of the decellularization and tissue regeneration after HF-PFA	3
Figure 2.1	Historical background of pulsed field ablation	8
Figure 2.2	Schematic of electroporation using pulsed field ablation at intact cell membrane to induce cell apoptosis	10
Figure 2.3	Elements of tissue engineering; biomaterials, cells and signals	13
Figure 2.4	Smooth muscle cell removal after PFA on the carotid artery	14
Figure 3.1	Experimental setup for comparing melanin accumulation and TTC staining methods	40
Figure 3.2	Comparison of melanin accumulation and TTC staining area over time	41
Figure 3.3	Comparison of pulsed electric field ablation area between melanin accumulation and TTC staining on the various conditions	43
Figure 3.4	Electrical current and conductivity changes after pulsed electric field ablation	44
Figure 3.5	IRE-ablated area at different staining times after pulsing.	45
Figure 3.6	TEM analysis of TTC-unstained and TTC-stained areas after pulsing on the potato tissue	46
Figure 3.7	Correlation among electrical properties and each staining method	47
Figure 3.8	The extent to which the IRE-ablated area is affected by the inner tissue inside the potato	48
Figure 3.S1	Preconditioning for pulse conditions of voltage, pulse numbers	51
Figure 3.S2	Preconditioning for pulse conditions of pulse delay	51
Figure 3.S3	TEM analysis of non-pulsed perimedullar zone with evident electron-dense line (arrows) along the cell wall (CW)	52
Figure 3.S4	TEM analysis of pulsed TTC-unstained medullar zone with no electron-dense line along with the CW	53
Figure 3.S5	TEM analysis of pulsed TTC-stained deep red inner medullar zone with partially continuous electron-dense lines along with the CW	54
Figure 4.1	Simulation of electric field by pulsed field ablation at the 3D gel model in the COMSOL Multiphysics 5.6	65
Figure 4.2	Simulation of electric field by pulsed field ablation at the 3D agarose gel model in the COMSOL Multiphysics 5.6	66
Figure 4.3	Simulation of thermal distribution by pulsed field ablation at the 3D agarose gel model in the COMSOL Multiphysics 5.6	67
Figure 4.4	FACS results to compare the cell death rate of LF-PFA and HF-PFA at various applied voltages using PI	72
Figure 4.5	FACS results to compare the death rate of 1500 V/cm PFA at various frequencies voltages using FITC dextran 10kDa and Annexin V/PI	73
Figure 4.6	Calcein AM, PI fluorescence after various pulsed field ablation and histogram of the PI stained area	74

Figure 4.7	H&E of cancer cell on the 3D gel model after pulsed field ablation	75
Figure 4.8	Tuj1, DAPI fluorescence image to detect neurogenic marker, beta-III tubulin after pulsed field ablation on the 3D gel model	76
Figure 5.1	Schematic of HF-PFA of human prostate cancer cells on the nude mouse skin	82
Figure 5.2	Tumor volume and weight changes over time after HF-PFA treatment at various conditions	84
Figure 5.3	TUNEL assay of the human prostate cancer after HF-PFA treatment	85
Figure 5.4	Western blot results of cleaved caspase-3, Bcl-2 after HF-PFA	86
Figure 5.5	Temperature change during the HF-PFA on the human prostate cancer tissue on nude mouse skin	87
Figure 6.1	Schematic of the HF-PFA treatment to the beagle prostate tissue	103
Figure 6.2	Simulation of electric field by HF-PFA at the prostate model in the COMSOL Multiphysics 5.6	105
Figure 6.3	Simulation of electric field by HF-PFA at the prostate model in the COMSOL Multiphysics 5.6	106
Figure 6.4	Current, electrical conductivity changes of the prostate and ECG of the beagles after HF-PFA	109
Figure 6.5	Location of tissue samples and gross changes of the prostate after HF-PFA over time	110
Figure 6.6	Gross and histological findings of the prostate after HF-PFA over time	111
Figure 6.7	Changes in TUNEL stained areas after HF-PFA over time	112
Figure 6.8	Detailed comparison of histological findings to compare ablation area	113
Figure 6.9	Preservation of urethra tissue after HF-PFA	114
Figure 6.10	Preservation of prostatic gland and vessels after HF-PFA	115
Figure 6.11	Regeneration of the urothelium cells after HF-PFA	116
Figure 6.12	Regeneration of the prostatic gland after HF-PFA	117
Figure 6.13	Changes in the fibrotic area after HF-PFA over time	118
Figure 6.14	Fibrotic areas around the urethra after HF-PFA over time	119
Figure 6.15	Fibrotic areas around the HF-PFA treated area over time	120
Figure 6.16	Biochemistry of the beagles after HF-PFA over time	121

# Chapter 1. Introduction

## 1.1 Background

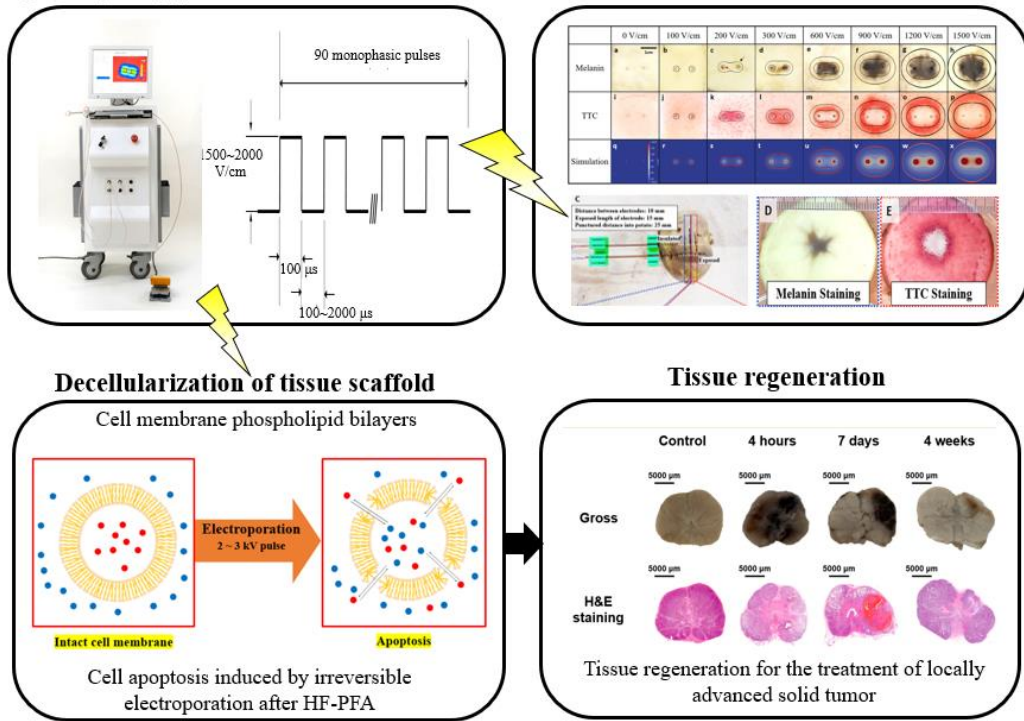
Pulsed field ablation (PFA), a non-thermal focal tissue ablation modality, uses ultrashort high electric pulses resulting in cell apoptosis in the target tissue by irreversibly permeabilizing the cellular membrane (Figure 1.1). Unlike other thermal focal ablation modalities (e.g., radiofrequency ablation (RFA), high intensity focused ultrasound (HIFU), microwave and cryoablation), PFA is a non-thermal ablation (  $< 43\text{ }^{\circ}\text{C}$  ) sparing extracellular matrix (ECM), vasculature, nerves and ductal networks, which results in rapid tissue regeneration and preservation of tissue function. Therefore, PFA is suggested to be an alternative instead of other thermal focal ablation modalities or adjuvant therapy of chemotherapy for locally advanced solid tumor (LAST) (e.g., locally advanced pancreatic cancer (LAPC), prostate cancer, and hepatocellular carcinoma (HCC)). Most of the research was focused on clinical and preclinical trials with low-frequency pulsed field ablation (LF-PFA). For example, most of the studies were performed with low-frequency pulse delays ranging from 100 to 1000 ms due to the limitation of the specification of the commercialized pulse generator. However, few studies have been approached from a tissue engineering perspective based on the process of decellularization and recellularization to investigate the tissue scaffold fabrication and tissue regeneration using high-frequency pulsed field ablation (HF-PFA) of hundreds of microsecond pulse delay. The general goal of my doctoral dissertation is therefore to apply HF-PFA for manipulation of decellularized tissue scaffold to accelerate tissue regeneration sparing the ECM for treatment of locally advanced solid tumors in clinical surgery.

## 1.2 Objectives

The working hypothesis underlying my dissertation is that HF-PFA can (i) fabricate decellularized tissue scaffold to ablate LAST with cell apoptosis, and (ii) provide the environments for rapid and proper tissue regeneration of the target region. To address these hypotheses, we developed an *in-vitro* evaluation platform with TTC agents in the potato model. Using this platform in combination with tissue engineering technique, we investigated the optimal conditions of HF-PFA treatment to fabricate decellularized tissue scaffold for the proper ablation of LAST with minimal heat (< 43 °C). Finally, engineered tissue scaffold was recellularized with perfusion bioreactor system resulting in tissue regeneration. The *In-vivo* preclinical model showed similar results after HF-PFA treatment. The specific aims of my dissertation work are as follows:

- Aim 1. To design the evaluation method of HF-PFA with TTC agents in the potato model to investigate the electroporated areas in the treated zones
- Aim 2. To develop strategies for optimal conditions of HF-PFA treatment to fabricate decellularized tissue scaffold for the ablation of LAST
- Aim 3. To investigate the tissue regeneration of the treated area after HF-PFA treatment in the *in-vitro* 3D culture model and *in-vivo* preclinical tissue

**High-frequency pulsed field ablation (HF-PFA) *In-vitro* evaluation platform on the potato**



**Figure 1.1. Schematic representation of the decellularization and tissue regeneration after HF-PFA.**

Pulsed field ablation (PFA) uses short high electric pulses resulting in apoptotic cell death in the target tissue by irreversibly permeabilizing the cell membrane. *In-vitro* HF-PFA ablated area evaluation platform was developed on the potato model. The tissue scaffold was decellularized after HF-PFA sparing extracellular matrix, vessel, and nerve structures, which results in rapid tissue regeneration.



## **Chapter 2. Pulsed field ablation for treatment of locally advanced solid tumor**

Pulsed field ablation (PFA) techniques have been influential in the treatment of locally advanced solid tumors. Here, we describe the historical and theoretical background pulsed field ablation that has contributed to major advances for treating a locally advanced solid tumor. We also discuss the pulsed field ablation for tissue engineering and clinical applications at various indications.

### **2.1 Background of pulsed field ablation**

Pulsed field ablation is a nonthermal local treatment modality for cancer tissue by irreversibly permeabilizing the membrane of the cells in the target tissue. The history of the pulsed field ablation is related to that of electroporation. Electroporation is the phenomenon of increasing cell membrane permeability by exposing cells to ultrashort, high electric field pulses. These pulses cause nano-sized pores in the cell membrane leading to apoptotic cell death. This phenomenon is also called irreversible electroporation (IRE).

IRE is mainly used to destroy undesirable cells such as cancer by inducing apoptotic cell death without thermal damage. Recently, IRE has been adopted as an alternative tool for minimally invasive ablation of cancerous tissue. Therefore, IRE can be also called pulsed field ablation (PFA). The goal of this chapter is to present a historical

and theoretical review of the field of pulsed field ablation from the first reports of the phenomenon in the 18th century to modern applications in minimally invasive surgery.

### **2.1.1 Historical background**

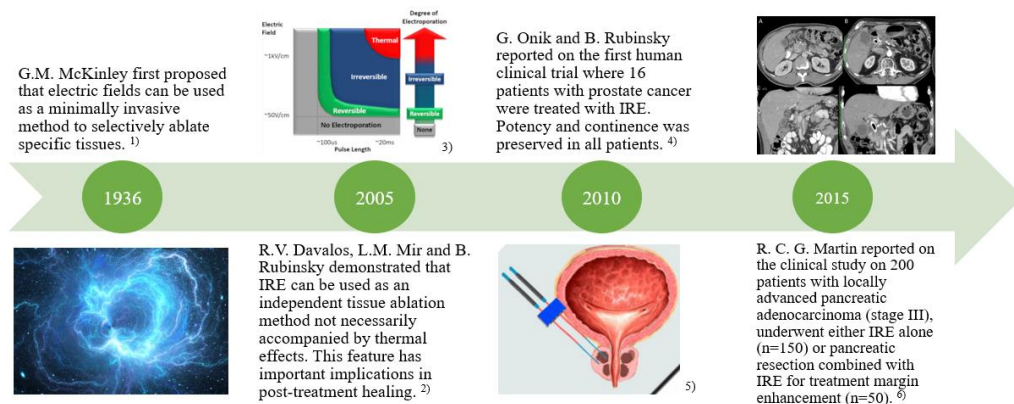
The historical background is summarized in Figure 2.1. The first scientific explanation for a phenomenon suggesting pulsed field ablation in tissues can be found in the previous study in 1764 [1]. In the electric field experiments, J.A. Nollet observed the formation of red spots on the humans and animal skin in areas where an electric spark was applied. The same phenomenon was observed in J.P. Reilly, who reported that red spots may be the result of stratum corneum degradation caused by heat [2]. However, these red spots are most likely caused by pulsed field ablation because erythemas are common when applying electroporation in the skin tissue [4, 5]. In the 1930s, the thermal effects of electric fields on biological materials were well studied [3,4]. The G.M. McKinley in 1936 found that the tissue damage caused by pulsed field ablation with frequency ranging from 10 to 100 MHz cannot be caused only by heat, especially in the case of nerve [5]. He even suggests that an electric field could be used as a selective minimally invasive ablation method for some specific tissues.

R. Davalos and B. Rubinsky proposed the use of IRE with a pulse length longer than 5  $\mu$ s as a tissue ablation method in 2004. [6] They detailed the treatment planning of the electrode configurations and the electrical variables. They also suggested that IRE can be designed to prevent tissue damage caused by heat, resulting in the successful procedural

outcome and rapid healing after treatment [7]. Therefore, IRE is also referred to as non-thermal irreversible electroporation (NTIRE).

G. Onik applied IRE to the canine prostate tissue using percutaneous needle electrodes under ultrasound guidance [8]. The ablation zone was distinct in the macroscopic observation and peripheral structures such as the blood vessels, urethra, nerves, and rectum were preserved after IRE. Onik also performed an *in-vitro* study suggesting that IRE induced the cell death of prostate adenocarcinoma cells [9].

G. Onik and B. Rubinsky reported the first human clinical trial of IRE on prostate cancer in 2010 [10]. They reported that the treatment was successful and the potency and continence were preserved in all patients. R. C. G. Martin reported on the human clinical trial of 200 patients with locally advanced pancreatic cancer (LAPC) [11]. In the study, the conventional chemotherapy combined with IRE resulted in prolonged survival compared to control groups.



**Figure 2.1. Historical background of pulsed field ablation.**

### 2.1.2 Theoretical background

The pulsed electric field causes two types of electroporation of the cell membrane; reversible electroporation (RE) when the formed pores were resealed, and irreversible electroporation (IRE) when the disruption of the cell membrane results in apoptotic cell death (Figure 2.2). In clinical studies, 2~3 kV pulses were applied to destroy the cancerous tissues with the IRE phenomenon.

It was believed that the killing mechanism of IRE was necrosis caused by increased permeability and subsequent destruction of the osmotic balance. In 1999, there were two independent papers indicating the mechanism of cell death was both necrosis and apoptosis through *in-vitro* studies [12,13]. It was found that the necrosis can be avoided through optimization of IRE pulse parameters sparing the nearby tissue structures, such as vessels, nerves, or extracellular matrix, to induce rapid regeneration of tissues.

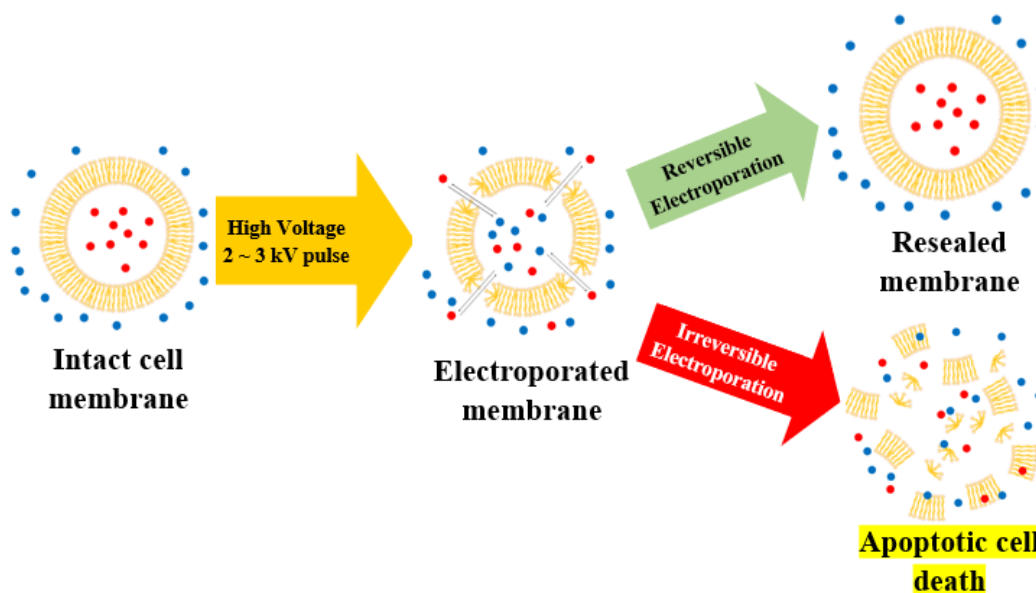


Figure 2.2. Schematic of electroporation using pulsed field ablation at intact cell membrane to induce cell apoptosis.

As described by Miklavcic and Kotnik [14] and Wachner and Gisma [15], the induced transmembrane potential (TMP) on the cell membrane can be calculated by taking into account the existence of a uniform electric field  $E_0$  being disrupted by the existence of a cell into an electric field  $E$ :

$$E = -\nabla\varphi \quad (1)$$

where  $\varphi$  is the electric potential satisfying the Laplace equation

$$\nabla^2\varphi = 0 \quad (2)$$

The TMP,  $\Delta\varphi$ , induced by an externally applied electric field to a cell is considered as the electric potential difference between the inner and outer surfaces of the membrane.

$$\Delta\varphi = \varphi_i - \varphi_e \quad (3)$$

where the subscript  $i$  denotes interior and  $e$  denotes exterior of the cell membrane. A TMP larger than 1 V must be applied to achieve cell death with IRE [14].

An analytical solution of electric field distribution was presented using the Laplace equation for two-needle electrodes by Corovic et al [16]. When assuming the

thickness of electrodes are uniform, with a circular electrode's radius of  $a$ , and with a distance between the electrodes of  $d$ , the Laplace equation can be solved in simplified two-dimension. The Laplace equation for the electric potential of the needles can be simplified when assuming the constant conductivity of the tissues as follows:

$$\nabla^2\varphi(x,y) = 0 \quad (4)$$

where  $\varphi(x,y)$  is the electric potential in the two-dimensional coordinate.  $\varphi(x,y)$  can be presented as the sum of the electric potentials of each needle as follows:

$$\varphi(x,y) = \sum_{n=1}^N \varphi_n(x,y) \quad (5)$$

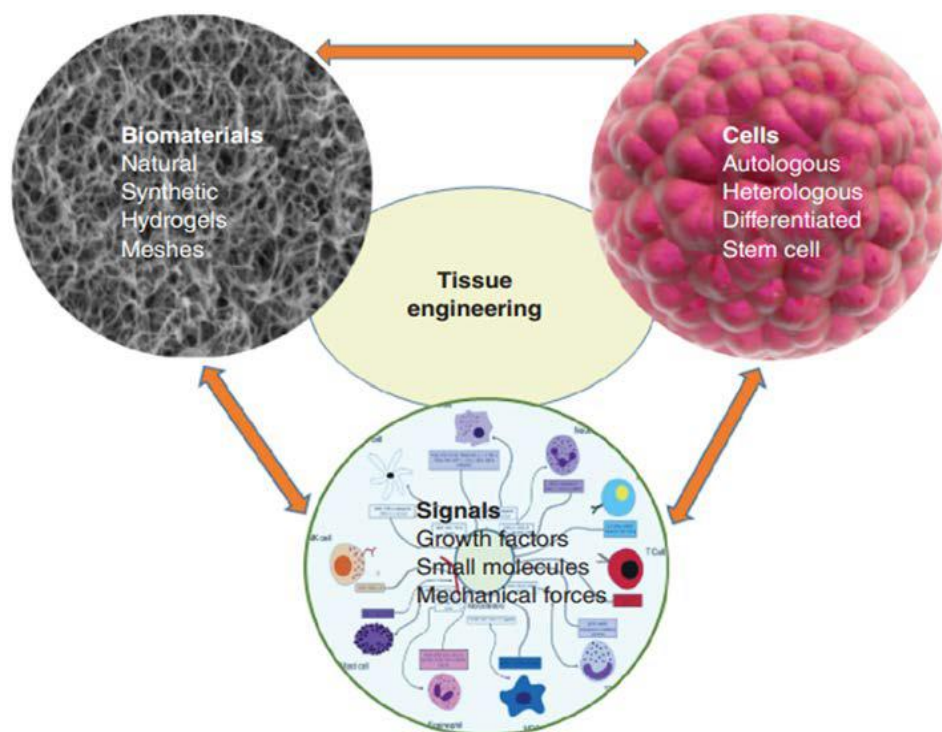
Then, the electric field is determined to be as follows by taking the derivative of  $\varphi(x,y)$  assuming two electrodes ( $n=2$ ):

$$E(x,y) = \frac{V_0}{2*\ln(\frac{d}{a})} * \left[ \frac{1}{a} - \frac{1}{d} \right] \quad (6)$$

where  $V_0$  is the applied electrical potential.

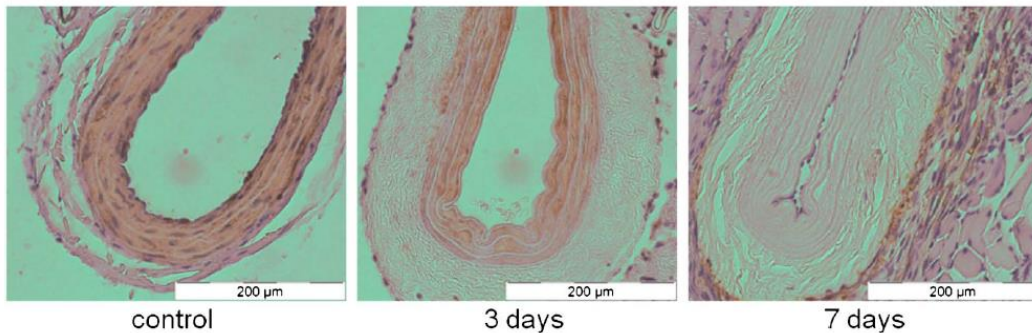
## 2.2 Pulsed field ablation for tissue engineering

Tissue engineering has been developed extensively as an industry and science since the paper of Langer and Vacanti over 29 years ago [17]. Tissue engineering has stabilized and become profitable since the turn of this decade as an industry [18]. Classically, tissue engineering is the use of a combination of cells, biomaterial scaffold, and signals like growth factors, small molecules, mechanical forces to improve or replace biological tissues (Figure 2.3) [19].



**Figure 2.3. Elements of tissue engineering; biomaterials, cells and signals**

Meanwhile, tissue scaffold is a key element of tissue engineering, and the ideal material for the scaffold is the extracellular matrix (ECM). This ideal scaffold can be produced by decellularization of living tissues using PFA in the targeted tissues. Previous studies demonstrated that the PFA spared the ECM of the tissues and produced the decellularized scaffold for rapid recellularization thereafter [20,21]. When the pulsed electric field was applied on the carotid artery *in-vivo*, a functional decellularized scaffold remained 3 days after PFA (Figure 2.4). Then, endothelial cells were regrown in 7 days, indicating that the scaffold preserved its function during the procedure.



**Figure 2.4. Smooth muscle cell removal after PFA on the carotid artery.**

The dark staining for  $\alpha$ -smooth muscle arteries ( $\alpha$ -SMA) in between the layers of the elastin presented that vascular smooth muscle cells (VSMC) decreased at 3 days and decellularized scaffold at 7 days after PFA treatment as compared to the control group.



## **2.3 Clinical applications of pulsed field ablation for treatment of locally advanced solid tumor**

The PFA has been used increasingly for cancer treatment over the past decade. PFA offers several advantages due to its nonthermal characteristics over other local treatment modalities, which are summarized in short treatment time, minimized thermal damage, and the ability to treat cancers near the major blood vessels [22]. Therefore, we reviewed clinical studies of PFA to treat cancer within the past decade in this chapter.

### **2.3.1 Locally advanced pancreatic cancer**

Locally advanced pancreatic cancer (LAPC) is non-metastatic, unresectable pancreatic ductal adenocarcinoma (PDAC), one of the most aggressive cancer with a 5-year overall survival rate of less than 10% [23]. LAPC generally encases the major vessels, such as the superior mesenteric artery, celiac artery, or portal vein which makes it hard to remove surgically. Therefore, the standard treatment for LAPC patients includes chemotherapy coupled with radiation or not [24,25]. In spite of the development of novel and powerful chemotherapeutic agents, there has been no significant progress yet. Minimally invasive ablation techniques are emerging as a promising and new alternative for the local destruction of LAPC [11,26–29]. As one of the minimally invasive ablation techniques, PFA induces the loss of cellular homeostasis resulting in apoptotic or necrotic cell death [30]. The high-voltage, ultrashort electrical pulses are applied through more than 2 needle electrodes, building pulsed electric fields among needles to destroy the LAPC.

PFA has obvious advantages over other focal ablation therapies such as radiofrequency ablation, microwave ablation, or ultrasound to treat LAPC. PFA primarily uses electrical energy to minimize heat generation, sparing sensitive surrounding structures such as bile ducts, large vessels, and the intestines [31,32]. Also, PFA has not been impeded by the “heat-sink effect”, which makes the thermal energy dissipating through the ductal structures. Therefore, LAPC near the large vessels or ducts can be ablated with PFA without the “heat-sink effect”. At last, the combination of the ablation with immunotherapy attracted attention recently to treat the PDAC [33]. PFA induces remarkable antigen release and activation of T cells resulting in a systemic immune response compared to other thermal focal modalities [34–36]. Therefore, PFA can be used as an outstanding focal ablation modality to destroy the malignant LAPC and to promote the recovery of the patients. Median overall survivals after PFA treatment for the LAPC patients were overviewed as shown below (Table 2.1).

**Table 2.1. Overall survival after pulsed field ablation for locally advanced pancreatic cancer.**

Overview of survival outcomes of LAPC patients who underwent PFA through laparoscopic, percutaneous, or open approach (median, in months). Referred from Moris et al [37].

Year	Authors	Approach	Overall Survival (months)
2015	Paiella et al. [38]	Open	7.5
2015	Kluger et al. [39]	Open	7.7
2015	Martin et al. [29]	Open	18
2015	Martin et al. [29]	Open	18
2015	Martin et al. [29]	Open	18
2016	Lambert et al. [40]	Open and Percutaneous	10.2
2016	Mansson et al. [41]	Percutaneous	7
2016	Stillström et al. [42]	Laparoscopic	14
2017	Vogel et al. [43]	Open	16
2017	Scheffer et al. [27]	Percutaneous	11
2017	Belfiore et al. [44]	Percutaneous	14
2017	Narayanan et al. [45]	Percutaneous	14.2
2018	Spilitiotis et al. [46]	Open	16.7
2018	Sugimoto et al. [47]	Open and Percutaneous	17.5
2018	Leen et al. [48]	Percutaneous	27
2019	Ruarus et al. [49]	Percutaneous	17

### **2.3.2 Locally advanced prostate cancer**

Focal ablative therapies for locally advanced prostate cancer (LAPRC) have been suggested to destroy the localized disease selectively [50,51]. The results appear promising in the medium-term despite the lack of long-term oncological results [52,53]. Many interests have been focused on prostate-sparing treatments in accordance with the advances in localization techniques for prostate tumors using mpMRI [54]. Several focal ablation modalities including radiofrequency ablation, cryotherapy, high-intensity focused ultrasound (HIFU), laser, photodynamic therapy (PDT), brachytherapy, and PFA are available to treat LAPRC [51].

PFA delivers high-voltage, ultrashort electric pulses to ablate the LAPRC through electrodes inserted transperineally [55]. Several papers have validated the efficacy of PFA in the short-term oncologic outcomes and the safety of PFA in the quality-of-life (QoL) [56–62]. We arranged clinical information and conditions of the PFA generator and the electrodes used in the table as shown below (Table 2.2).

**Table 2.2. Clinical and preclinical studies of pulsed field ablation for locally advanced prostate cancer.**

Procedure information							Generator						Electrode					Ref.	
Type	Organ	Approach method	No.	Muscle blocker	Sacrifice/ F-UP Period	Observation	Device	Voltage (V)	Current (A)	Pulse width ( $\mu$ s)	Pulse delay (s)	Pulse no.	Pulse type	Type	Size	No.	Distance (cm)		Exposure (cm)
Beagle	Prostate	Transperineally	6	O	2 weeks	Gross, H&E	DC generator	1000, 1500, 2000	N/D	100	0.1, 0.2	80	Monophasic	Monopolar two probes	18 G	2	0.5, 1, 1.5	N/D	[63] Onik, Gary (2007)
Beagle	Prostate	Incision	1	O	4 hours	H&E	ECM830 generator	1250 V/cm	5	100	1	100	Monophasic	Monopolar two probes	18 G	2	1	0.5	[64] Neal, Robert E (2014)
Human	Prostate Cancer	Transperineally	4	O	3, 4 weeks	H&E	Nanoknife System	1500 ~ 1750 V/cm	12~34	70	ECG Synch.	90	Monophasic	Monopolar two probes	18 G	2 <	1.2 ~ 1.5	1 ~ 1.5	[64] Neal, Robert E (2014)
Human	Prostate Cancer	Transperineally	20	O	6 weeks, 3, 6, 9, 12 months	Side Effect, Gleason Score	Nanoknife System	N/D	20~40	70	N/D	90	Monophasic	Monopolar two probes	19 G	N/D	N/D	N/D	[62] Valerio, Massimo (2014)
Human	Prostate Cancer	Transperineally	34	O	6 (1 ~ 25) Months	Side Effect, Gleason Score	Nanoknife System	N/D	20~40	70	N/D	90	Monophasic	Monopolar two probes	N/D	2~6	< 2	2	[59] Valerio, Massimo (2014)
Human	Prostate Cancer	Transperineally	32	O	6 weeks, 3, 6 months	Side Effect, Gleason Score	Nanoknife System	900 - 3000	20~40	70	N/D	90	Monophasic	Monopolar two probes	18 G	4.6 (3~6)	0.6 ~ 2	1.5 ~ 2.5	[61] Ting, F. (2016)
Human	Prostate Cancer	Transperineally	16	O	4 weeks	Affected essential structure	Nanoknife System	1200 ~ 2100 V/cm	15~45	90	ECG Synch.	90	Monophasic	Monopolar two probes	19 G	2, 3, 4 <	Pull back method	1.5	[65] Van den Bos, W. (2016)
Human	Prostate Cancer	Transperineally	20	O	6 weeks, 3, 6, 9, 12 months	Side Effect	Nanoknife System	N/D	20~40	70	N/D	90	Monophasic	Monopolar two probes	19 G			0.5 ~ 2	[66] Valerio, Massimo (2017)
Human	Prostate Cancer	Transperineally	429	O		Side Effect, Gleason Score	Nanoknife System	1518 $\pm$ 204 V/cm	N/D	N/D	N/D	N/D	Monophasic	Monopolar two probes	N/D	5 $\pm$ 1			[58] Guenther, E (2019)

\* N/D : No data

### **2.3.3 Locally advanced hepatocellular carcinoma**

Hepatocellular carcinoma (HCC) is widely known as the main cause of cancer-related deaths in the world [67]. More than 1 million people will die due to liver cancer in 2030 despite universal vaccination of hepatitis B, advanced screening, and antiviral therapies for hepatitis C [68]. While many screenings have been performed on high-risk groups and the early stage diagnosis has increased, many people have been still diagnosed as an unresectable HCC [69]. The focal ablative therapies including RFA, MWA, or cryotherapy are the standard solutions to treat the HCC unless the tumors are not located in the area adjacent to vascular or ductal structures [70,71].

PFA is a nonthermal focal ablation therapy sparing vital structures such as vessels, ducts within the target tissue and avoiding the heat-sink effect [72]. PFA has been used to treat the locally advanced HCC according to several papers [72–76]. We overviewed clinical information and conditions of the PFA generator and electrodes in the table as shown below (Table 2.3).

**Table 2.3. Clinical and preclinical studies of pulsed field ablation for locally advanced hepatocellular carcinoma.**

Procedure information							Generator						Electrode					Ref.	
Type	Site	Approach method	No.	Muscle blocker	Sacrifice/ F-UP Period	Observation	Device	Voltage (V)	Current (A)	Pulse width (µs)	Pulse delay (s)	Pulse no.	Pulse type	Type	Size	No.	Distance (cm)		Exposure (cm)
Human	Liver cancer	Open, Percutaneous	77	O	12 weeks, 3 months	Safety, Efficacy	Nanoknife System	3000	N/D	20~100	ECG Synch.	90	Monophasic	Bipolar, Monopolar	19 G	2~	15~23	N/D	[77] Philips, Prejesh (2013)
Human	Liver cancer	Percutaneous	44	O	2 weeks, 3, 6, 12 months	Safety, Efficacy	Nanoknife System	3000	N/D	20~100	ECG Synch.	90	Monophasic	Bipolar, Monopolar	19 G	2~5	5~20	N/D	[78] Cannon, Rober (2013)
Human	Liver cancer	Percutaneous	22	O	2, 4 weeks	Pain analysis	Nanoknife System	1500~3000	N/D	N/D	ECG Synch.	N/D	Monophasic	Bipolar, Monopolar	19 G	2~5	N/D	N/D	[73] Narayanan (2013)
Human	Liver cancer	Percutaneous	56	O	6 weeks, 3, 6 months	Adverse effects	Nanoknife System	1650~3000	N/D	90	N/D	70	Monophasic	Monopolar two probes	18 G	2~6	N/D	N/D	[79] Dollinger, Marco (2015)
Human	Liver cancer	Percutaneous	1	N/D	6 months	Major vessel safety	Nanoknife System	1540~3000	17.2~31.1	90	ECG Synch.	90	Monophasic	Monopolar two probes	N/D	4	12~18	N/D	[80] Kos, Bor (2015)
Human	Liver cancer	N/D	124	O	1, 5, 14 months	Liver function	Nanoknife System	1500~3000	N/D	N/D	N/D	70~90	Monophasic	Monopolar two probes	N/D	N/D	N/D	N/D	[81] Froud, Tatiana (2015)
Human	Liver cancer	Percutaneous	14	O	1, 3, 6, 9, 12 months	Safety, Efficacy	Nanoknife System	1500 V/cm	~50	100	ECG Synch.	90	Monophasic	Monopolar two probes	19 G	2~4	~20	20	[82] Eller, Achim (2015)
Human	Liver cancer	Open, Percutaneous	20	O	1, 3, 6, 9, 12 months	Adverse effects	Nanoknife System	~3000	N/D	20~100	ECG Synch.	90	Monophasic	Monopolar two probes	19 G	2~	15~20	15~20	[74] Padia, Siddharth A. (2015)
Human	Liver cancer	Percutaneous	34	O	6 weeks, 3, 6, 12 months	Safety, Efficacy	Nanoknife System	1500 V/cm	20~50	90	ECG Synch.	70	Monophasic	Monopolar two probes	19 G	2~6	10~20	N/D	[83] Niessen, Christoph (2016)
Human	Liver cancer	Percutaneous	35	O	6 weeks	Safety, Efficacy	Nanoknife System	N/D	N/D	N/D	N/D	N/D	Monophasic	Monopolar two probes	18 G	2~6	30	N/D	[84] Beyer, Lukas P. (2017)

\* N/D : No data

# Part I: DESIGNING EVALUATION METHOD OF PULSED FIELD ABLATED AREA

---

## Overview

From the concept of a ‘pulsed field ablation’, the designing evaluation method of abated area is of great importance in a wide variety of biomedical and clinical applications such as gene delivery, drug delivery, therapeutic research for locally advanced solid tumors.

In Part I, inspired by the biochemical features of the tetrazolium salts, we developed a novel evaluation method to investigate the pulsed field ablated area with 2,3,5-triphenyltetrazolium chloride (TTC), which no attempts have been made yet in the potato model. In addition, we used these new platforms as a tool for quantitative analysis of irreversibly or reversibly electroporated areas, predicting the extent of cell apoptotic areas for *in-vitro* and *in-vivo* studies.

Chapter 3 showed that the IRE-ablated area was distinguished with TTC staining in a potato model within 3 hours and showed results similar to conventional melanin accumulation area after pulsing. The TTC-unstained white areas were consistent over time and at different staining times. The presumed-RE area was formed with TTC staining in a potato model. The areas were highly correlated with electrical variables such as current and conductivity changes.

Our findings in Part I propose that TTC staining is a rapid biochemical reaction after pulsed field ablation and presents distinguishable lines for IRE or RE-ablated areas. Therefore, it might be the best choice to evaluate IRE-ablated and RE areas in a potato model.



## **Chapter 3. Evaluation of electroporated area using 2,3,5-triphenyltetrazolium chloride in a potato model**

### **3.1 Summary**

Irreversible electroporation (IRE) is a tissue ablation method, uses ultrashort high electric pulses and results in cell death in target tissue by irreversibly permeabilizing the cell membrane. Potato is commonly used as a tissue model for electroporation experiments. The blackened area that forms 12 hours after electric pulsing is regarded as an IRE-ablated area caused by melanin accumulation. Here, the 2,3,5-triphenyltetrazolium chloride (TTC) was used as a dye to assess the IRE-ablated area 3 hours after potato model ablation. Comparison between the blackened area and TTC-unstained white area in various voltage conditions showed that TTC staining well delineated the IRE-ablated area. Moreover, whether the ablated area was consistent over time and at different staining times was investigated. In addition, the presumed reversible electroporation (RE) area was formed surrounding the IRE-ablated area. Overall, TTC staining can provide a more rapid and accurate electroporated area evaluation.

## 3.2 Introduction

Irreversible electroporation (IRE), a tissue ablation method, uses ultrashort high electric pulses that cause low thermal damage and induce apoptotic cell death by irreversibly permeabilizing the cell membrane in the targeted tissue [85]. IRE was recently investigated as an alternative ablation method to several conventional tissue ablation techniques, such as cryoablation, radio-frequency ablation, and microwave ablation [86–89]. The advantages of IRE include producing a sharp boundary between treated and untreated areas, sparing vasculature and ductal networks, which results in more rapid tissue regeneration [90–92].

Many researchers used potatoes as models to evaluate IRE-ablated areas due to their low cost, relative convenience, and lack of ethical issues [93–96]. The evaluation is conventionally performed by calculating the blackened potato tissue area 12 hours posttreatment [97]. The intracellular polyphenol oxidation results in melanin accumulation that forms the dark area [98]. However, when using this method, obtaining the posttreatment results requires waiting for long hours. Furthermore, the results are affected by the inhomogeneity of the potato tissue [99].

Magnetic resonance imaging (MRI) was used for instant imaging of potato tissue changes after pulsing to overcome these disadvantages [100]. The ablation area detected using MRI was similar to the conventional melanin pigmentation ablation outcome in various electric field strengths. However, using MRI for most researchers is unsuitable due to its high cost and uneasiness to handle. The blue dye was used to evaluate IRE-ablated

areas on the potatoes using the osmotic equilibrium phenomenon, but RE areas were not detected [101].

The water-soluble tetrazolium salt has been used to evaluate cell viability in *in-vitro* and *ex-vivo* experiments [102–105]. The 2,3,5-triphenyltetrazolium chloride (TTC) is a representative agent for this purpose and is reduced to insoluble red-colored triphenylformazan crystals by the dehydrogenase produced by mitochondria in cells [106]. The IRE-ablated area was evaluated with TTC in *ex-vivo* swine pancreatic tissue [104]. The TTC-unstained white area was an IRE-ablated area in the swine pancreas tissue. This type of TTC staining has a rapid chemical reaction and reduces evaluation time. However, research is needed to evaluate the IRE-ablated area potato models using TTC staining.

Here, an IRE-ablated area was assessed based on TTC staining in a potato model after pulsing. The TTC-unstained white area was compared with the blackened area by the conventional melanin accumulation method. Moreover, the consistency of the TTC-unstained white area was examined to verify its accuracy and usefulness in IRE research. Moreover, the presumed-RE area was formed with the TTC staining after IRE pulsing on the potato. Furthermore, the correlation between the ablation area and the electrical properties of potatoes was examined to evaluate the suitability of the TTC staining method for electroporation research.

### **3.3 Materials and Methods**

#### **3.3.1 Electric fields simulation**

The geometry of the model was adopted from a previous study [107]. The electric field

strength between electrodes is governed by the Poisson equation as follows:

$$\nabla^2\phi = -\frac{\rho}{\epsilon_0} \quad 1$$

If the conductivity of the potato is supposed to be constant, a steady-state electric field distribution was obtained by solving the equation as follows:

$$\nabla^2\phi = 0 \quad 2$$

where  $\phi$  is the electric field strength, assuming the electrode length is larger than the distance between electrodes. The surface effects of the potato are neglected. The electric field strength is presented based on a gradient of the electric potential:

$$E = \nabla\phi \quad 3$$

The boundary condition is defined as either  $\phi = V_0$  or 0 in the applied tissue. The resting boundaries were assumed as electrically insulating ( $\frac{d\phi}{dn} = 0$ ). The electric field was estimated using the EPO code<sup>TM</sup> developed with the OpenFOAM (The Standard Co. Ltd., Gunpo-si, Republic of Korea).

### 3.3.2 Potato tissue ablation

A single batch of large-size (weight, ~240 g; length, 80 mm; and width, 60 mm) potato tubers from the same harvest were purchased from a local grocery store (Gunpo-si, Republic of Korea). All experiments were performed using the EPO-S1 generator (The Standard Co., Ltd.), a prototype pulse generator for IRE (Figure 3.1A). Two 6-Fr-

diameter stainless-steel needle electrodes with a 15-mm exposure length, inserted in parallel, normal to the potato slice surface, with a 10-mm center-to-center distance between the electrodes (Figure 3.1C), delivered the electric pulses. The treatment consisted of a square-pulsed electric field with 300, 600, 900, 1,200, or 1,500 V/cm, 100  $\mu$ s pulse width; 2,000  $\mu$ s pulse delay; and 32 pulse numbers to cause a sufficient IRE-ablated area according to the pre-test (Figure 3.S1, 3.S2). In the different staining time experiments, electric field strength 1,000 V/cm, 100  $\mu$ s pulse width, 2,000  $\mu$ s pulse delay, and 100 pulse numbers were used with the same electrodes as described above.

### **3.3.3 Conductivity and current measurement**

The conductivity measurement was performed using 4192A LF Impedance Analyzer (Yokogawa-Hewlett-Packard Ltd., Japan). A manual switch was placed between the experimental object and the analyzer for measurements after pulsing (Figure 3.1B). The conductivity was measured before pulsing, and the switch was turned off to ensure a connection between the object and pulse generator. After pulsing, the switch was immediately turned on to connect the analyzer to the object and was manually operated. The conductivity was measured using a 10-Hz frequency. A digital oscilloscope (TDA3044B, Tektronix, USA) was used for current measurements. A hole-type current probe (TCP305A, Tektronix) was clamped to a code connecting the pulse generator and the electrode.

### **3.3.4 Melanin accumulation and TTC staining methods**

A section from the treated potato was cut in 5 mm (width) × 4 ~ 6 cm (length) and placed at room temperature in about 60% humidified environment for 48 hours for melanin accumulation (Figure 3.1D). Another section was submerged into a dish containing 20 mL of 0.5% w/v TTC (Kanto Chemical Co., Ltd., Japan) in normal saline for 48 hours (Figure 3.1E). The results were quantitatively compared after 3 hours of TTC staining and 12 hours of melanin accumulation (Figure 3.1F). TTC staining was performed within 5 min after pulsing. Photographs were taken every hour for 8 h, and then once at 10, 12, and 24 hours thereafter. Melanin accumulation and TTC staining images were compared (Figure 3.2C). ImageJ 1.53c (Wayne Ribband, National Institutes of Health, USA) software was used to evaluate the IRE-ablated area in the potato models. The distance was set using a ruler in the software. Trainable Weka Segmentation was performed to create a binary image of the white area and deep red area caused by TTC staining to measure the IRE and the presumed reversible electroporation (RE) areas. Moreover, areas with accumulated black melanin were calculated using the same method.

### **3.3.5 Transmission electron microscopy (TEM)**

Fragments (1 × 3 mm) were excised from pulsed, inner medullar zones (IRE and deep red areas), and non-pulsed, perimedullar zones of the pulsed potato tuber. They were prefixed in 2% (w/v) paraformaldehyde and 2% (w/v) glutaraldehyde in 0.05M sodium cacodylate buffer (pH 7.2) at 4 °C overnight. They were washed with cacodylate buffer and post-fixed in 1% (w/v) osmium tetroxide at 4 °C for 2 h. The osmicated specimens

were en-bloc stained with 1% (w/v) uranyl acetate at 4°C overnight. The specimens were immersed in a graded ethanol series for dehydration, treated with 100% propylene oxide, and embedded in Spurr's resin. Ultrathin sections were obtained using an ultramicrotome (Leica UC7; Leica Microsystems, Wetzlar, Germany) and were mounted on 150-mesh copper grids. They were stained with 2% (w/v) uranyl acetate and Reynolds' lead citrate for 7 min each. The sections were examined using TEM (JEM1400plus; JEOL, Tokyo, Japan) at 120 kV.

### **3.3.6 Statistical analysis**

Experimental results were expressed as mean  $\pm$  standard deviation from three repetitions. A two-tailed paired Student's *t*-test was conducted to determine the significance of differences in means (\**P* < 0.05; \*\**P* < 0.01; \*\*\**P* < 0.001). Pearson's correlation statistics was used to determine correlation between electrical properties and ablated area of the two different staining methods after IRE. Statistical analysis was performed using Microsoft Excel 2013 (Microsoft Co., Ltd., Redmond, WA, USA) software.

## **3.4 Results**

### **3.4.1 Melanin accumulation and TTC staining over time**

Based on the experimental scheme (Figure 3.1), two staining methods were compared. Representative melanin accumulation and TTC staining are shown in Figure 3.1D and E. Three hours after pulsing, the samples for melanin accumulation only showed slight

changes, and a prominent ablation area was not observed. However, the TTC staining showed a clear white ablation area inside the deep red area (Figure 3.2A). After 12 h, the ablation region in the melanin accumulation became dark black, and in the TTC staining, the white dead cell area remained (Figure 3.2B). The red, color-stained area in the TTC staining became visible 1 hours after pulsing and showed a clear demarcation 3 hours posttreatment compared with melanin accumulation, which required >12 hours after pulsing for visualization of results (Figure 3.2C).

The results showed that IRE-ablated areas by TTC staining showed consistency over various electric field strengths (Figure 3.2D). The melanin accumulation area increased over time and was similar to TTC staining areas 48 hours posttreatment.

### **3.4.2 Comparison of melanin accumulation and TTC staining at various electric field strengths**

IRE treatment was performed on potatoes with increasing electric field strength to compare the ablation area using melanin accumulation and TTC staining (Figure 3.3A). The ablation area significantly increased depending on the intensity of the field strength in both staining methods (Figure 3.3B). In general, both the TTC-unstained white area and the blackened area in melanin accumulation seemed similar. Ablated areas in both methods were not significantly different at the various electric field strengths (Figure 3.3B,  $P > 0.05$ ). With a Pearson's correlation coefficient of 0.9687, the ablated areas stained by the two methods were highly correlated (Figure 3.3C,  $P < 0.0001$ ).



### **3.4.3 Current and conductivity changes at the various electric field strengths**

Electrical properties, such as current and conductivity change, were estimated to investigate the correlation between the two staining methods (Figure 3.4). Current that passed through the potato tissue after applying 32 pulses of 1,500 V/cm is shown in Figure 3.4A. The inset in Figure 3.4A shows several square pulses of 100  $\mu$ s pulse width and 2,000  $\mu$ s interpulse delay. The current gradually increased from 12.5 A to ~15 A and saturated after the 17<sup>th</sup> pulse. Conductivity at 10 Hz was measured before and after pulsing for the different electric field strengths. The conductivity tended to increase linearly with the electric field strength (Figure 3.4B). A 10-Hz frequency was selected to measure the conductivity because, compared with the other frequencies, it provides the most significant difference in conductivity after pulsing (Table 3.S1).

### **3.4.4 TTC staining at different times**

TTC staining was performed at 5 min; 30 min; and 1, 4, and 21 hours after pulsing to investigate whether the IRE ablation area changes (Figure 3.5A). The white IRE-ablated areas were consistent at the different staining times except for a slight increase in the 4 hours and the 21 hours groups (Figure 4B). These results showed the IRE-ablated areas were similar regardless of the staining time (Figure 3.5B). Deep red areas decreased as the staining time became late, and the areas at 1 hours and 4 hours after pulsing were significantly lower than that of 5 min ( $P < 0.01$ ) (Figure 3.5C).

### **3.4.5 TEM analysis of the potato tissue by TTC staining**

TEM revealed whether the continuity of the plasma membrane was preserved after pulsing in the TTC-stained and unstained areas on the potato tissue. Non-pulsed perimedullar zone, pulsed TTC-unstained inner medullar zone, and pulsed TTC-stained deep red inner medullar zone were investigated using TEM (Figure 3.6A).

TEM revealed the well-preserved plasma membrane overall attached to the cell wall in the perimedullar zones of the tuber in the non-pulsed perimedullar zone (Figure 3.6B, Figure 3.S3A). Organelles, such as Golgi bodies and mitochondria, were commonly observed in the cytoplasm. The cisternae, lumens, and secretory vesicles could be discerned from the Golgi body (Figure 3.S3B). Magnified views showed double membranes and cristae of the mitochondria (Figure 3.S3C). Complex plasmodesmata were often seen between two adjoining parenchyma cells (Figure 3.S3D).

The cytoplasmic disruption occurred in the IRE inner medullar zone (Figure 3.6C, Figure 3.S4A). The pulsed cytoplasm partially contained electron-dense vesicles with various diameters. The absence of an electron-dense continuous plasma membrane was commonly observed along the cell wall in the magnified views (Figure 3.S4B). No distinct organelles were found in the cells (Figure 3.S4C). Magnified views showed the disrupted cytoplasm and plasma membrane detached (to ~1  $\mu\text{m}$ ) from the cell wall (Figure 3.S4D).

Partially continuous electron-dense plasma membranes were commonly found in the TTC-stained deep red inner medullar zone (Figure 3.6D, Figure 3.S5A). Magnified

views showed the dotted electron-dense remains and detachment of the plasma membrane (to ~500 nm) from the cell wall (Figure 3.S5B). Partially disrupted organelles, including Golgi bodies, were found near the plasma membrane in the cells (Figure 3.S5C). Small vesicles, ~100 nm or less in diameter, were observed between the plasma membrane and cell wall (Figure 3.S5D). Vesicular bodies appeared to fuse with the plasma membrane.

Magnified views showed differences in the plasma membrane integrity between the inner medullar and perimedullar zones. Continuous electron-dense lines were evident along the cell wall of the perimedullar zones (Figure 3.6B). Without a distinct plasma membrane, the fibrillar arrangement was apparent on the cell wall of the IRE inner medullar zones (Figure 3.6C). Dotted remains of the plasma membrane were found in the TTC-stained deep red inner medullar zone (Figure 3.6D).

### **3.5 Discussion**

Many researchers have evaluated IRE-treated areas in potato models using melanin pigmentation caused by intracellular polyphenol oxidation [93,94,98,108]. This method is convenient to perform because minimal preparation is required. However, >12 hours are required to obtain such results [97]. Furthermore, the blackened area in melanin accumulation may include the RE-treated areas, which are consisted of live cells [109]. Therefore, it is challenging to determine that the blackened area in the treated potato model only consists of dead cells.

TTC staining has several advantages over the currently used melanin accumulation methods regarding evaluating the IRE-treated areas. First, researchers can

obtain the ablation results within 3 hours after pulsing (Figure 3.2A). The recommendation is that experimental time should be short when using potato tissues after pulsing because living tissues, like potatoes, are susceptible to the external environment, such as ambient temperature and humidity. Moreover, the consistency of the IRE-ablated area using TTC staining was verified at different staining times in the present study experiments (Figure 3.5B).

Furthermore, TTC staining showed a clear demarcation line within 3 hours (Figure 3.2C). In TTC staining, the viable cell area becomes red due to the reduction of tetrazolium salt when a living cell remains and the dead cell areas become white [105]. Therefore, TTC staining is more applicable to IRE research [57,110,111]. TTC-unstained white area is relatively consistent during 48 h, but the melanin accumulation area changes gradually over time (Figure 3.2D). At 48 h, the IRE-ablated areas accumulated melanin and finally were similar to the TTC-unstained white areas. These results correspond to the previous study stating that 48 hours is the optimal time for melanin accumulation to observe the IRE-ablated area [112]. These TTC staining characteristics provide several advantages for IRE researchers using a potato model, such as more rapid and accurate detection than the conventional method.

Potato tubers were recently adopted to evaluate the ablation area using high-frequency irreversible electroporation (H-FIRE) [112]. Unlike conventional IRE, H-FIRE comprises biphasic pulse trains, making pulse parameter combinations more complicated, such as positive pulse width, negative pulse width, interpulse delay, and inter-phase delay. TTC staining has an advantage when researchers investigate various

conditions of H-FIRE due to rapidness and consistency.

TTC staining provides not only IRE-ablated white areas but also deep red areas surrounding white areas (Figure 3.3Aj–2Ap). These extra red areas in TTC staining were dyed darker than the outside, which was similar between 100 and 250 V/cm line simulation results (the outermost black line of simulation in Figure 3.3Aj–3Ap). The potato cells in these red areas might be alive, referring to the previous study stating that potato cell membranes were intact under a 200 V/cm pulsed electric field [105]. Note that these deep red areas were observed when TTC staining was performed on the potato 5 min, 30 min, 1 h, and 4 hours posttreatment (Figure 3.5Aa, 4Ab, 4C), whereas the areas were not observed in TTC staining at 21 hours after IRE (Figure 3.5Ac, 4Ad). In general, the cell membrane took a few minutes to reseal after electroporation [113]. The deep red areas decreased as the staining time was delayed, hinting cell membrane resealing was being processed. Based on the TTC staining mechanism, TTC is reduced by dehydrogenase in the cell mitochondria, resulting in a red color formazan [106,114]. Therefore, the color intensity around IRE-ablated areas could be related to the health of the cell. However, it is weird to explain that more cells in the deep red areas were alive because the color was darker than the untreated outer area. Potentially, when the cell membrane is reversibly electroporated with electrical stimulation, TTC molecules are diffused into the cell as per Fick's law of diffusion [115]. It might trigger more chemical reactions between TTC and dehydrogenase produced in the cell mitochondria, causing a deeper red than in the surrounding area.

Plasma membranes were observed using TEM to ensure these outcomes. Irreversible electroporation was theoretically known to form innumerable nanoscale pores in the plasma membrane [116]. Nevertheless, it is challenging to observe them due to the innate metastable nanopore structures in the bilayer and technical limitations in specimen microscopy preparation [117]. This study demonstrated differences in parenchyma cell ultrastructure between the inner medullar and perimedullar zones of potato tuber (Figure 3.6). In the non-pulse potatoes, perimedullar zones showed the overall continuous electron-dense plasma membrane attached to the cell wall (Figure 3.6B), and their organelles appeared to have typical structures, such as cisternae and cristae. However, in the pulsed potatoes, IRE inner medullar zone was primarily characterized by the disruption of the plasma membrane and organelles in the cells (Figure 3.6D). Instances were noted where partial degradation and detachment of plasma membrane from the cell wall occurred in the presumed-RE inner medullar zone (Figure 3.D). Such membrane aberrancies have been exemplified using TEM in other organisms [118,119].

Different membrane disruption levels were noted in the potato tuber between the IRE and presumed-RE inner medullar zones (Figure 3.6C, D). The degradation of the plasma membrane was more pronounced in the IRE regions compared with the presumed-RE regions. Given the cellular programs for plasma membrane remodeling, the detachment of the plasma membrane from the cell wall could be assumed to be an intermediate phase for sealing holes [120]. More studies await the elucidation of mechanisms underlying possible plasma membrane sealing and reattachment to the cell wall.

Furthermore, TTC staining highly correlated with electrical changes in the potato compared with melanin accumulation (Figure 3.7). Electrical properties were compared between TTC staining and melanin accumulation; the current that flowed when pulsed electric field stimulation was applied and the conductivity change ratios at 10 Hz represent the extent of cell damage in electrically stimulated tissue [121]. Regarding current, the correlation between current and melanin accumulation area had a correlation coefficient value of 0.9506 ( $P < 0.0001$ , Figure 3.7A), and between current and TTC-unstained white area had a Pearson's correlation coefficient value of 0.9577 ( $P < 0.0001$ , Figure 3.7C). The TTC-unstained white area had a slightly higher correlation with the current than the melanin accumulation area. Regarding the conductivity change ratio at 10 Hz, the correlation between conductivity change ratios and melanin accumulation area had a correlation coefficient value of 0.9096 ( $P < 0.0001$ , Figure 3.7B), and between conductivity change ratios and TTC-unstained white area had a Pearson's correlation coefficient of 0.9211 ( $P < 0.0001$ , Figure 3.7D). The TTC-unstained white area had a slightly higher correlation with conductivity change ratios than the melanin accumulation area. The heat map showed which variables had highly correlated coefficient values (Figure 3.7E). Moreover, the TTC-stained presumed-RE area was positively correlated with other values, except for the conductivity change. These relatively low correlations between presumed-RE area and other variables were estimated to be so due to the large measurement deviations, because the delineations of the deep red areas were relatively less pronounced compared with the TTC-unstained white area. Other variables had a correlation coefficient  $> 0.85$ . These results showed that TTC staining is an acceptable

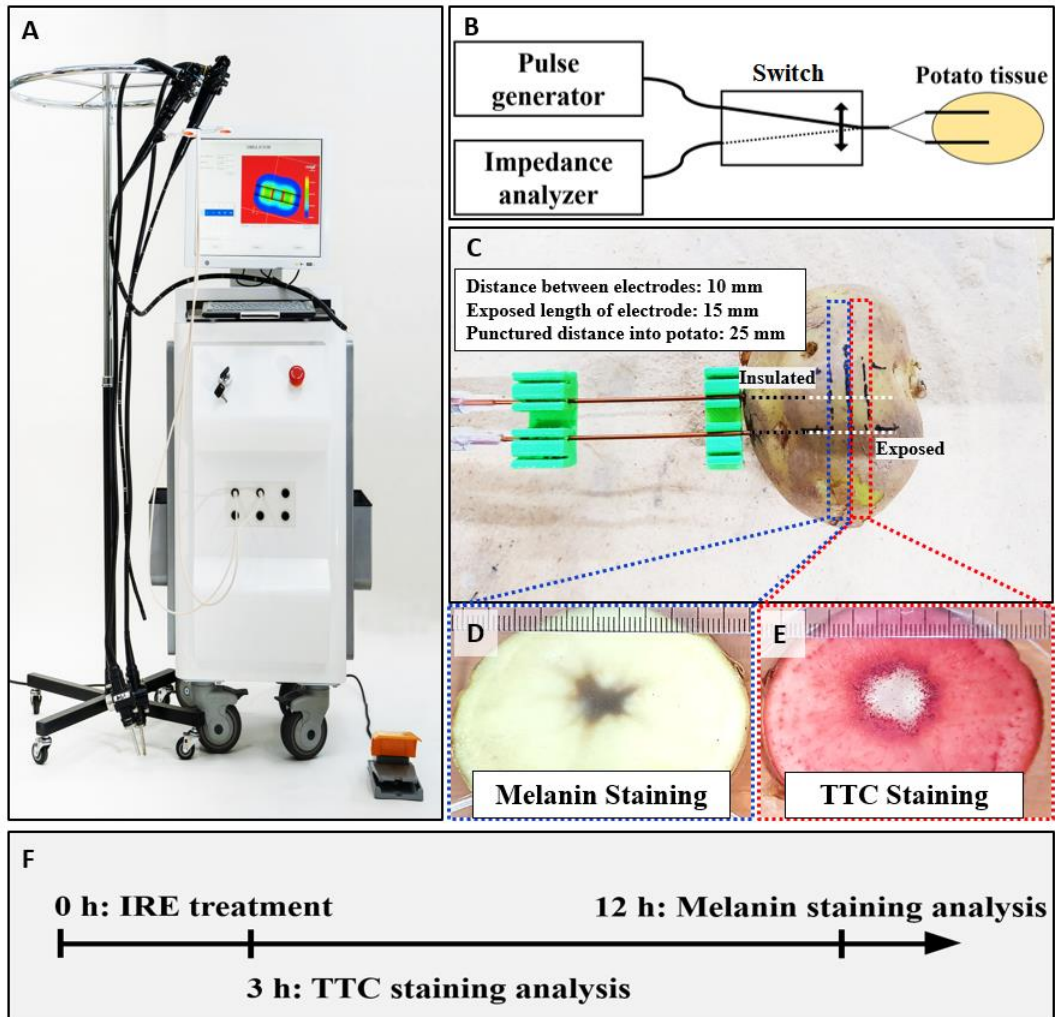
method for analyzing the IRE-ablated area associated with electrical current and conductivity changes in potato tissue.

TTC staining showed more consistent results compared with melanin accumulation in potatoes. Homogeneity of tissue is essential to evaluate the IRE-ablated area. However, potato tissue is not very homogeneous, and the ablation outcome can be affected by inner tissues [99]. Here, melanin accumulation area was affected by the inner medullar zone with a star-shaped ablation area. Nonetheless, TTC-unstained white area was less affected by the potato inner medullar zone on other sections of the same potato (Figure 3.8). This result indicated that TTC staining could provide a more accurate ablation area when using potato tissues for IRE researches.

The limitation of this study was that the TTC-stained presumed-RE area was not directly identified. Additional microscopy studies are needed to investigate whether the potato cells in the presumed-RE region show reversible nanopores after pulsing. Furthermore, the mechanism of this phenomenon should be investigated in future studies.

In summary, the IRE-ablated area was distinguished with TTC staining in a potato model within 3 hours and showed results similar to conventional melanin accumulation area after pulsing. The TTC-unstained white areas were consistent over time and at different staining times. The presumed-RE area was formed with TTC staining in a potato model. The areas were highly correlated with electrical variables such as current and conductivity changes. Hence, TTC staining might be the best choice to evaluate IRE-ablated and RE areas in a potato model.





**Figure 3.1. Experimental setup for comparing melanin accumulation and TTC staining methods.** (A) The EPO-S1 system (The Standard Co., Ltd.) was used as a pulse generator for IRE. (B) An impedance analyzer with a relay was used to measure the conductivity between the electrodes in the potato. (C) The electrodes had a 1-mm outer diameter, 10-mm distance, 10-mm exposure (not insulated part), and 25-mm puncture distance into the potato. The potato was punctured with electrodes. (D) The left side of the sectioned potato was accumulated with melanin from the middle point of the exposed needle. (E) The right side was stained with TTC. (F) The experimental timeline shows TTC staining analysis was faster than the melanin accumulation analysis.

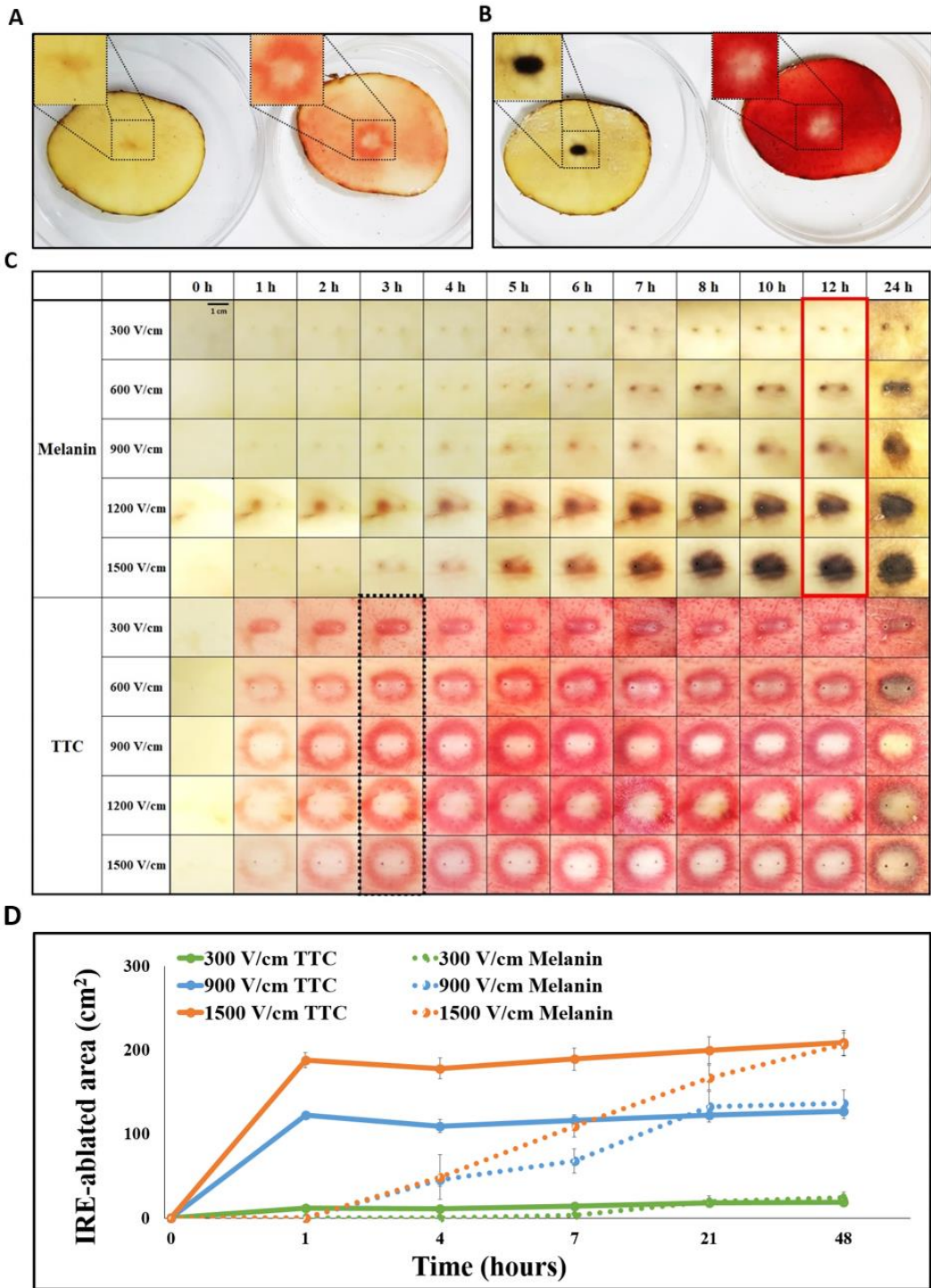
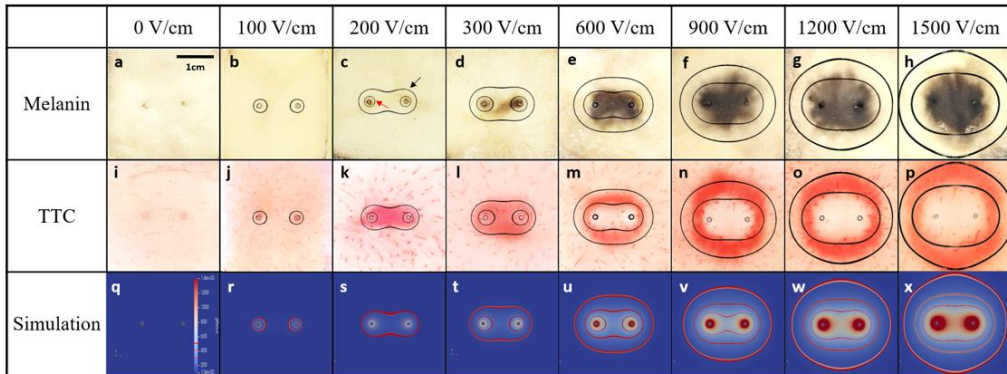


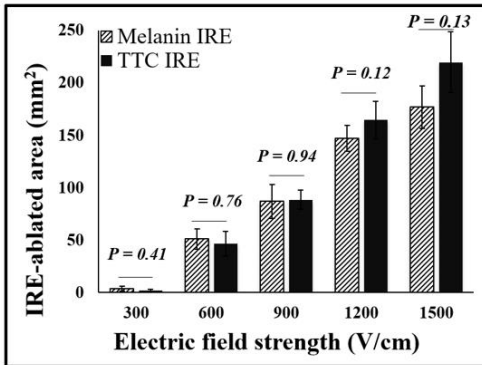
Figure 3.2. Comparison of melanin accumulation and TTC staining area over time.

(A) Three hours after pulsing, TTC staining showed a distinct IRE-ablated area (right) compared with melanin accumulation, which showed a minimal tissue change (left). (B) Twelve hours after pulsing, the samples for melanin accumulation also showed a distinct IRE-ablated area (left), and the white dead cell area remained in TTC staining (right). (C) Melanin accumulation and TTC staining in the treated potato during 24 hours at various voltage conditions. The samples for melanin accumulation showed the ablated area 12 hours after pulsing, and TTC staining showed the clear demarcation line of the ablated area 3 hours after pulsing. (D) IRE-ablated area comparison graph between melanin accumulation and TTC staining during 48-hour period.

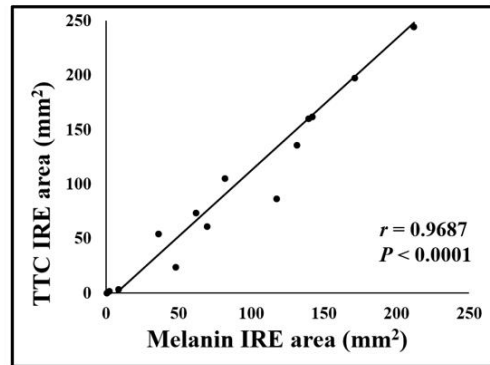
**A**



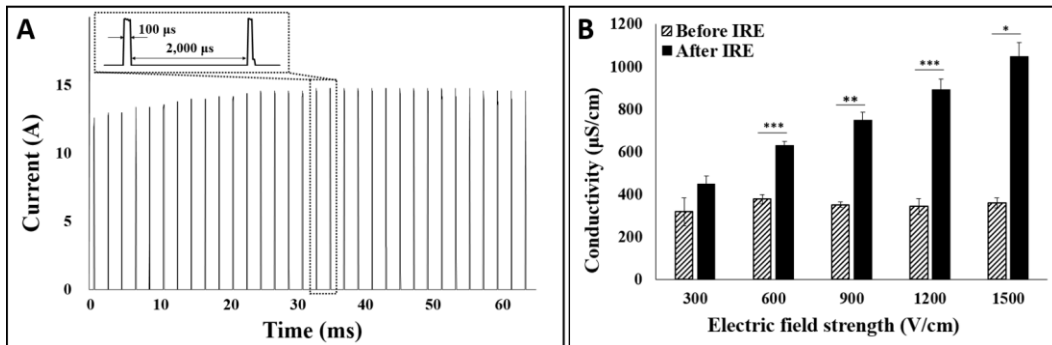
**B**



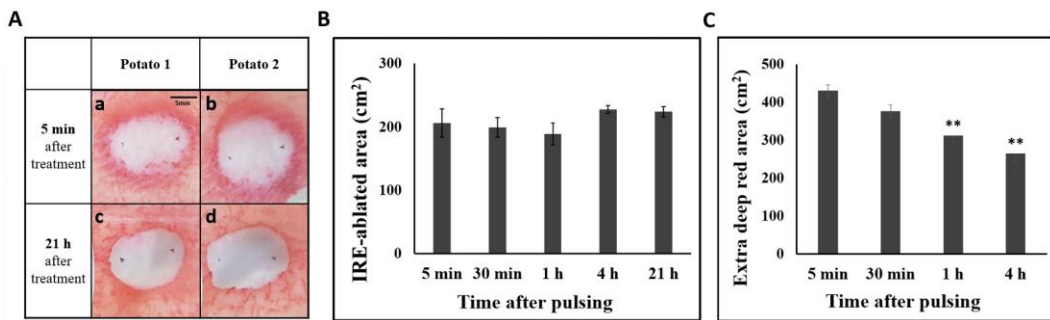
**C**



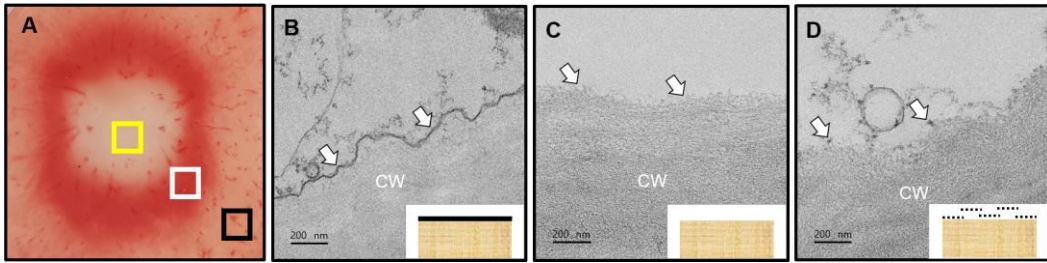
**Figure 3.3. Comparison of pulsed electric field ablation area between melanin accumulation and TTC staining on the various conditions.** (A) Comparing melanin accumulation and TTC staining methods for the IRE-treated area in the potato model at various electric field strengths. (a–h) Conventional melanin accumulation results after pulsing with simulation results (red arrow indicates 250 V/cm line; black arrow indicates 100 V/cm line). (i–p) TTC staining results after pulsing with simulation results. (q–x) Simulation results were calculated using the OpenFOAM program for each condition (red lines indicate 500, 250, and 100 V/cm from the inside). (B) Histogram of IRE-ablated area in potato accumulated melanin or stained with TTC. In both staining methods, the ablation area increased depending on electric field strength. (C) Correlation data showed the two staining methods for IRE were similar with a high correlation value of 0.9687 ( $P < 0.0001$ ) using Pearson's correlation statistics. A two-tailed paired Student's *t*-test was used to determine significance (\* $P < 0.05$ ; \*\* $P < 0.01$ ; \*\*\* $P < 0.001$ ).



**Figure 3.4. Electrical current and conductivity changes after pulsed electric field ablation.** (A) current flow after 1,500 V/cm 32-pulse stimulation and (B) conductivity changes at 10 Hz, before and after pulsing. Conductivity change ratio increased as electric field strength increased. A two-tailed paired Student's *t*-test was used to determine significance (\* $P < 0.05$ ; \*\* $P < 0.01$ ; \*\*\* $P < 0.001$ ).

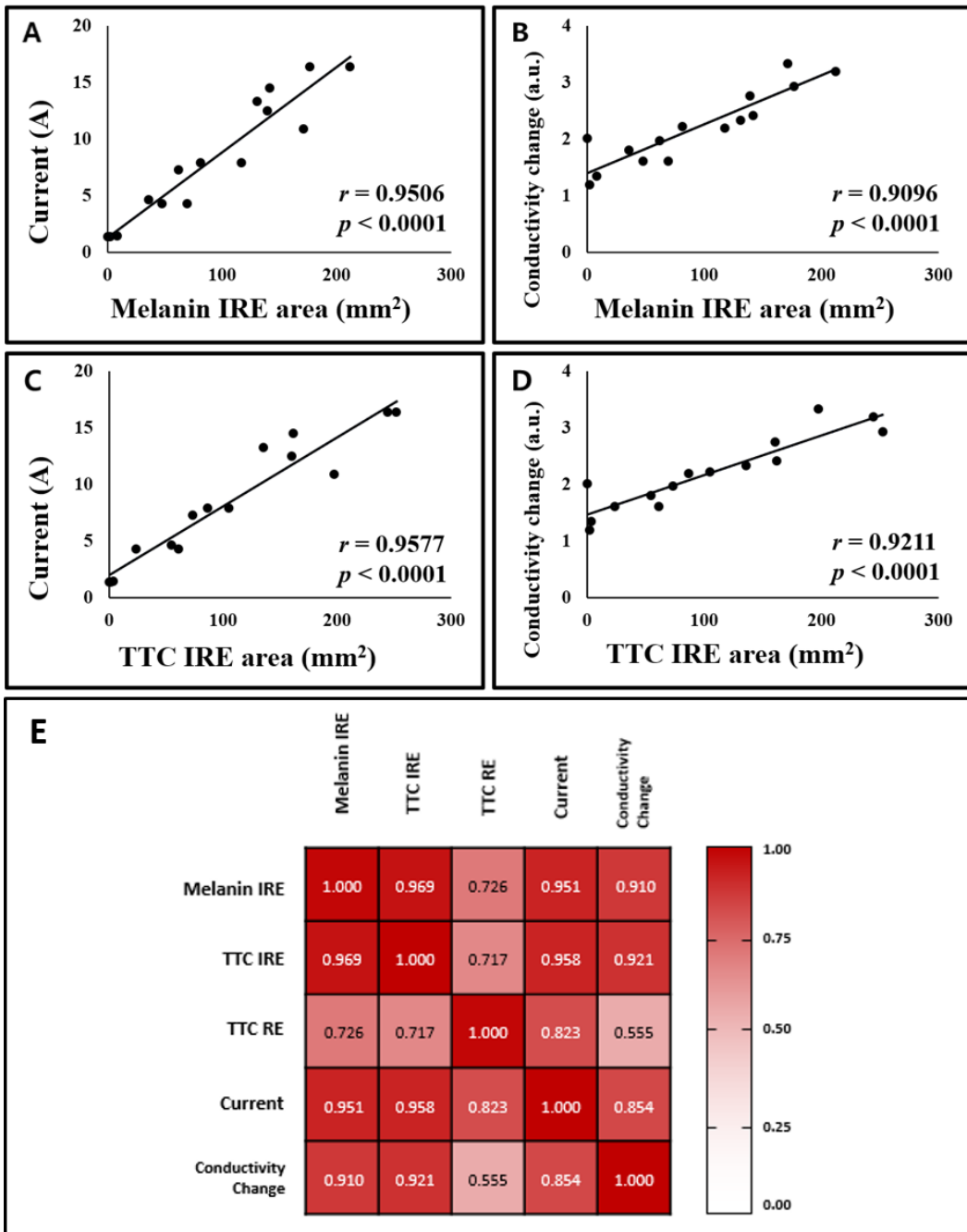


**Figure 3.5. IRE-ablated area at different staining times after pulsing.** (A) After treating the potato with IRE, TTC staining was performed within 5 min on half of the potato (a, b) and 21 hours after pulsing on the other half of the potato (c, d). (B) Result comparisons of the TTC-unstained white areas in IRE-treated potatoes at different staining times. (C) Deep red areas at different staining times. A two-tailed paired Student's t-test was used to determine significance compared with the 5 min group (\* $P < 0.05$ ; \*\* $P < 0.01$ ; \*\*\* $P < 0.001$ ).



**Figure 3.6. TEM analysis of TTC-unstained and TTC-stained areas after pulsing on the potato tissue.** (A) The black box indicates a non-pulsed perimedullar zone, the yellow one indicates pulsed TTC-unstained inner medullar zone, and the white one indicates pulsed TTC-stained deep red inner medullar zone. (B) Non-pulsed perimedullar zone with evident electron-dense line (arrows) along the cell wall (CW). (C) Pulsed TTC-unstained medullar zone with no electron-dense line along with the CW. (D) Pulsed TTC-stained deep red inner medullar zone with partially continuous electron-dense lines along with the CW.

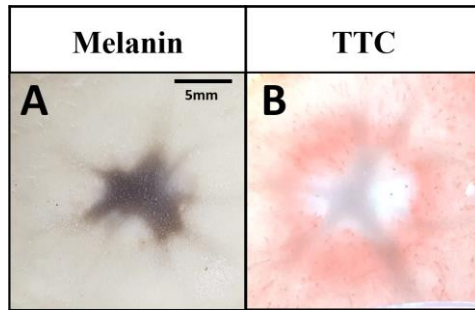




**Figure 3.7. Correlation among electrical properties and each staining method.** (A) Correlation graph between current and IRE-ablated area by melanin accumulation with a high correlation value of 0.9506 ( $P < 0.0001$ ). (B) Conductivity changes at 10 Hz and IRE-



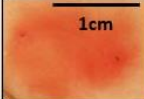

















ablated area by melanin accumulation with a value of 0.9096 ( $P < 0.0001$ ). (C) Current and TTC-unstained white IRE-ablated area with a value of 0.9577 ( $P < 0.0001$ ). (D) Conductivity changes at 10 Hz and TTC-unstained white IRE-ablated area with a value of 0.9211 ( $P < 0.0001$ ). (E) Heat map between IRE-ablated area by melanin accumulation, TTC-unstained white IRE-ablated area, TTC-stained presumed-RE area, current, and conductivity changes at 10 Hz. TTC-unstained IRE-ablated area had a higher correlation value than IRE-ablated area by melanin accumulation with current and conductivity change. Pearson's correlation statistics and P-values were used for correlation and statistical significance.



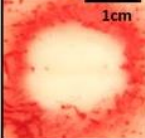
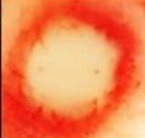
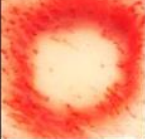
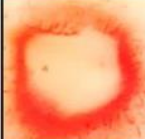
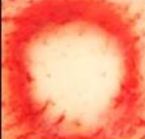

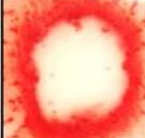


**Figure 3.8. The extent to which the IRE-ablated area is affected by the inner tissue inside the potato.** (A) Melanin accumulation area after pulsing was star-shaped, affected by the inner tissue. (B) TTC-unstained white IRE-ablated area was less affected by the inner tissue and showed an oval shape.

**Table 3.S1. Conductivity change rate before and after IRE treatment on potato at various voltage conditions depending on the frequency**

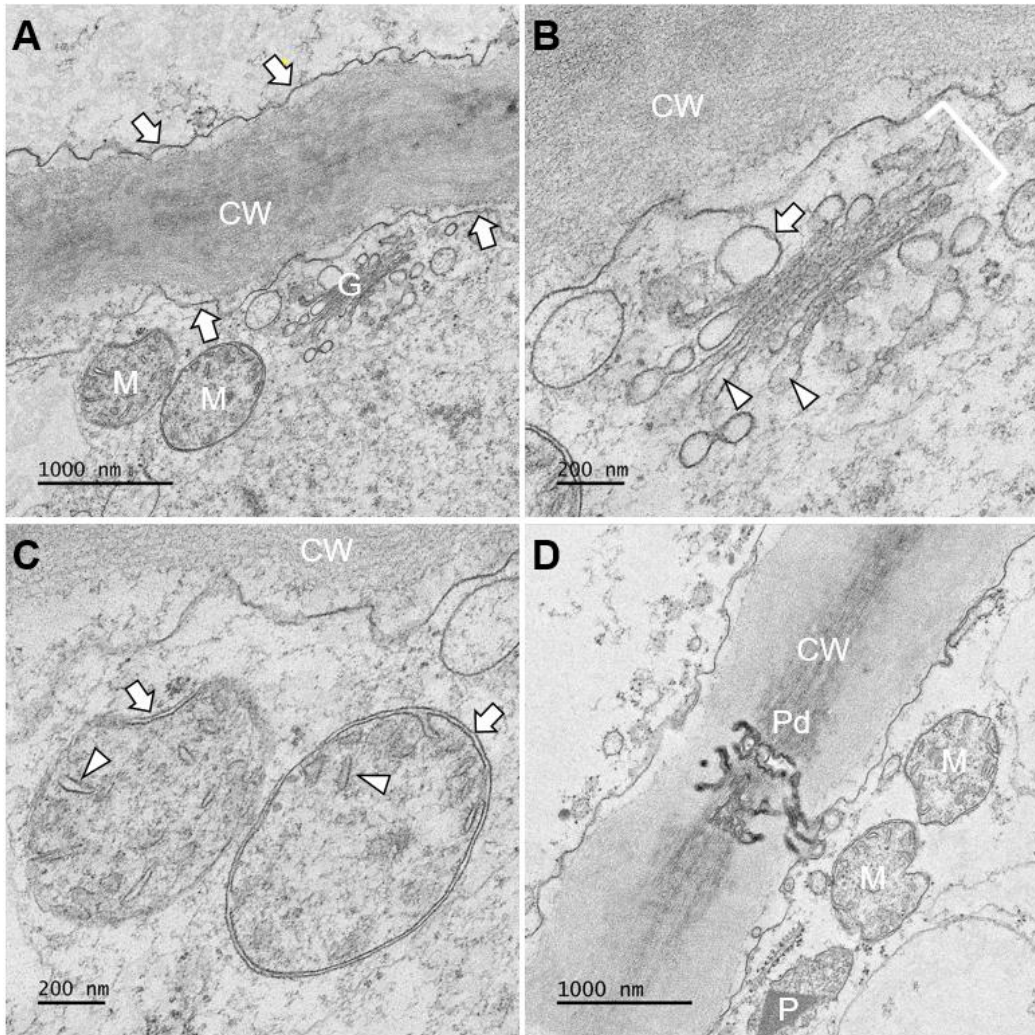
Unit: %	10 Hz	100 Hz	1,000 Hz	10,000 Hz	100,000 Hz	1,000,000 Hz	10,000,000 Hz
300 V/cm	4.1	-1.5	0.8	2.6	18.6	8.1	-1.0
500 V/cm	20.4	13.9	16.2	17.0	34.2	11.1	-1.5
700 V/cm	27.3	23.3	28.6	32.2	48.2	11.9	-1.7
900 V/cm	31.9	28.7	39.5	51.5	60.9	8.8	-1.3
1100 V/cm	83.1	75.3	78.7	76.9	85.5	21.0	0.5

	500 V/cm	700 V/cm	900 V/cm	1100 V/cm	1300 V/cm	1500 V/cm
8 pulses						
16 pulses						
32 pulses						

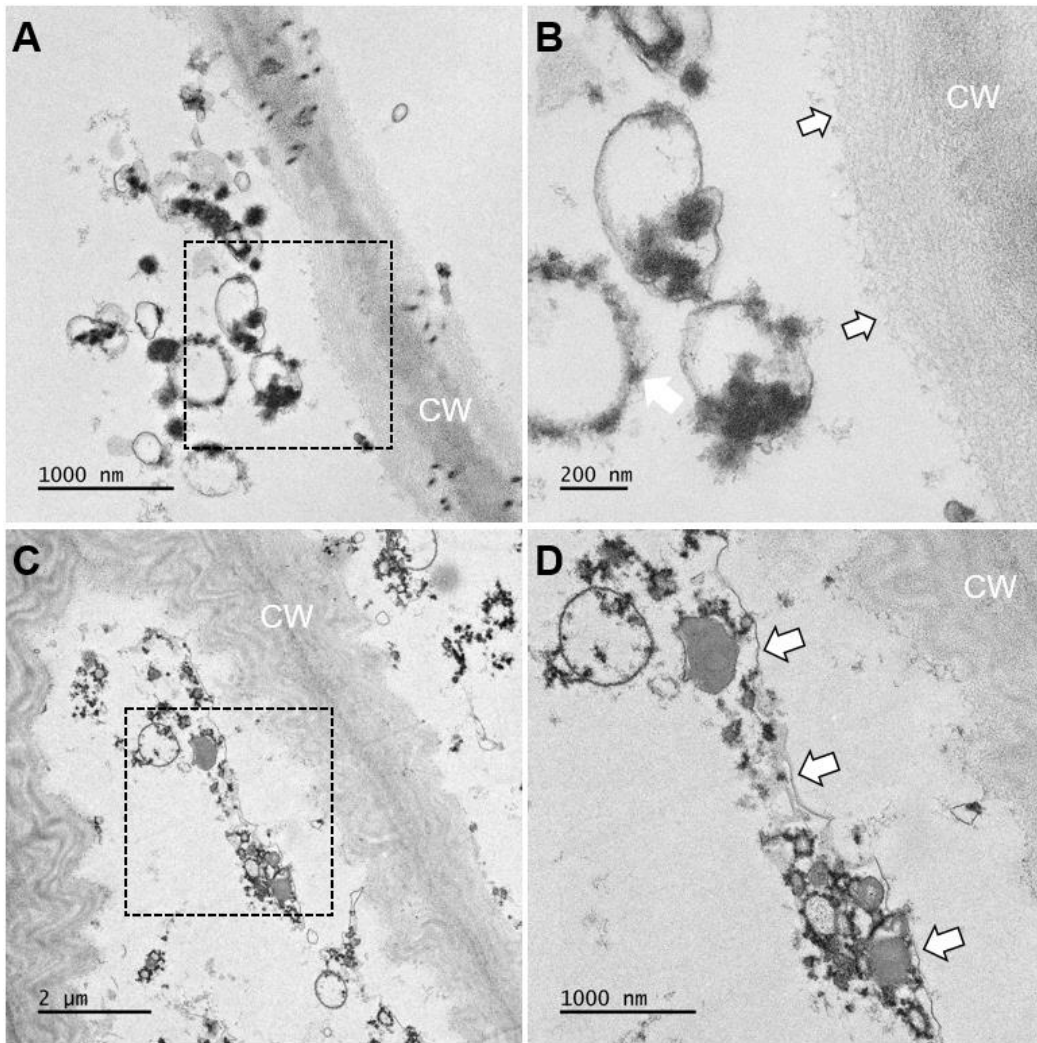
**Figure 3.S1. Preconditioning for pulse conditions of voltage, pulse numbers.** TTC staining on potato tissue 3 hours posttreatment at various pulse voltage and pulses with 100  $\mu$ s pulse width, 200  $\mu$ s pulse delay

Pulse Delay	Repetition 1	Repetition 2	Repetition 3
100 $\mu$ s			
2,000 $\mu$ s			
1 s			

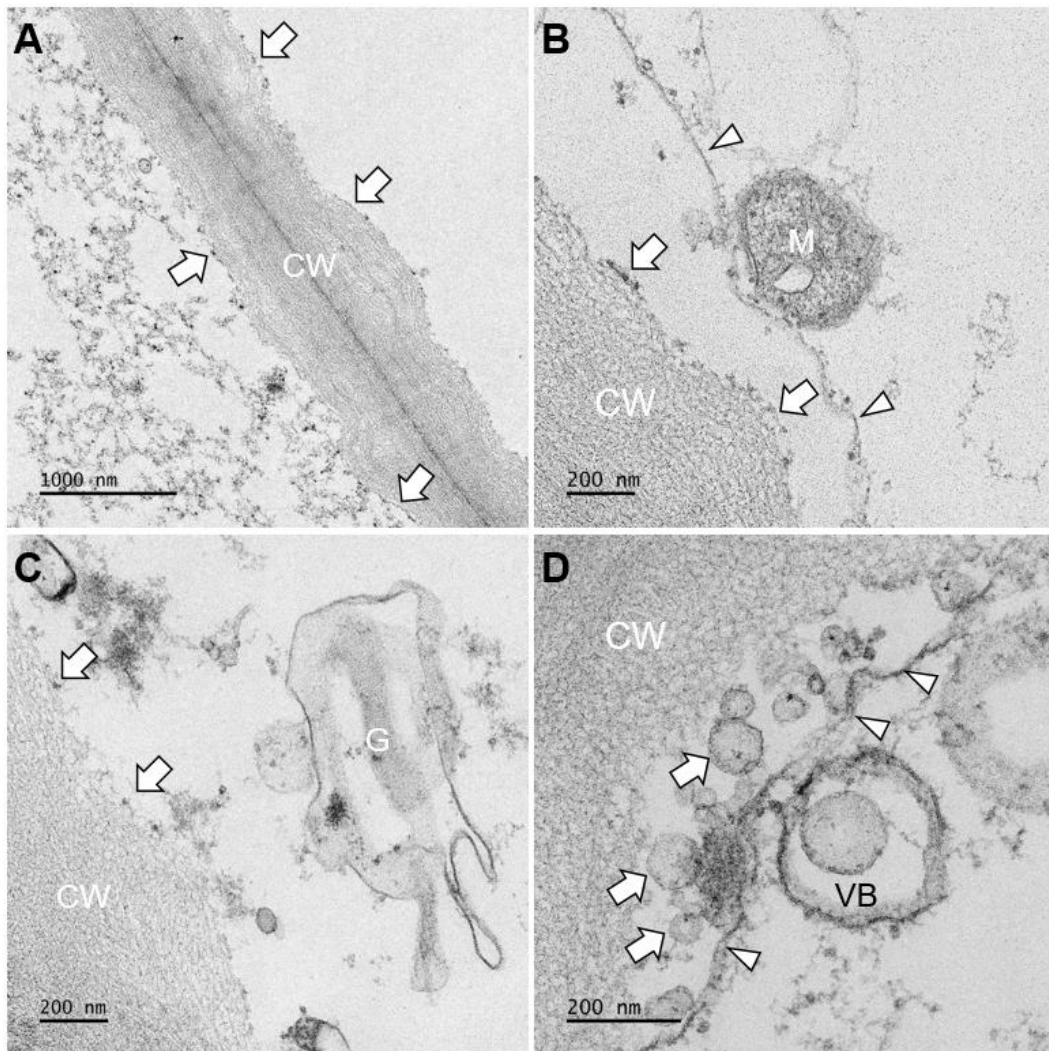
**Figure 3.S2. Preconditioning for pulse conditions of pulse delay.** TTC staining on potato tissue 3 hours posttreatment at various pulse delay with 1000 V/cm pulse voltage, 36 pulse number



**Figure 3.S3. TEM analysis of non-pulsed perimedullar zone with evident electron-dense line (arrows) along the cell wall (CW).** (A) The well-preserved plasma membrane overall attached to the cell wall in the perimedullar zones of the tuber in the non-pulsed perimedullar zone. Organelles, such as Golgi bodies (G) and mitochondria (M), were commonly observed in the cytoplasm. (B) The cisternae, lumens, and secretory vesicles could be discerned from the Golgi body. (C) Magnified views showed double membranes and cristae of the mitochondria. (D) Complex plasmodesmata (Pd) were often seen between two adjoining parenchyma cells (P).



**Figure 3.S4. TEM analysis of pulsed TTC-unstained medullar zone with no electron-dense line along with the CW.** (A) The cytoplasmic disruption occurred in the IRE inner medullar zone. (B) Magnified views showed the pulsed cytoplasm partially contained electron-dense vesicles with various diameters. The absence of an electron-dense continuous plasma membrane was commonly observed along the cell wall in the magnified views. (C) No distinct organelles were found in the cells. (D) Magnified views showed the disrupted cytoplasm and plasma membrane detached (to  $\sim 1 \mu\text{m}$ ) from the cell wall.



**Figure 3.S5. TEM analysis of pulsed TTC-stained deep red inner medullar zone with partially continuous electron-dense lines along with the CW.** (A) Partially continuous electron-dense plasma membranes were commonly found in the TTC-stained deep red inner medullar zone. (B) Magnified views showed the dotted electron-dense remains and detachment of the plasma membrane (to ~500 nm) from the cell wall. (C) Partially disrupted organelles, including Golgi bodies, were found near the plasma membrane in the cells. (D) Small vesicles, ~100 nm or less in diameter, were observed between the plasma membrane and cell wall. Vesicular bodies (VB) appeared to fuse with the plasma membrane.



## **Part II: HIGH-FREQUENCY PULSED FIELD ABLATION FOR IN-VITRO 3D TISSUE SCAFFOLD**

---

### **Overview**

From the concept of ‘tissue engineering’, designing tissue scaffolds is of great importance in a wide variety of biomedical and clinical applications such as regenerative medicine, therapeutic research.

In Part II, inspired by the biochemical features of pulsed field ablation, we developed a decellularized *in-vitro* 3D tissue scaffold using high-frequency pulsed field ablation (HF-PFA) for neurogenesis of adipose-derived mesenchymal stem cells (ADMSCs).

In Chapter 4, pre-conditioning of HF-PFA was performed in the *in-vitro* study to find optimal parameters for apoptotic cell death. In addition, 3D agarose hydrogel with NCC-24 liver cancer cell line was decellularized by HF-PFA of 1500, 1800 V/cm. The neurogenesis of ADMSC on the decellularized 3D tissue scaffold was confirmed by the immunocytochemistry of the neurogenic marker Tuj1 for the neurogenic marker, beta-III tubulin.

Our findings in Part II propose that decellularized 3D tissue scaffold can be fabricated using pre-screened HF-PFA conditions and the decellularized 3D tissue scaffold supplies an excellent environment for ADMSC to be differentiated to the neurogenic cells. Therefore, HF-PFA can be the nonthermal modality to fabricate tissue scaffolds and cause neural tissue regeneration in an *in-vitro* 3D model.



## **Chapter 4. Fabrication of decellularized 3D tissue scaffold using high-frequency pulsed field ablation**

### **4.1 Summary**

Pulsed field ablation (PFA), a tissue ablation method, uses short high electric pulses and results in cell death in target tissue by irreversibly permeabilizing the cell membrane. Inspired from the biochemical features of pulsed field ablation, we developed a decellularized *in-vitro* 3D tissue scaffold using HF-PFA for neurogenesis of adipose-derived mesenchymal stem cells (ADMSCs). Before treatment, pre-conditioning of pulse frequency parameters was performed in an *in-vitro* study, and a 2 ms interval was selected for HF-PFA. 3D agarose hydrogel with NCC-24 liver cancer cell line was decellularized by HF-PFA of 1500, 1800 V/cm. The neurogenesis of ADMSC on the decellularized 3D tissue scaffold using perfusion bioreactor was confirmed by the immunocytochemistry of the neurogenic marker Tuj1 for the neurogenic marker, beta-III tubulin. Therefore, HF-PFA successfully fabricated tissue scaffold and cause neural tissue regeneration in an *in-vitro* 3D model.

## 4.2 Introduction

PFA, a tissue ablation method, uses short high electric pulses that cause low thermal damage and induce apoptotic cell death by irreversibly permeabilizing the cell membrane in the targeted tissue [85]. PFA was recently investigated as a decellularization tool to fabricate tissue scaffold sparing the vessel, ducts, and extracellular matrix (ECM) for tissue engineering [20,21,122]. The endothelial cells were removed in the treated zone, but the structures of the vessels remained resulting in rapid tissue regeneration [20,21].

Meanwhile, pulse parameters, such as voltage, pulse number, frequencies, can affect the efficacy of cell death. In one study, various frequencies from 1Hz to 2.5 kHz showed different apoptotic dead cell rates until 400 voltages [123]. Possible mechanisms for PFA frequency are based on the high-frequency pass filter of the cellular membrane [124] and transient rise of  $\text{Ca}^{2+}$  concentration of cytosol of the cells [125]. In general, the  $\text{Ca}^{2+}$  concentration of cytosol of the cells is maintained at 10-100 nM [126]. Single PFA pulse can cause a small (10-20 nM) transient rise of  $\text{Ca}^{2+}$  but no physiological events occur when pulse interval is long enough to membrane resealing [125]. Temporal summation of short interval pulses can reach a physiological significant level (about 200 nM), producing sufficient cell death. Still, no study was performed to investigate the decellularization of 3D scaffolds using high-voltage HF-PFA.

To address these challenges, we developed a 3D agarose hydrogel with an NCC-24 liver cancer cell line, which imitated the cancer tissue. We prescreened the optimal pulse parameters for the electroporation by varying the interval of the pulses in *in-vitro* experiments. After selecting the optimal pulse interval, HF-PFA of 1200, 1500, and 1800

V/cm were performed to decellularize the scaffold. It is hypothesized that the decellularized tissue scaffold would supply the ADMSC with the proper environment to be differentiated into neural cells. We fabricated decellularized 3D scaffold and seeded the ADMSC on the scaffold with a perfusion bioreactor to circulate the neurogenic media. Thereafter, immunocytochemistry was performed to investigate the neurogenic marker beta-III tubulin (Tuj1).

## **4.3 Materials and Methods**

### **4.3.1 HF-PFA procedure**

The EPO-IRE® system (EPO-S1, The Standard Co., Ltd., Gunpo-si, Korea) was used with monopolar electrodes (Smart EPO Probe, The Standard Co., Ltd.) to deliver HF-PFA to the cancer cells on the 3D hydrogel. The PFA parameters used in this study were as follows: electric fields strength: 1200, 1500, and 1800 V/cm, pulse width: 100  $\mu$ s, pulse interval: 2 ms. A total of 90 pulses were divided into 9 times of 10 each to avoid the thermal effects of intensive electrical current. Pulse intervals of 100  $\mu$ s, 1 s were performed when comparing the effect of frequencies to the cell death rate.

### **4.3.2 Cell culture**

The human liver cancer line NCC-24 and prostate cancer line PC-3 was received from Korean Cell Line Bank and cultured in RPMI 1640 medium (Thermo Scientific, Waltham,

MA, USA) supplemented with 10% fetal bovine serum (Thermo Scientific) and 1% penicillin-streptomycin (100 IU/100 µg/ml). The cells were cultured with the 1% agarose (Sigma-Aldrich, MO, USA) solution of growth medium on the 2% agarose substrate solution in the 48 well culture dishes at 37 °C in a humidified atmosphere containing 5% CO<sub>2</sub>.

Human adipose-derived mesenchymal stem cells (hADMSCs) were purchased from CEFOBIO (CEFIO Co., Ltd. Seoul, Korea) and cultured in a medium of human-adipose-tissue-derived MSC growth medium (CEFOgro™ ADMSC [CB-ADMSC-GM]; CEFO Bio) with the provided supplementation. The cells were washed with phosphate-buffered saline (PBS; Thermo Scientific) two times and detached using 0.05% trypsin-EDTA. The subcultured hADMSCs were plated on the Matrigel (Corning, Glendale, AZ, US) in the 24-well plates and cultured with MSC Neurogenic Differentiation Medium (PromoCell GmbH, Heidelberg, Germany) with perfusion bioreactor using a peristaltic pump (Boxer 9000, Uno International, UK) for three days.

#### **4.3.3 Simulation of electrical field, temperature distribution of 3D gel model**

A finite element analysis (FEA) based model was adopted using COMSOL Multiphysics 5.6 (Stockholm, Sweden) to simulate the electrical field strength and thermal distribution of high-frequency pulsed field ablation using monopolar electrodes when applied 1200, 1500, and 1800 V with 100 µs width, 2 ms delay and 90 pulses on the 3d gel model. The electrical and thermal properties of the 3D gel were determined according to the references [127–130] as shown in Table 4.1, 4.2. The electrodes were formed with denser mesh to

evaluate more accurate results. A stationary study solver was adopted for electric field strength evaluation and a time-dependent study solver was used for thermal distribution around monopolar electrodes in the 3D gel model.

#### **4.3.5 Cell death assays**

Cell death assays were performed to investigate the optimal frequencies of pulse interval at various voltages using Guava Muse Cell Analyzer (Luminex, Austin, TX, USA). PC-3 cells (passage 32) were used for the study. First, low-frequency PFA (LF-PFA) of 1 s pulse interval was compared to HF-PFA of 2 ms pulse interval for the cell death rate using PI (diluted 1:1000 in PBS, Sigma-Aldrich, MO, USA) 20 min after the treatment. Second, various pulse interval frequencies; 100  $\mu$ s, 2 ms, 1 s were compared at PFA of 1500 V/cm using Muse Annexin V and Dead Cell Kit (Luminex) 6 hours after the treatments, FITC-conjugated dextran (diluted in 1:40 in PBS, 10 kDa, Sigma-Aldrich) 20 min after the treatments, and fluo-3AM (diluted in 1:200 in HBSS buffer, Invitrogen, MA, USA) 30 min after the treatments.

#### **4.3.6 Immunocytochemistry**

The cells on the Matrigel were fixed with a 4% paraformaldehyde solution (Sigma-Aldrich) for 30 min at room temperature. The samples were treated with 0.2% Triton X-100 (Sigma-Aldrich) for 15 min, and then stained with the neurogenic marker, beta-III tubulin (ab18207, 1:1000, Abcam, Cambridge, MA, USA) for 1 h, FITC-conjugated goat anti-

rabbit antibody for 1 h, and 4',6-diamidino-2-phenylindole (1:500, DAPI; Merck Millipore Corp., Burlington, MA, USA) for 10 min. A Nikon fluorescence microscope was used to acquire images of the stained cells.

#### **4.3.7 Statistical analysis**

Experimental results were expressed as mean  $\pm$  standard deviation from three repetitions. In case of 2 levels, a two-tailed paired Student's *t*-test was conducted to determine the significance of differences in means (\* $P < 0.05$ ; \*\* $P < 0.01$ ; \*\*\* $P < 0.001$ ). Statistical analysis was performed using Microsoft Excel 2013 (Microsoft Co., Ltd., Redmond, WA, USA) software. In case of 2 or more levels, analysis of variance (ANOVA, one-way) was employed to determine the significance of the differences in means. Fisher's least significant difference test (LSD,  $p < 0.05$ ) was utilized to compare the means of variables. LSD tests were performed using RStudio Version 1.4.1106 free software.

### **4.4 Results**

#### **4.4.1 Simulation of electric field and temperature distribution**

For the simulation of the electric field and temperature distribution, the geometry of monopolar electrodes inserted into the 3D gel was formed in the COMSOL Multiphysics 5.6 (Figure 4.1A). Meshed geometry was established with proper size in the analysis domain (Figure 4.1B). The front view of the geometry showed the complete insertion of electrodes into the 3D gel (Figure 4.1C).

Simulation of the electric field when applied 1200, 1500, and 1800 V between the electrodes showed that dumbbell type electric field between the electrodes (Figure 4.2). As the applied voltage increased, the intensity of the electric field also increased between the electrodes. At the center of the electrodes, the electric field strength was 250 V/cm when 1200 V was applied, 350 V/cm for 1500 V, and 450 V/cm for 1800 V. Simulation of the thermal distribution when applied 1200, 1500, and 1800 V between the electrodes showed that temperature slightly increased at the periphery of the electrodes. The maximum temperature increase was 3.1 °C when 1200 V was applied, 4.9 °C for 1500 V, and 7 °C for 1800 V. At the center of the electrodes, the temperature remained at 20~21 °C.

#### **4.4.2 Cell death assay at various pulse parameters**

Fluorescence-activated cell sorting (FACS) of the PC-3 after LF-PFA or HF-PFA at various voltages showed that more PI infiltrations into the cell membranes were detected at HF-PFA compared to LF-PFA (Figure 4.4). Statistically significant difference was observed at the applied voltage of 1500 V/cm ( $P < 0.05$ ).

FACS of the PC-3 after PFA of various frequencies showed that more FITC-dextran with 10 kDa infiltrations into the cell membranes were detected at PFA of 2 ms pulse interval compared to other groups (Figure 4.5). Annexin V/PI results showed similar results with statistically significant differences ( $P < 0.05$ ). Fluo-3AM, calcium indicator, showed the highest detection rate at 2 ms pulse interval with statistically significant differences, which means more agents were infiltrated into the cell membranes at the frequency ( $P < 0.05$ ).

#### **4.4.3 Decellularization of NCC-24 using HF-PFA**

Fluorescence microscopic evaluation of the NCC-24 after the various HF-PFA treatments showed that strong PI signals were detected as the strength of HF-PFA increased (Figure 4.6). It means that more dead cells were detected as the applied voltage increased between the electrodes. Hematoxylin and Eosin (H&E) histology of the 3D agarose gel with NCC-24 showed that the 3D tissue scaffolds were decellularized when applied at least 1500 V between electrodes (Figure 4.7). Live cells were detected on the control, 1200 V groups (Figure 4.7 A, B). However, the shrunk cells was detected on the 1500 V group (Figure 4.7 C), and destroyed cells on the 1800 V group (Figure 4.7 D).

#### **4.4.4 Neurogenesis of ADMSC on the decellularized 3D gel**

Immunocytochemistry of beta-III tubulin (Tuj1), neurogenic marker, and DAPI of ADMSC on the decellularized 3D gel using HF-PFA showed that the Tuj1 was stained at several sites and many sites corresponds to the DAPI-stained sites (Figure 4.8). It presented that ADMSCs were live and differentiated to neurogenic cells that compound neurogenic markers.



## 4.5 Discussion

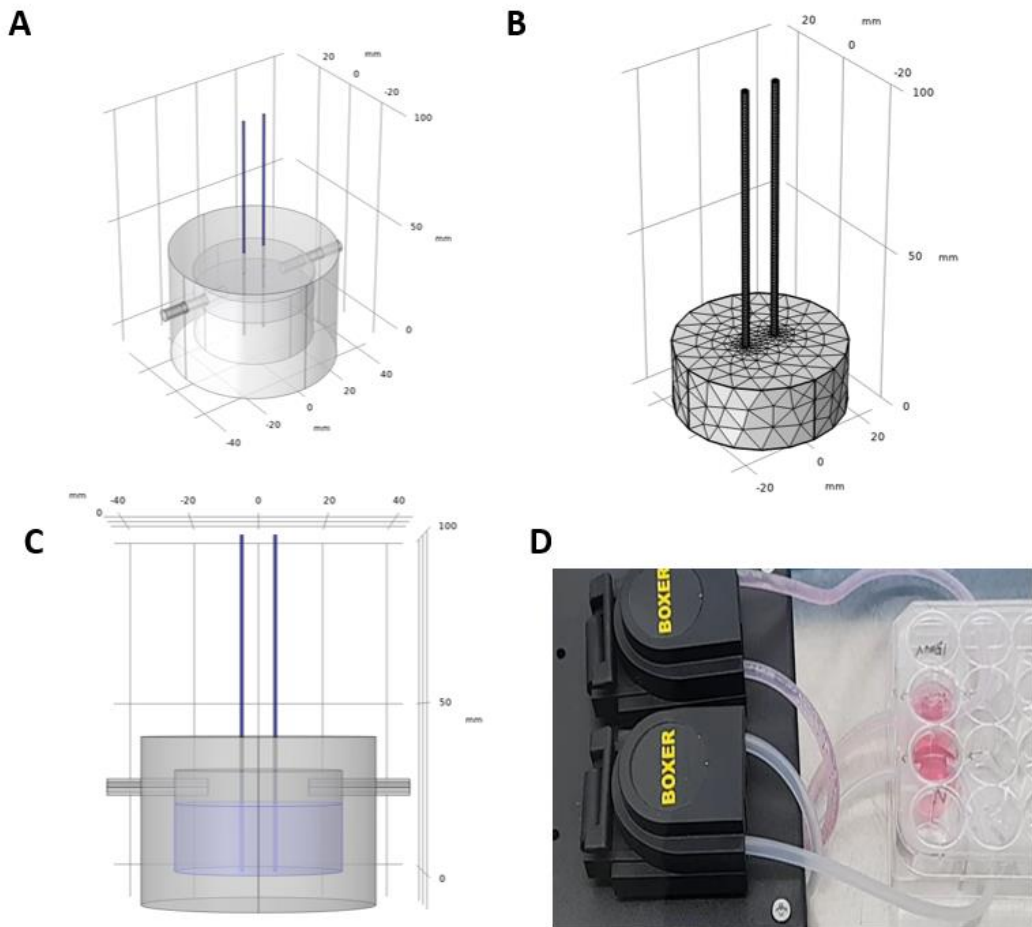
Pulsed field ablation is a nonthermal method for ablation of living cells, which gives PFA another advantage of preserving the ECM and making a quick recovery [6,7]. This advantage of PFA is crucial to make decellularized tissue scaffolds for tissue engineering.

We applied the HF-PFA to 3D tissue scaffolds grown with liver cancer cells. In our study, we demonstrated the formation of the decellularized 3D tissue scaffold after HF-PFA. Before the main study, pulse interval conditions were optimized through FACS analysis of cell death rate. HF-PFA induced more cell death rate of PC-3 cells than LF-PFA at various voltage conditions (Figure 4.4). PFA of 2 ms pulse interval caused the highest death rate and electroporation rate of PC-3 cells (Figure 4.5). We adopted 2 ms as an optimal pulse interval to fabricate the *in-vitro* tissue scaffold from these results.

The cell death rate increased as the intensity of applied voltage increased from 1200 V to 1800 V between electrodes (Figure 4.6). However, more heat was generated as the voltage increased according to the COMSOL simulation of temperature distribution (Figure 4.3). In addition, H&E of the 3D tissue scaffold after HF-PFA presented that liver cancer cells were successfully decellularized when applied voltage over 1500 V between electrodes in the scaffold (Figure 4.7). Therefore, an applied voltage of 1500 V is the optimal option for the decellularization of 3D tissue scaffold when all the circumstances were considered. A fabricated 3D tissue scaffold was a proper environment for ADMSCs to be differentiated to neurogenic cells (Figure 4.8). Tuj1, DAPI were stained in similar sites indicating that live ADMSCs were differentiated to neurogenic cells.

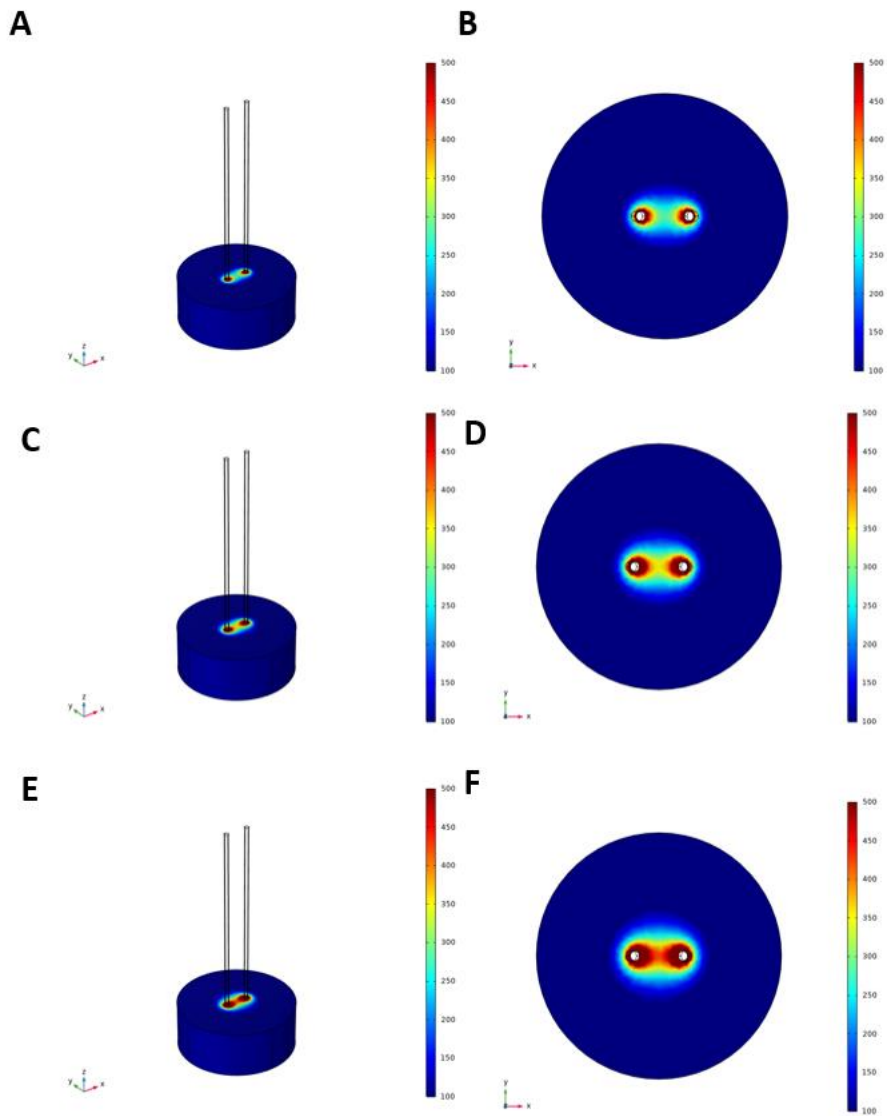
Despite all the results shown in the study, several limitations were existent. First, decellularization of the 3D gel was investigated only on H&E histology due to the softness of the scaffold. A second limitation of this study was that the analysis of neurogenesis was dependent only on an immunocytochemistry assay for beta-III tubulin.

In conclusion, we investigated the decellularization of the 3D tissue scaffold using HF-PFA and neurogenesis of ADMSC on the scaffold. These results support the validity of HF-PFA as a decellularized scaffold fabrication tool for tissue engineering.



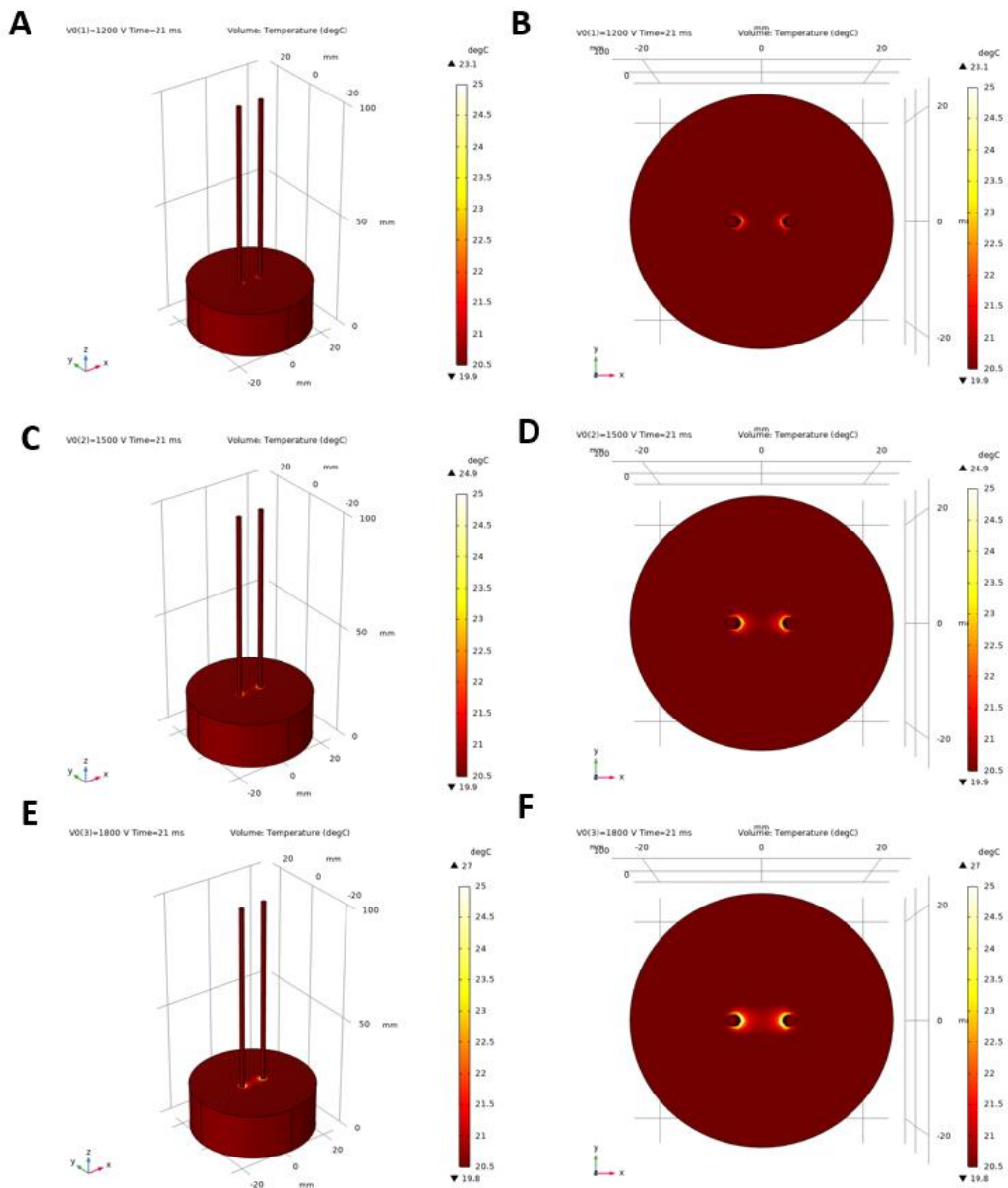
**Figure 4.1. Simulation of electric field by pulsed field ablation at the 3D gel model in the COMSOL Multiphysics 5.6.**

(A) Geometry of monopolar electrodes inserted into the 3D gel (B) Meshed geometry of the analysis domain including monopolar electrodes. (C) The front view of the 3D gel model showed complete insertion of the electrodes into the gel. (D) 3D cell culture with Matrigel using Peristaltic pump.



**Figure 4.2. Simulation of electric field by pulsed field ablation at the 3D agarose gel model in the COMSOL Multiphysics 5.6.**

(A, C, E) The electric field strength at the overall view at the 3D agarose gel model when applied 1200, 1500, 1800 V between electrodes. (B, D, F) The electric field strength at the cross-section direction to the electrodes when applied 1200, 1500, 1800 V between electrodes.



**Figure 4.3. Simulation of thermal distribution by pulsed field ablation at the 3D agarose gel model in the COMSOL Multiphysics 5.6.**

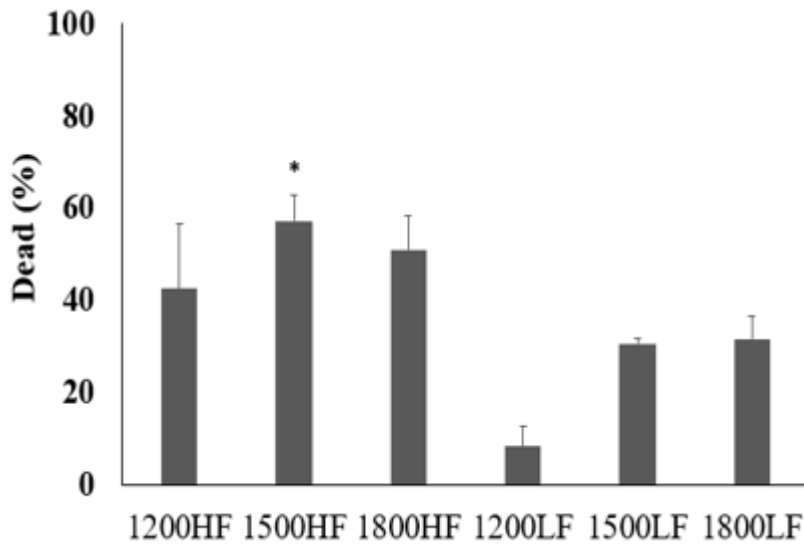
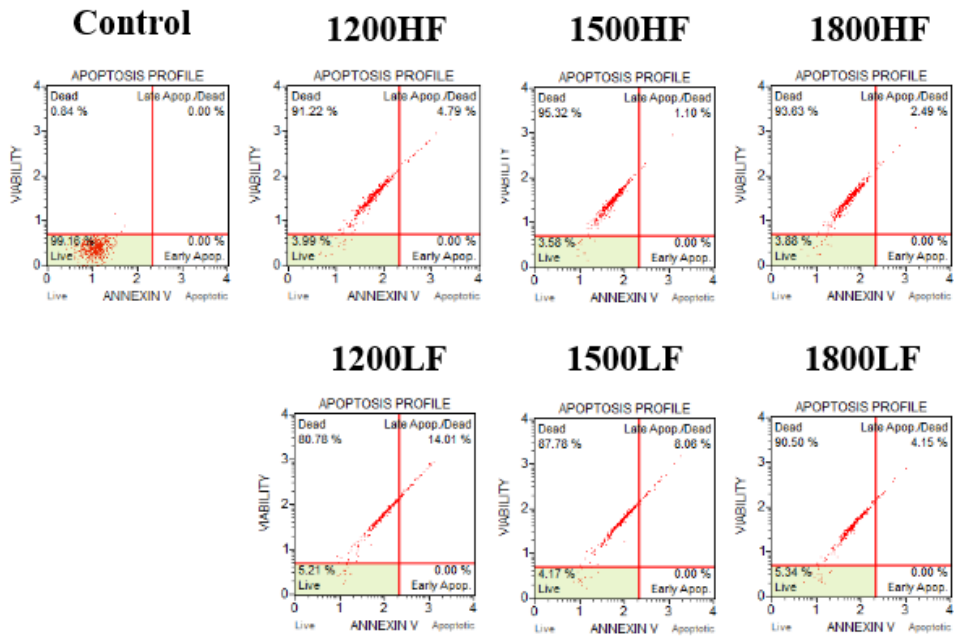
(A, C, E) Thermal distribution at the overall view at the 3D agarose gel model when applied 1200, 1500, 1800 V between electrodes. (B, D, E) Thermal distribution at the cross-section direction to the electrodes when applied 1200, 1500, 1800 V between electrodes.

**Table 4.1. Geometrical parameters of the 3D gel with the electrodes and physical parameters of the pulsed field ablation model for COMSOL simulation.**

<b>Parameters</b>	<b>Value</b>
Diameter of the gel	50 [mm]
Height of the gel	20 [mm]
Diameter of electrode	1 [mm]
Exposed length of electrode	20 [cm]
Ambient temperature	293.15 [K]
Natural convection in the air	25 [W/(m <sup>2</sup> *K)]
Applied voltage between electrodes	1200, 1500, 1800 [V/cm]
Pulse width	100 [us]
Pulse interval	2 [ms]
Pulse number	10

**Table 4.2. Material properties of the 3D gel for COMSOL simulation.**

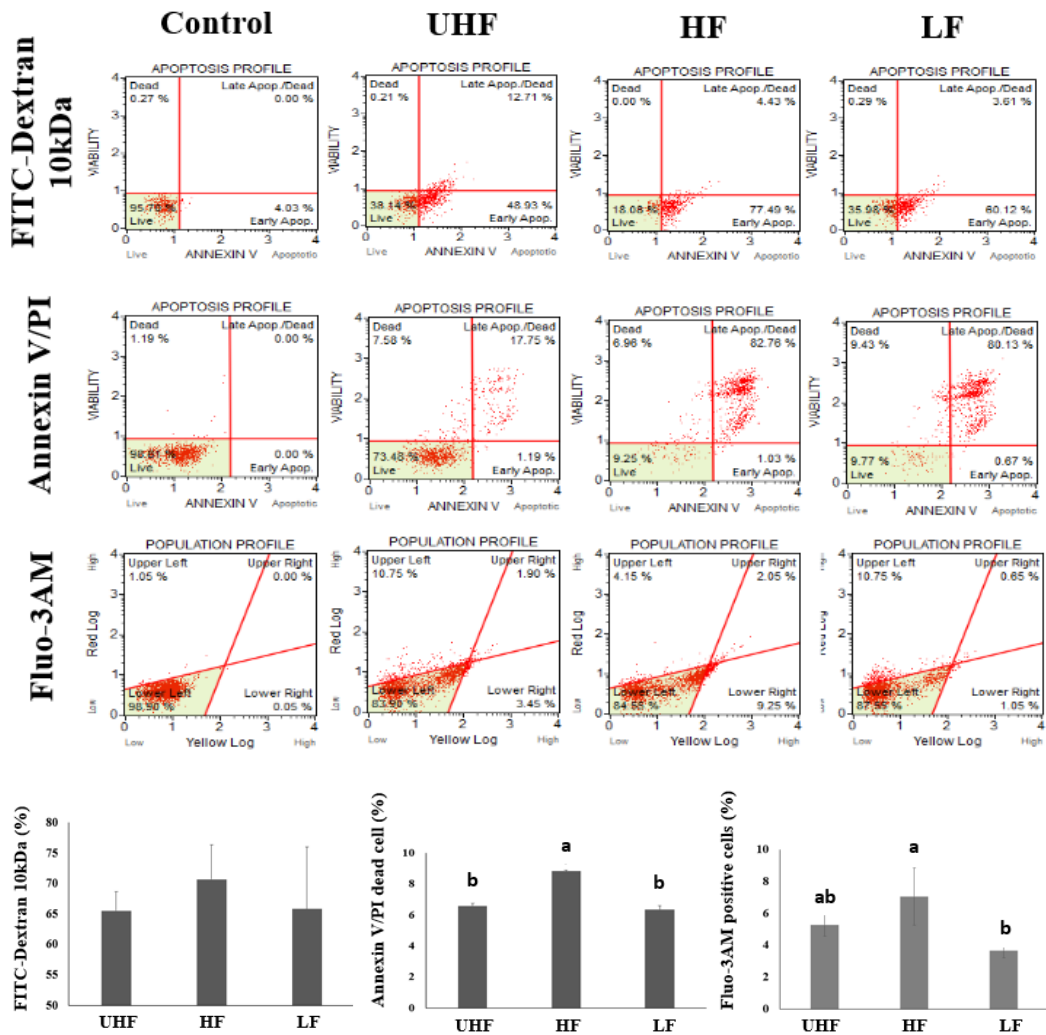
<b>Parameters</b>	<b>Value</b>
Electrical conductivity	0.15 [S/m]
Density	1033 [kg/m <sup>3</sup> ]
Heat capacity	4200 [J/(kg*K)]
Thermal conductivity	0.55 [W/(m*K)]
Relative permittivity	75



**Figure 4.4. FACS results to compare the cell death rate of LF-PFA and HF-PFA at various applied voltages using PI.**

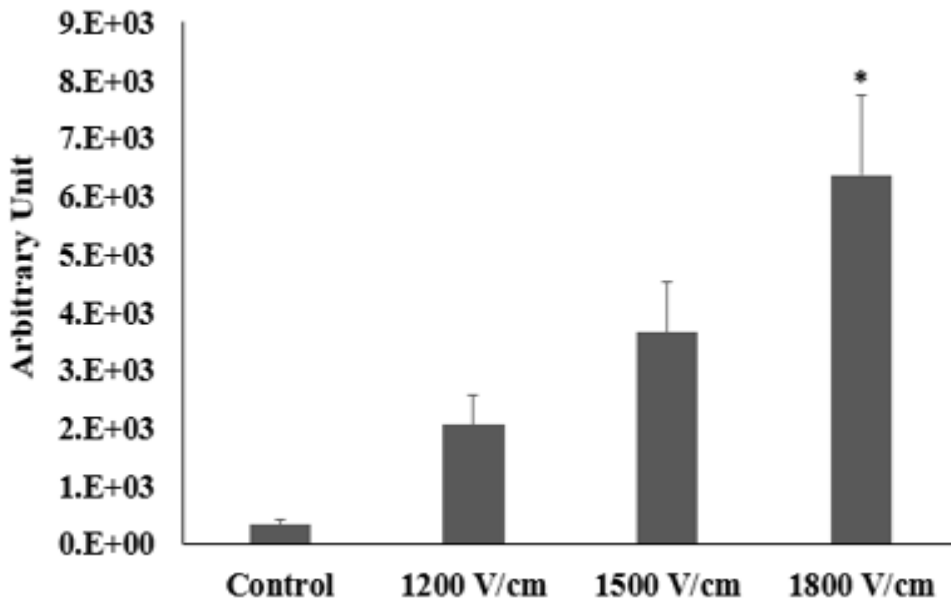
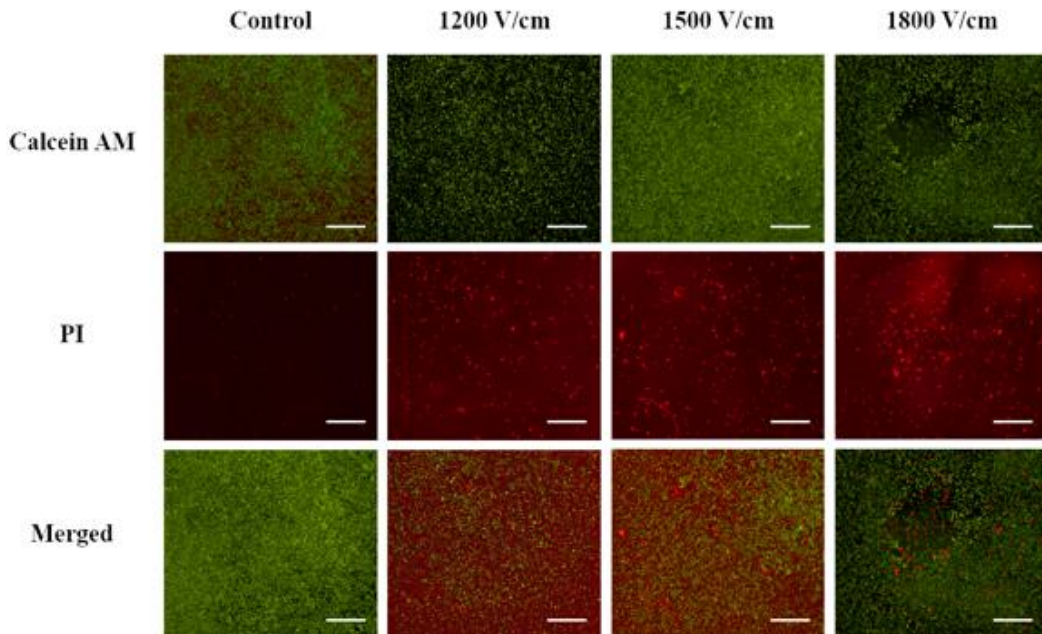
HF-PFA for 2 ms pulse interval and LF-PFA for 1 s interval at 1200, 1500, 1800 V/cm. HF-PFA showed higher death rate of PC-3 than LF-PFA. N = 3, \*P < 0.05; \*\*P < 0.01; \*\*\*P < 0.001





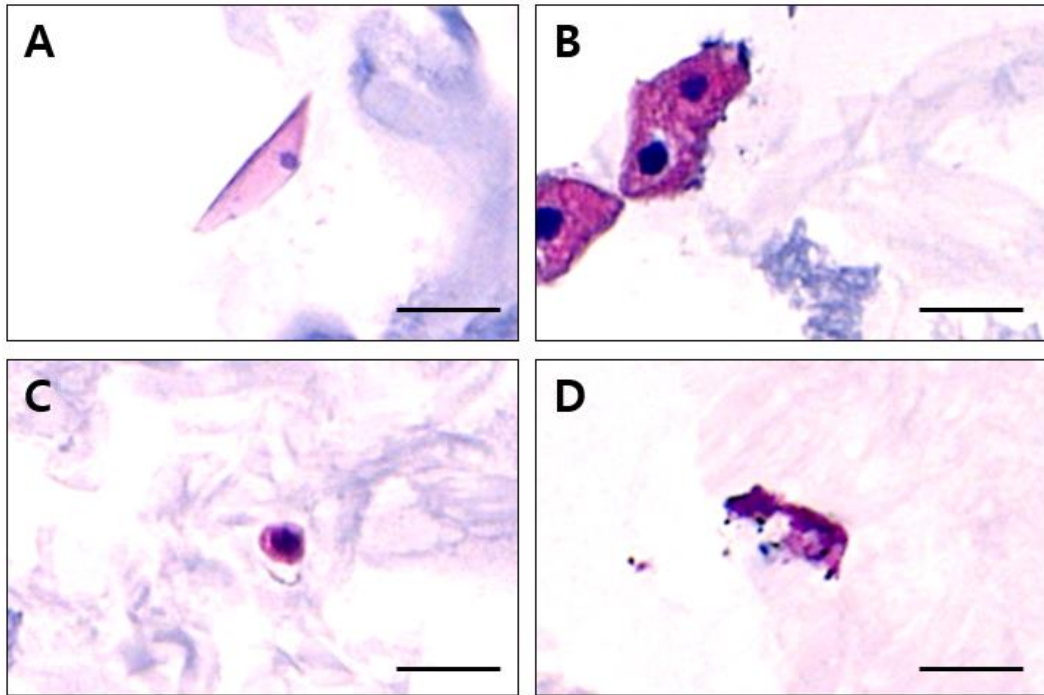
**Figure 4.5.** FACS results to compare the death rate of 1500 V/cm PFA at various frequencies voltages using FITC dextran 10kDa, Annexin V/PI, and Fluo-3AM.

PFA of 1500 V/cm at ultra-high frequency (UHF) for 100 us pulse interval, high frequency (HF) for 2 ms pulse interval, and low frequency (LF) for 1 s pulse interval. PFA of 2 ms pulse delay showed the highest death rate and electroporation of PC-3 than others. N = 3, \*P < 0.05; \*\*P < 0.01; \*\*\*P < 0.001, ANOVA Fishers Least Significant Difference (LSD) test.



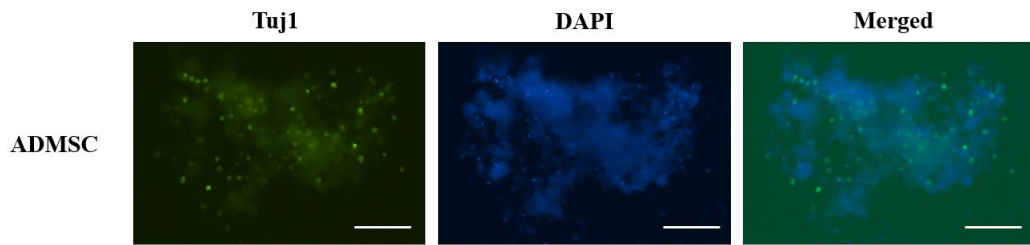
**Figure 4.6. Calcein AM, PI fluorescence after various pulsed field ablation and histogram of the PI stained area.**

Strong PI signals were detected as the strength of pulsed field ablation increased. Scale bar, 1 mm; magnification,  $\times 4$ . N = 3, \*P < 0.05; \*\*P < 0.01; \*\*\*P < 0.001



**Figure 4.7. Decellularization of the 3D agarose gel after HF-PFA.**

(A) Control, (B) 1200 V/cm, (C) 1500 V/cm, (D) 1800 V/cm. As the strength of pulsed field ablation increases, cell morphology is changed to apoptotic death. Scale bar, 20  $\mu\text{m}$ ; magnification,  $\times 50$ .



**Figure 4.8. Neurogenesis of ADMSC after decellularization using pulsed field ablation on the 3D gel model**

TuJ1, DAPI fluorescence images to detect neurogenic marker, beta-III tubulin after pulsed field ablation on the 3D gel model. TuJ1 fluorescence was detected from differentiated ADMSC on the 3D gel model after pulsed field ablation of the cancer cell line. Scale bar, 50  $\mu\text{m}$ ; magnification,  $\times 20$ .

## **Part III: HIGH-FREQUENCY PULSED FIELD ABLATION FOR IN-VIVO TISSUE SCAFFOLD**

---

### **Overview**

Pulsed field ablation (PFA) is frequently used in a diverse clinical and biomedical applications such as gene delivery, drug delivery, therapeutic research for locally advanced solid tumors.

In Part III, inspired by the established pulsed field ablation, we developed a novel PFA method by changing the pulse interval to the microseconds range resulting in high-frequency pulsed field ablation (HF-PFA), which no attempts have been made yet in the preclinical model.

Chapter 5 showed that HF-PFA of 1000, 1400, and 1800 V/cm successfully reduced human prostate cancer size compared to the sham control group 2 weeks after the treatment. Immunohistochemistry (IHC) and western blot of cleaved caspase-3 and Bcl-2 presented that cell apoptosis is maximized at 1800 V/cm after HF-PFA. Chapter 6 showed that beagle prostate tissue was successfully ablated 4 hours after HF-PFA of 1800 V/cm, 90 pulses. Acellular parts such as prostatic glands, duct, and urethra were preserved after HF-PFA and ablated acinus was regenerated 7 days, 4 weeks after HF-PFA.

Our findings in Part III propose that HF-PFA is safe and efficient to ablate *in-vivo* tissue such as the prostate and induced sufficient human prostate cancer cell apoptosis to kill the cancer tissue. Therefore, HF-PFA might be an excellent alternative to the existing PFA method requiring a lot of time for the *in-vivo* tissue ablation.

## **Chapter 5. Decellularization of the human prostate cancer using high-frequency pulsed field ablation**

### **5.1 Summary**

Pulsed field ablation (PFA), a minimally invasive ablation method, uses ultrashort high-voltage electric pulses resulting in cell apoptotic death in the tissue by forming irreversible nanopores on the cell membrane. Unlike existing PFA pulsing approximately 1~4 Hz, HF-PFA about 476 Hz were adopted to ablate the *in-vivo* human prostate cancer tissue in this study. HF-PFA of 1000, 1400, and 1800 V/cm successfully reduced human prostate cancer size compared to the sham control group 2 weeks after the treatment. Immunohistochemistry (IHC) and western blot of cleaved caspase-3 and Bcl-2 presented that cell apoptosis is maximized at 1800 V/cm after HF-PFA. Therefore, HF-PFA successfully ablated the human prostate tissue efficiently. It might be an excellent alternative to the existing PFA method requiring a lot of time for the *in-vivo* tissue ablation.

## 5.2 Introduction

Prostate cancer, the most frequently diagnosed in men, is the second leading cause of cancer-related death in men following lung cancer worldwide [147]. Of the prostate cancer patients, about 77% patients developed locally advanced prostate cancer (LAPRC) [131]. Radical prostatectomy was frequently used to remove the cancerous tissues and improve survival rates of the patients, but the treatment caused many side effects such as urinary incontinence, or sexual dysfunction of the patients [134–136].

To reduce the side effects of the standard procedure, various local treatment techniques, such as laser, high-intensity focused ultrasound (HIFU), cryoablation, photodynamic therapy (PDT), radiofrequency ablation (RFA), and nonthermal pulsed field ablation (PFA), have been introduced to preserve the extracellular matrix (ECM) of the treated area [137,138].

Unlike thermal ablation techniques, PFA uses high-voltage microseconds short electric pulses to induce apoptotic cell death of cancer tissues sparing acellular structures such as neurovascular bundles, blood vessels, and ductal structures resulting in rapid and sufficient regeneration of the targeted tissue [139–141].

In this study, we assessed the efficacy of the HF-PFA on the human prostate cancer tissue. According to the energy levels, HF-PFA of 1000, 1400, and 1800 V/cm were delivered to the cancer tissues. Histological examination, TUNEL assay, and western blot of cleaved caspase-3 and Bcl-2 were performed to investigate whether apoptotic cell death occurred. Tumor regressions were observed during 2 weeks.

## **5.3 Materials and Methods**

### **5.3.1 Electrical ablation**

Electrical ablation was performed using EPO-IRE<sup>®</sup> generator (EPO-S1, The Standard Co., Ltd., Gunpo-si, Korea) with the monopolar electrode (19 G, The Standard Co., Ltd.). Electrical ablation conditions were composed of three groups for effectiveness: 1000 V/cm for low energy (LE), 1400 V/cm for medium energy (ME), and 1800 V/cm for high energy (HE) (Table 5.1).

### **5.3.2 Cell culture**

Prostate cancer cell line from humans (DU145) was purchased from the American Type Culture Collection (ATCC). The cells were harvested in Roswell Park Memorial Institute (RPMI) 1640 medium supplemented with 10% fetal bovine serum (FBS, heat-inactivated), 100 µg/mL streptomycin, and 100 units/mL penicillin at 37 °C in 5% CO<sub>2</sub> atmosphere. Passages of the cells from 10 to less than 15 were utilized in the experiments.

### **5.3.3 *In-vivo* experiment procedure**

All experiments dealing with animals were granted by the Institutional Animal Care and Use Committee (IACUC) of Asan Medical Center (# 2020-12-238). The schematic of the



study was presented in Figure 5.1. Five-week-old male Balb/c nude mice were purchased from the local company (Central Lab. Animal Inc., Korea). The nude mice were acclimated to local environments for 7 days. before tumor injection with the human prostate cancer cell lines. Subsequently, the tumor cells were injected subcutaneously into the right flank of the mice with 0.1 ml Matrigel containing  $3 \times 10^6$  human prostate cancer cells (DU145 cells, passage 15). Total 28 mice were randomized into 4 groups 4 weeks after tumor implantation: control, LE, ME, HE groups. The histological analysis and TUNEL assay were performed 18 hours after HF-PFA and tumor volume and body weight were measured at 1, 5, 8, 12, and 15 days after HF-PFA.

#### **5.3.4 Gross and Histologic Examination**

The human prostate cancer tissues were evaluated with the histopathological appearance 18 hours after the HF-PFA procedure. Tissue specimens were cut and fixed in 10% formalin for at least 24 hours. Subsequently, the samples were processed for microscopic and gross observation. The samples were processed with hematoxylin and eosin (H&E) for histomorphological analysis. Digitalized slides were assessed histologically from a scanner (Pannoramic 250 FLASH III, 3D HISTECH Ltd., Budapest, Hungary) and were analyzed using its viewer software (CaseViewer, 3D HISTECH Ltd).

#### **5.3.5 Immunohistochemistry**

Immunohistochemistry (IHC) was carried out on the formalin-fixed paraffin-embedded

tissue sections to verify apoptotic cell death after HF-PFA treatment on the human prostate tissues. Terminal deoxynucleotidyl transferase dUTP nick end labeling (TUNEL assay) were carried out using a kit (In-Situ Cell Death Detection, POD kit, Roche, Germany). The specimens were visualized using a staining equipment (BenchMark XT, Ventana Medical Systems, Tucson, AZ, USA).

### **5.3.6 Western blot**

Tumor tissue extract was processed in a RIPA lysis buffer including protease inhibitor cocktail (Sigma-Aldrich, MO, USA). The lysates of tumor tissue were centrifuged at 13,000 x g for 20 min. Then, the protein concentration was calculated using the Bradford assay kit (Bio-Rad Inc., Hercules, CA, USA). Thereafter, lysates of Tissue were blended with a same amount of protein (20 µg in 15 µL) of 5X SDS loading sample buffer. The specimens were heated at 100 °C for 7 minutes prior to loading. Subsequently, the samples were separated on a precast 4 – 20% polyacrylamide-gradient SDS-gels (Bio-Rad Inc.) After the proteins electrotransferring to a polyvinylidene fluoride (PVDF) membrane (Merck Millipore Corp., Burlington, MA, USA), nonspecific bindings to the membrane were blocked with 5% BSA in TBST buffer at room temperature for 1 hour. The membrane was incubated with a cleaved caspase-3 antibody (1:1,000, Cell Signaling Technology, Danvers, MA, USA) at 4 °C with shaking (110 rpm orbital shaker) overnight.

β-actin (diluted in 1:10,000, Santa Cruz Biotechnology, Dallas, TX, USA) and α-tubulin (diluted in 1:5,000, Cell Signaling Technology) were used as internal controls. Then, the membrane was incubated with horseradish peroxidase-conjugated IgG as

secondary antibodies in 5% for BSA blocking buffer with shaking at room temperature for 1 hour. The blotting membranes were stripped and re-probed with anti-immunoreactive bands were visualized by exposition to X-ray utilizing Immobilon Western enhanced chemiluminescent (ECL) solution (Merck Millipore Corp.). Quantification of the protein band intensity was processed by the image software (ImageJ, National Institutes of Health, Bethesda, MD, USA). The normalizations of the proteins relative to  $\beta$ -actin were performed.

### **5.3.7 Temperature measurements**

The temperature was measured using an optic fiber (FTX-100-LUX+, OSENSA Innovations Corp., Burnaby, BC, CA) connected to the transmitter (PRB-G20-2.0M-ST-C, OSENSA Innovations Corp.). The fiber was inserted into the tissue in contact with the electrode.

### **5.3.8 Statistical analysis**

Experimental results were represented as the form of mean  $\pm$  standard deviation from three repetitions. In case of 2 levels, a two-tailed paired Student's *t*-test was utilized to decide the significant differences in means (\* for  $P < 0.05$ ; \*\* for  $P < 0.01$ ; \*\*\* for  $P < 0.001$ ). The analysis was processed using the Excel software (2013, Microsoft Co., Ltd., Redmond, WA, USA). In case of 2 or more levels, Analysis of variance (ANOVA, one-way) was utilized to decide the significant differences in means. For statistical grouping, Fisher's

least significant difference test (LSD,  $P < 0.05$ ) was utilized to compare the means of variables using RStudio software (version 1.4.1106).

## **5.4 Results**

### **5.4.1. Decellularization of human prostate cancers**

Human prostate cancers on the skin of nude mice were decellularized with HF-PFA at various voltage conditions. The volume of the prostate cancer tissues decreased depending on the intensity of voltage 14 days after HF-PFA with statistically significant differences (Figure 5.2A). Tumor volumes decreased to half of the control group in the case of 1000 V/cm, one-third for 1800 V/cm. Tumor weight showed a similar tendency (Figure 5.2C). Meanwhile, the body weight of the nude mouse was maintained for 14 days after the treatment (Figure 5.2B).

TUNEL assay showed apoptotic cell death of DU145 prostate cancer cells 18 hours after HF-PFA at the various voltages (Figure 5.3). Apoptotic cells increased as the voltages increased resulting in almost extinction of the cells at the applied voltage of 1800 V/cm (Figure 5.3D).

### **5.4.2. Western blot for apoptotic marker**

Western blot was performed to quantify the later apoptosis marker, cleaved caspase-3, and anti- or pro-apoptosis marker, Bcl-2 (Figure 5.4). Band intensity of cleaved caspase-3 and

Bcl-2 increased as the pulsed electric field increased (Figure 5.4A). The density of cleaved caspase-3 normalized to  $\beta$ -actin showed the same tendency with a statistically significant difference (Figure 5.4B).

### **5.4.3. Temperature change during the HF-PFA**

Temperature change during the HF-PFA on the human prostate cancer tissue of the nude mouse skin was shown in Figure 5.5. HF-PFA of 1400 V/cm was applied 9 times of 10 pulses, a total of 90 pulses on the prostate cancer tissue. The results showed that the temperature increased under 43 °C. This fact indicated that there was no thermal damage.

## **5.5 Discussion**

PFA has been performed on the human prostate cancer tissues on the nude mouse skin using monopolar electrodes in the previous studies. One study showed that the PFA caused apoptotic cell death on the prostate cancer cells and TUNEL positive areas were maximized 12~24 hours after the PFA and decreased over time until 72 hours [110]. Another study showed that the radius of dead cell areas increased in the H&E staining as the PFA duration, the number increased [148]. However, long-term tumor regressions of PFA were not investigated in any of the studies.

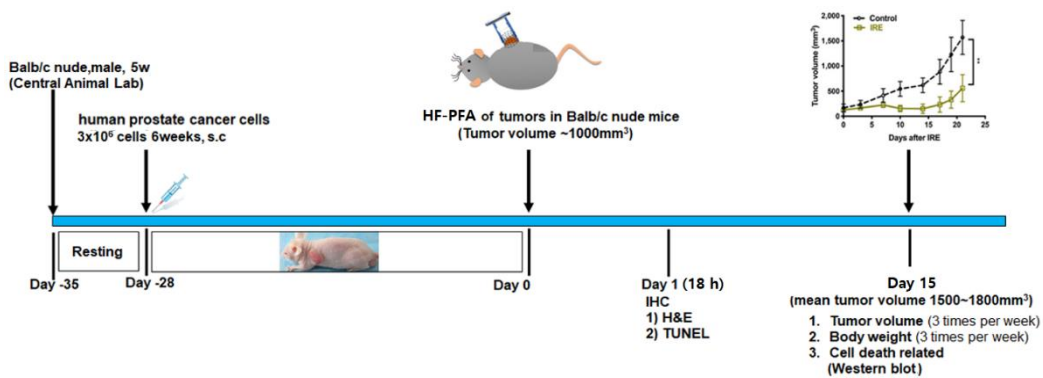
In this study, HF-PFA of 1000, 1400, and 1800 V/cm decellularized the *in-vivo* human prostate cancer tissue on the skin of the nude mouse. The tumor regression during

2 weeks (Figure 5.2) and apoptotic changes (Figure 5.3) showed that electric field strength of at least 1400 V/cm reduced the tumor volume and induced sufficient apoptosis of the cancer cells.

The tumor regression of HF-PFA can be caused by thermal damage due to short pulse intervals. Therefore, the temperature change was performed during HF-PFA of 1400 V/cm (Figure 5.4). Thermal damage can occur at a temperature of 43 °C [149]. The results showed that there were little thermal damages during HF-PFA of 1400 V/cm.

In the limitation of the study, there was no measurement data of the temperature increase during HF-PFA of 1800 V/cm. In the case of the HF-PFA 1400 V/cm group, the temperature change was measured only once, so additional repetitions are needed for a statistically significant difference. Moreover, quantification of the cell apoptotic death is needed to conclude the differences between groups in statistical significance.

In conclusion, the human prostate cancer tissues were sufficiently decellularized after HF-PFA of at least 1400 V/cm with little thermal damage. These facts suggest that HF-PFA can be applied as an effective modality to treat LAPRC.



**Figure 5.1. Schematic of HF-PFA of human prostate cancer cells on the nude mouse skin.**

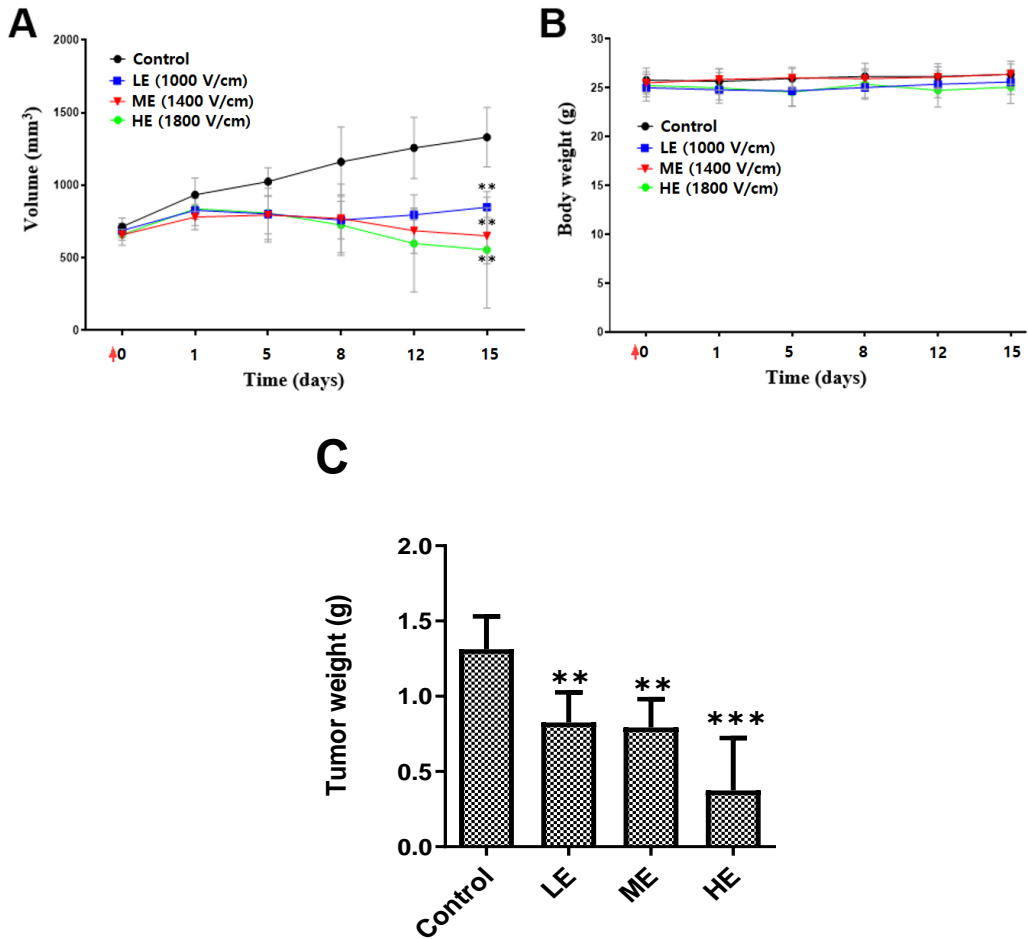
The cancer tissues were raised for 15 days and the tissues were treated with the EPO-IRE generator (The Standard Co., Ltd. Gunpo-si, Korea) with the monopolar electrode (19 G, The Standard Co., Ltd.). H&E and TUNEL assay were performed on day 1 and tumor and body volumes were measured for 15 days.

**Table 5.1. Electrical ablation conditions for the HF-PFA of human prostate cancer tissue on the nude mouse skin.**

The control group was penetrated by electrodes without HF-PFA treatment. Each group was treated with HF-PFA; 1000, 1400, and 1800 V/cm.

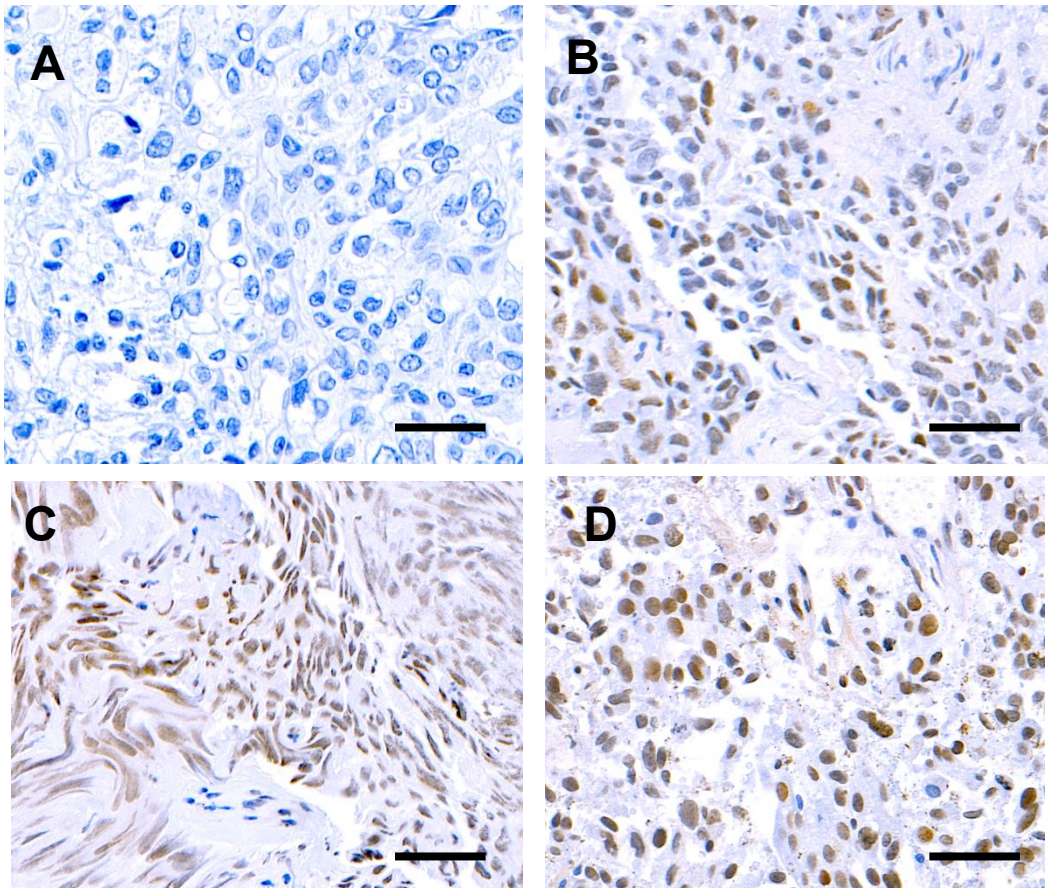
	<b>Control</b>	<b>Group 1 (LE)</b>	<b>Group 2 (ME)</b>	<b>Group 3 (HE)</b>
Electric field	Only penetration	1000 V/cm	1400 V/cm	1800 V/cm
Pulse number		180	180	180
Pulse width		100 $\mu$ s	100 $\mu$ s	100 $\mu$ s
Pulse width		2 ms	2 ms	2 ms
Burst (Pulse group)		90 ea x 2 times	90 ea x 2 times	90 ea x 2 times
Burst interval		10 s	10 s	10 s
Electrode Distance		5 mm	5 mm	5 mm
Electrode Exposure		15 mm	15 mm	15 mm





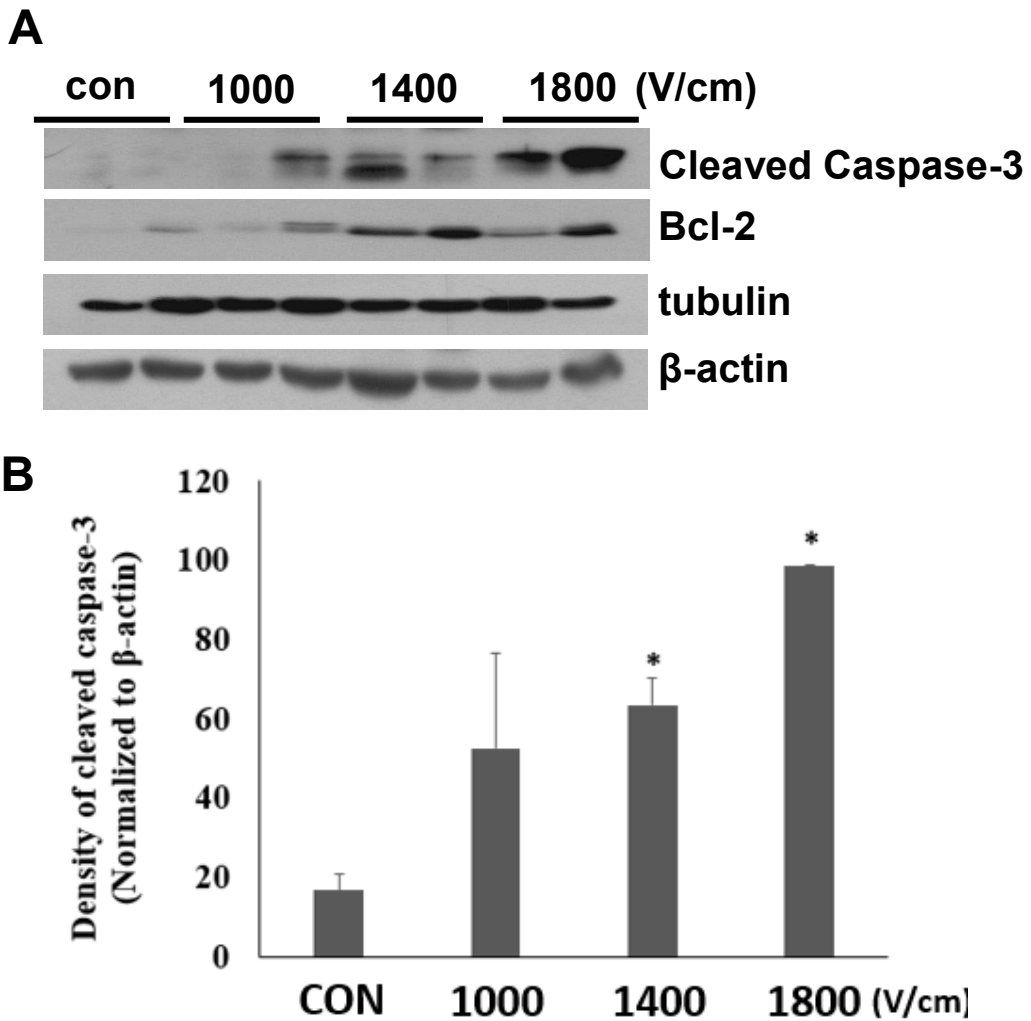
**Figure 5.2. Tumor volume and weight change over time after HF-PFA treatment at various conditions.**

(A) Tumor volume decays after HF-PFA depending on the intensity of energy. (B) Body weight were maintained. (C) Tumor weight also decays. N = 5, \*P < 0.05; \*\*P < 0.01; \*\*\*P < 0.001.



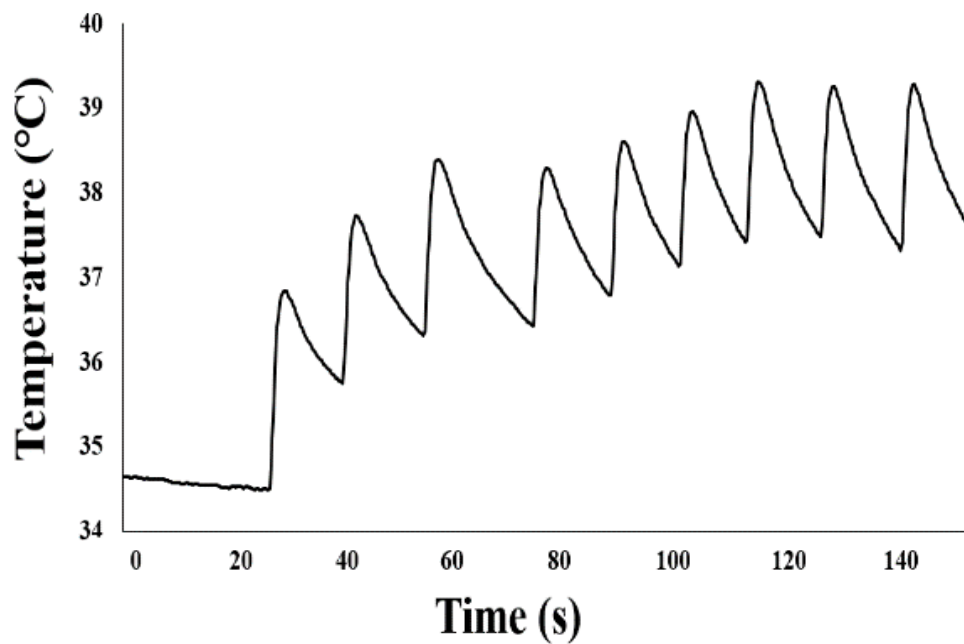
**Figure 5.3. TUNEL assay of the human prostate cancer after HF-PFA treatment.**

(A) Sham control, (B) 1000 V/cm, (C) 1400 V/cm, (D) 1800 V/cm. The results showed that apoptotic cells increased as the applied voltage increased. Scale bar 20  $\mu\text{m}$ .



**Figure 5.4. Western blot of cleaved caspase-3, Bcl-2 after HF-PFA.**

(A) Band intensity of cleaved caspase-3 (later apoptosis marker) and Bcl-2 (anti- or pro- apoptosis marker) increased as the pulsed electric field increases. (B) Density of cleaved caspase-3 normalized to  $\beta$ -actin showed same tendency. N =2, \*P < 0.05; \*\*P < 0.01; \*\*\*P < 0.001.



**Figure 5.5. Temperature change during the HF-PFA on the human prostate cancer tissue on nude mouse skin.**

HF-PFA of 1400 V/cm was applied 9 times of 10 pulses, a total of 90 pulses on the prostate cancer tissue.

## **Chapter 6. Decellularization of the beagle prostate using high-frequency pulsed field ablation and tissue regeneration**

### **6.1 Summary**

Pulsed field ablation (PFA), a minimally invasive ablation method, uses ultrashort high-voltage electric pulses resulting in apoptotic cell death in the tissue by forming irreversible nanopores on the cell membrane. Unlike existing PFA pulsing approximately 1~4 Hz, HF-PFA about 476 Hz were used to ablate the *in-vivo* prostate tissue according to previous *in-vitro* experiments. The beagle prostate tissue was successfully ablated 4 hours after HF-PFA of 1800 V/cm, 90 pulses. Acellular parts such as prostatic glands, duct, and urethra were preserved after HF-PFA. Ablated acinus was regenerated similar to the original tissues 7 days, 4 weeks after HF-PFA. Hematology of troponin I, creatine kinase (CK), and CK-MB showed that there was no damage related to cardiac tissue after HF-PFA. Therefore, HF-PFA successfully ablated the beagle prostate tissue safely and efficiently. It might be an excellent alternative to the existing PFA method requiring a lot of time for the *in-vivo* tissue ablation.

## 6.2 Introduction

Prostate cancer is the most frequently diagnosed cancer in the United States with an estimated 248,530 cases in 2021 [131]. Locally advanced prostate cancer (LAPRC) is 77% of the new prostate cancer cases in 2003-2017 [131]. Radical prostatectomy was performed to improve survival rates or delay the metastatic progression of the LAPRC in clinical trials [132,133]. However, the standard treatment caused side effects such as erectile dysfunction, and urinary incontinence resulting in reduced quality of life of patients [134–136].

To minimize the side effects, several focal treatment modalities have been developed to spare the adjacent vessels or neurovascular bundles near the targeted sites in the prostate [137]. Focal thermal therapies such as radiofrequency ablation (RFA), photodynamic therapy (PDT), cryoablation, laser, high-intensity focused ultrasound (HIFU), and pulsed field ablation (PFA) [138].

PFA delivers high-voltage ultrashort electric pulses to ablate prostatic cancer tissues. The electric fields formed between the electrode pairs cause the cancer cells to death by irreversibly permeabilizing the membrane of the cells [139]. This unique mechanism of killing the cells can spare the acellular structures such as blood vessels, neurovascular bundles, and extracellular matrix (ECM) in the targeted regions resulting in rapid tissue regeneration after the treatments [139–141].

In this study, we evaluated the safety and efficacy of HF-PFA on the beagle prostate. Animals were grouped 4 hours, 7 days, and 4 weeks after HF-PFA to investigate the safety and efficacy over time. The cardiac safety was assessed using electrocardiography (ECG) measurement. Hematology including CK, CK-MB, Troponin I was analyzed for the detailed analysis to evaluate the effect of HF-PFA on the beagle prostate on cardiac safety. Histological examination and immunohistochemistry were performed to evaluate the effectiveness of HF-PFA to cause cell apoptosis to the target tissue and tissue regeneration after HF-PFA at the treated sites.

## 6.3 Materials and Methods

### 6.3.1 HF-PFA Devices and electrodes

The EPO-IRE<sup>®</sup> system (EPO-S1, The Standard Co., Ltd., Gunpo-si, Korea) was utilized with the monopolar electrodes (Smart EPO Probe, The Standard Co., Ltd.) to deliver HF-PFA on the beagle prostate (Figure 6.1A-D). The system was able to set an electric field intensity up to 3000 V with pulse widths of 100–1,000  $\mu$ s with 100–2,000  $\mu$ s pulse intervals.

### 6.3.2 Simulation of electrical field, temperature distribution of HF-PFA

A finite element analysis (FEA) based model was adopted using COMSOL Multiphysics 5.6 (Stockholm, Sweden) to simulate the electrical field strength and thermal distribution of HF-PFA using monopolar electrodes when applied 1800 V with 100  $\mu$ s width, 2 ms delay, and 10 pulses. The thermal and electrical properties of the prostate tissue were determined according to the online database (<https://itis.swiss/virtual-population/tissue-properties/database/>) as shown in Table 6.2, 5.3. The electrodes were formed with denser mesh to evaluate more accurate results. A stationary study solver was adopted for electric field strength evaluation and a time-dependent study solver was used for thermal distribution around monopolar electrodes in the prostate model. Heat transfer was solved by the following equations:

$$\rho C_p \frac{\partial T}{\partial t} + \rho C_p \mathbf{u} \cdot \nabla T + \nabla \cdot \mathbf{q} = Q$$

$$\mathbf{q} = -k \nabla T$$

C<sub>p</sub> : Specific heat capacity [J/(kg\*K)]  
k : Thermal conductivity [W/(m\*K)]  
T : Temperature [°C]  
t : time [s]  
Q : Electrical energy  
q : Energy flow [W]



### **6.3.3 Animal Study**

The animal study was granted by the Institutional Animal Care and Use Committee of the Asan Institute for Life Sciences (2020-14-277) complying with the guidelines of the National Institutes of Health. Twelve certified-healthy, 12 months aged male beagles with a weight of 14.5–16.2 kg (median weight = 15.35 kg), were used for the study. Three beagles were used as a control group only punctured with electrodes without pulsing, and the remaining nine beagles underwent HF-PFA treatments. The nine beagles were divided into 3 groups of 3 each according to the sacrifice time at 4 hours, 7 days, and 28 days after the HF-PFA procedure. The sacrifice was performed by injecting an overdose of xylazine hydrochloride (Rompun; Bayer, Seoul, Korea).

The twelve beagles were examined to investigate whether the animals were suitable for the experiments after 7 days acclimatization period. After examination, the animals were displaced to the individual cages with an area larger than 0.74 m<sup>2</sup>, at 23 ± 2 °C, relative humidity of 50 ± 10%, with 12 hours lighting time (8 am - 8 pm), and 10–15 times/h ventilation.

### **6.3.4 HF-PFA procedure**

All dogs were generally anesthetized before the procedure. The abdomens of dogs was opened with a 70 mm midline incision from the xiphoid process down and the urethra and urinary bladder were identified. Subsequently, the prostate was discerned by tracing along the urinary tract. Two monopolar electrode needles were penetrated into the randomized

side of the prostate under ultrasound guidance (Figure 6.1E-G). The HF-PFA conditions used in this study were as follows: electric fields strength: 1800 V/cm, pulse width: 100  $\mu$ s, pulse interval: 2 ms. A total of 90 pulses were divided into 9 times of 10 each to avoid the thermal damage of intensive electrical current (Table 6.1). A digital oscilloscope (TDA3044B, Tektronix, US) was utilized to measure the electric current and a hole-type current probe (TCP305A, Tektronix) was clamped to a cord connecting the pulse generator and the electrodes. The conductivity of the beagle prostate was also measured before, during, and after HF-PFA treatment using 4192A LF Impedance Analyzer (Yokogawa-Hewlett-Packard Ltd.).

After the treatments, the abdomen was irrigated with 0.9% saline solution, and the incision abdomen wall was closed and sutured. All dogs were under appropriate human care from professional staff. The appetite, body temperature, fecal output, pain, and other clinical symptoms were supervised for 7 days. Antibiotic (Gentamicin, 80 mg/2 mL; SHIN POONG PHARM Ltd., Seoul, Korea) and analgesics (Keromin, 30 mg; Ketorolac; HANA PHARM Ltd., Seoul, Korea) were routinely used for three days after the surgical procedures.

### **6.3.5 Electrocardiography (ECG)**

ECG signals were monitored by the Ag/AgCl electrodes (2223H, 3M, MN, USA) connected with an ECG amplifier (PSL-iECG, PhysioLab, Busan, Korea). The fur above the lower third of the humerus and femur was performed shaved off and the sole, skin was attached with biomedical sensor pads. The signals were measured to investigate the cardiac

safety of HF-PFA on the beagle prostate. ECG including heart rate was continuously monitored and recorded before, during, and after the HF-PFA procedure about 5 minutes.

### **6.3.6 Blood chemistry**

Blood serum samples were obtained pre-, post-treatment, and 1, 7 days after HF-PFA procedure to measure cardiac troponin I levels, creatine kinase-MB (CK-MB) fraction levels, and creatine kinase (CK) levels to monitor cardiac function and inflammatory response. On days of blood sampling procedures, animals were moved to the laboratory area and a syringe with 24 gauge was inserted into the venous blood from a forelimb, and 3 ml baseline blood samples were collected and were transferred into Vacutainer SST Tubes. Tubes were pre-chilled and the specimens were centrifuged at 3500 rpm at 4 °C for 10 min. The serums were transferred to polypropylene tubes and stored at -20 °C.

### **6.3.7 Gross and histological examination**

Gross and histological examinations were performed to evaluate the gross and histopathological changes of the prostate, urinary bladder, and urethra structures of the beagle prostates after HF-PFA over time. The prostate tissues were separated from the bladder and urethra. The tissue specimens were excised and fixed in 10% formalin for at least 24 hours. The proximal, middle and distal portions of the HF-PFA ablated segments were transversely sectioned. Subsequently, the samples were processed by embedding them into paraffin blocks for gross and microscopic analysis. The slides were prepared by

microtome and stained with Masson's trichrome (MT), hematoxylin and eosin (H&E) for histomorphological analysis. Digitalized slides were assessed histologically from a scan equipment (Pannoramic 250 FLASH III, 3D HISTECH Ltd, Budapest, Hungary) and were analyzed using its viewer software (CaseViewer, 3D HISTECH Ltd).

### **6.3.8 Immunohistochemistry**

Immunohistochemistry (IHC) was performed on the paraffin-embedded sections to verify apoptotic cell death after the HF-PFA treatment. Terminal deoxynucleotidyl transferase dUTP nick end labeling (TUNEL assay) was carried on using an In-Situ Cell Death Detection, POD kit (Roche, Germany). The sections were visualized using a stainer (BenchMark XT, Ventana Medical Systems, Tucson, AZ).

Regeneration by cell proliferation was assessed by performing immunofluorescence (IF) staining of Ki-67. Briefly, all samples (G1 ~ G4) were fixed in 10 % formalin after taking off the animals at room temperature overnight. Afterward, all tissues sliced to a thickness of 3  $\mu\text{m}$  were hydrated with ethyl alcohol and washed with tap water at room temperature. The slides were incubated in 3 %  $\text{H}_2\text{O}_2$  for 10 min to block endogenous peroxidase activity, 10 % normal serum albumin for 30 min to block non-specific immunoglobulin binding, and primary antibody in PBS for 60 min. After washing the slides in PBS with 0.5 % Tween for 5 min, the slides were incubated with Alexa Fluor 594-conjugated Ki67 antibody (1:200, Rabbit, Abcam) for 60 min and the nuclei of the cells were stained with DAPI for 1 min at room temperature. Using a fluorescence microscope (magnification, X100), Ki-67 positive tissues were taken.

### **6.3.9 Statistical analysis**

Experimental results were represented as the form of mean  $\pm$  standard deviation (SD). In case of 2 levels, a two-tailed paired Student's *t*-test was performed to determine the significant differences in means (\* $P < 0.05$ ; \*\* $P < 0.01$ ; \*\*\* $P < 0.001$ ). The analysis was carried on using Excel software (2013, Microsoft Co., Ltd., Redmond, WA, USA). In case of more than 2 levels, analysis of variance (ANOVA, one-way) was conducted to decide the significant differences in means. Fisher's least significant difference test (LSD,  $P < 0.05$ ) was utilized to compare the means of the variables using RStudio Version 1.4.1106 software.

## **6.4 Results**

### **6.4.1 Simulation of electric field and temperature distribution**

For the simulation of the electric field and temperature distribution, the geometry of monopolar electrodes inserted into the prostate tissue was formed in the COMSOL Multiphysics 5.6 (Figure 6.2A). Meshed geometry was established with proper size in the analysis domain (Figure 6.2B).

Simulation of the electric field when applied 1800 V between the electrodes showed oval type electric field between the electrodes at the cross-sectional images (Figure

6.2C), and dumbbell type electric field between electrodes at the longitudinal images (Figure 6.2D). Simulation of the thermal distribution when applied 1800 V, 10 pulses between the electrodes showed that temperature slightly increased at the periphery of the electrodes (Figure 6.3A-B). The maximum temperature at the midpoint of electrodes was 37.4 °C when 1800 V was applied (Figure 6.3C).

#### **6.4.2 Electrical changes and electrocardiogram (ECG)**

The current graph showed that HF-PFA pulses were successfully delivered to the prostate tissues (Figure 6.4A) Maximum current at the 9<sup>th</sup> group increased about 3 A compared to the initial current. The electrical conductivity of prostate tissue was 3.76 folded after HF-PFA (Figure 6.4B). The total treatment time was  $420 \pm 190$  seconds. ECG of the beagles was not interfered with after HF-PFA (Figure 6.4C).

#### **6.4.3 Gross and histological examination**

Gross examination of the beagle prostate tissue after HF-PFA showed that the gross ablation areas were maximized at 4 hours and decreased over time (Figure 6.5A-B). Similar results were shown in the proximal, middle, and distal cross-sections of the prostate. Therefore, the middle sections were used to investigate further histological examinations. Histomorphological analyses including H&E, MT, and TUNEL assay were performed to investigate the histological changes in detail (Figure 6.6). The ablated areas were maximized at 4 hours and reduced over time resulting in complete tissue regeneration at 4

weeks after HF-PFA (Figure 6.7A-B).

#### **6.4.4 Detailed histological changes**

A detailed comparison between non-treated and treated areas 4 hours after HF-PFA showed that apoptotic cell death in the treated area and prostatic duct structure was preserved (Figure 6.8). The preservation of urethra tissue was observed 4 hours after HF-PFA (Figure 6.9). Magnified images showed apoptotic cell death of endothelial cells sparing the structure. The prostatic gland and ducts were preserved at the periphery of the punctured site with the electrodes 4 hours after HF-PFA (Figure 6.10).

#### **6.4.5 Immunohistochemistry**

Ki-67 was used to detect the proliferating cells in the prostate tissue over time. There were significant changes around the urethra after HF-PFA over time (Figure 6.11). There was almost no detection around the urethra 4 hours after HF-PFA indicating that urothelium cells were ablated by HF-PFA treatment. Ki-67 detection around the urethra was maximized 7 days after HF-PFA indicating that urothelium cells were undergoing proliferation. Ki-67 almost disappeared 4 weeks after HF-PFA similar to sham control. It presents that the urothelium cells around the urethra were regenerated over time.

In addition, there were significant changes in the prostatic glands after HF-PFA over time (Figure 6.12). Distances between prostatic glands were widened with decreased Ki-67 detection around the glands 4 hours after HF-PFA and the shapes of the glands were

distorted and shrunk 7 days after HF-PFA. However, the prostatic glands were almost recovered 4 weeks after HF-PFA similar to sham control. It presents that the prostatic glands were regenerated over time.

#### **6.4.6 Fibrotic changes**

Gross MT staining showed that the fibrotic areas increased and maximized 4 hours after HF-PFA, especially, around the urethra (Figure 6.13). Subsequently, the areas decreased over time similar to that of sham control. Magnified images in MT staining showed detailed changes in fibrotic areas (Figure 6.14). The extent of fibrotic changes (blue color density) around the urethra was maximized 7 days after HF-PFA. Subsequently, the extent of collagen fiber formation decreased 4 weeks after HF-PFA similar to sham control. The fibrosis around the treated area was maximized 4 hours after HF-PFA (Figure 6.15). The extent of collagen fiber formation decreased over time and was similar to sham control 4 weeks after HF-PFA.

#### **6.4.7 Biochemistry for cardiac safety**

Biochemistry of the beagles after HF-PFA over time showed that cardiac troponin I, creatine kinase MB levels were maintained during and after HF-PFA (Figure 6.16). The results showed that there were little cardiac damages after HF-PFA on the beagle prostate.



## 6.5 Discussion

PFA has many advantages to treat the LAPRC sparing the ECM, such as the neurovascular bundles, ducts, and major vasculatures in the target tissues resulting in rapid regeneration of the tissues [142]. Moreover, arrhythmias are less likely to occur because the prostate is located far from the heart [143]. Although previous studies of the PFA, no studies were using HF-PFA on the beagle prostate to ablate the LAPRC except one study that performed short period observation [144]. In the previous study, the prostatic glands were swollen 18 hours after HF-PFA but no information is existent about the histological changes and regeneration thereafter. Moreover, the applied voltage was 700 V, not enough to ablate sufficient volume of the tissues.

In this study, HF-PFA of 1800 V were delivered in 10 pulses of 9 groups, a total of 90 pulses using monopolar electrodes (Figure 6.1A-B) according to the electrical condition of the previous study [64]. Monopolar electrodes were inserted under ultrasound guidance and maintained their parallel direction (Figure 6.1E-G). The animals were sacrificed 4 hours, 7 days, and 4 weeks after HF-PFA to investigate the histomorphological changes at the prostate tissues.

It was confirmed that HF-PFA sufficiently ablated the prostate tissues through the current increases and the change of electrical conductivity (Figure 6.4A-B). In the previous study, the electrical conductivity of the prostate tissue was 3.26 folded after PFA from 0.284 to 0.927 S/m and the treated areas were sufficiently ablated [64]. The electrical conductivity of the prostate tissue was 3.76 folded after HF-PFA from 0.607 to 2.282 S/m

in this study (Figure 6.4B). It presents that the energy level of HF-PFA was enough to induce cell death of the prostate tissues.

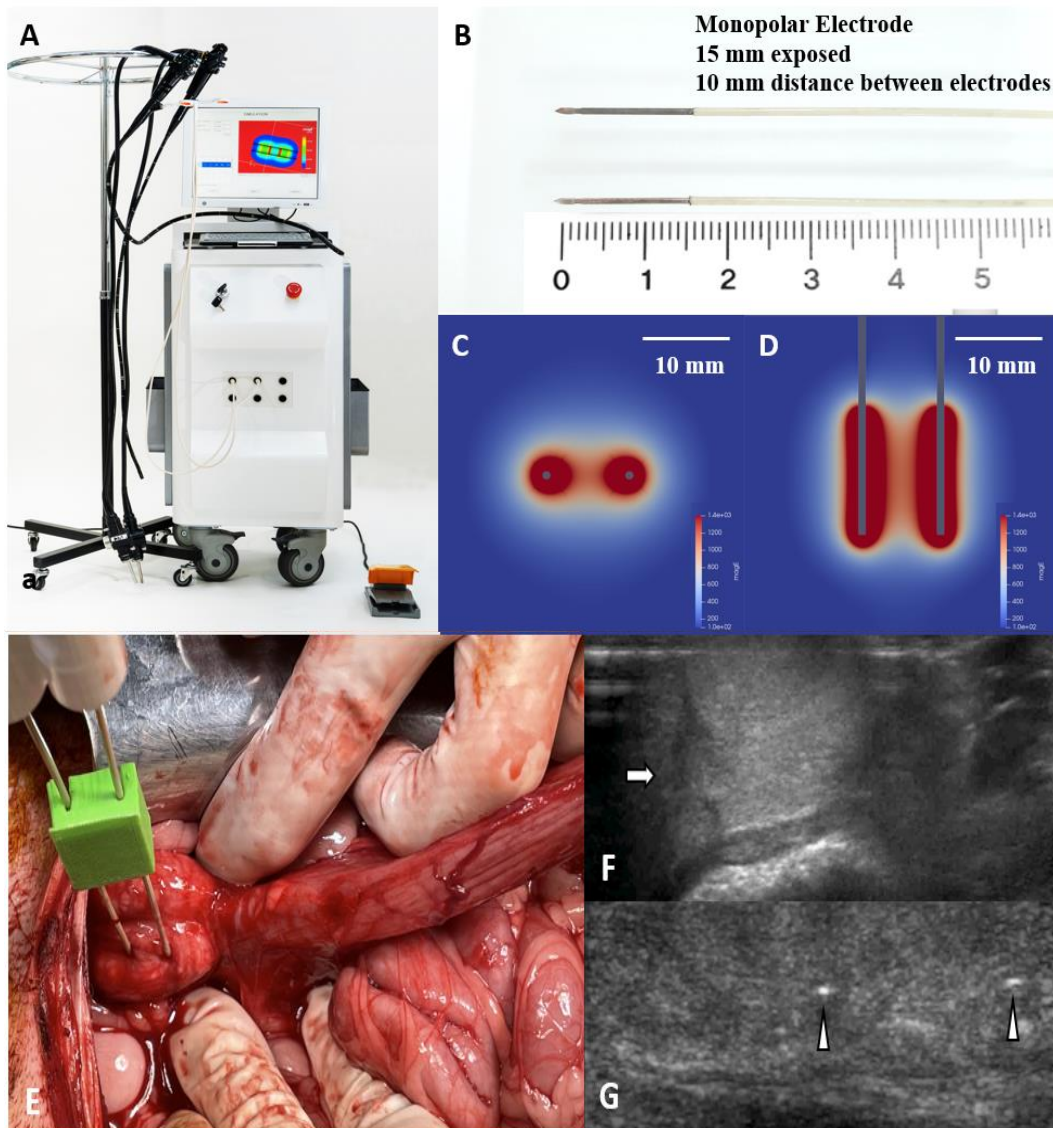
Cardiac safety issues after HF-PFA was investigated through ECG and biochemistry of cardiac marker; Troponin I, and creatine kinase MB. Troponin I levels of the beagles were maintained below 0.2 ng/mL according to the previous study [145]. ECG was distorted during the HF-PFA but restored its original shapes and frequencies instantly (Figure 6.4C). Troponin I levels after HF-PFA maintained below 0.2 ng/mL and did not increase over time (Figure 6.16A). Creatine kinase MB showed no significant increases after HF-PFA over time (Figure 6.16B). Overall, the cardiac safety of HF-PFA was verified in the beagle prostate.

Apoptotic cell death of HF-PFA was investigated by TUNEL assay and H&E to observe the gross structures in the treated areas. Gross observation showed that macroscopic changes around needle electrodes were maximized 4 hours after HF-PFA and decreased over time (Figure 6.5B). This tendency is identified also in the TUNEL assay and H&E observation (Figure 6.7A-B). In the treated areas, there were many TUNEL positive cells indicating that apoptotic cell death occurred while maintaining the urethra, vessels, ducts, and gland structures (Figure 6.8-10). This showed there was little necrosis due to the tissue structures can be disrupted in the process of necrosis [146].

Regeneration of the prostate tissue at the treated sites was investigated by immunohistochemistry of Ki-67 and MT staining. The urothelium cells around the urethra were in the process of apoptosis 4 hours after HF-PFA (Figure 6.9). Newly proliferating urothelium cells were detected 7 days after HF-PFA and recovered their original structures

in 4 weeks (Figure 6.11). This means that urothelium cells were regenerated and urethra structures were recovered in 4 weeks after HF-PFA. Prostatic gland structures were maintained but fibrotic parts increased interstitial glands 4 hours after HF-PFA (Figure 6.12, 15). The newly proliferating cells gradually increased along the border of the glands over time (Figure 6.12). The glands' structures were almost recovered their original shapes and fibrotic areas were reduced between glands 4 weeks after HF-PFA (Figure 6.15). The prostatic glands were regenerated 4 weeks after HF-PFA similar to sham control. Fibrotic areas were maximized 4 hours after HF-PFA, especially around the urethra, but decreased over time (Figure 6.13-15). Fibrotic areas also recovered 4 weeks after HF-PFA similar to the control.

The study had several limitations, including the use of one condition 1800 V/cm, thus below 1800 V/cm conditions should be investigated for further applications. Moreover, there is no data for the regeneration above 4 weeks. In conclusion, HF-PFA of 1800 V/cm successfully decellularized the beagle prostate 4 hours after the treatments. Acellular parts, such as the urethra, prostatic glands, ducts, vessels were preserved and the treated areas were regenerated in 4 weeks. These results showed that HF-PFA might be a good option to treat LAPRC.

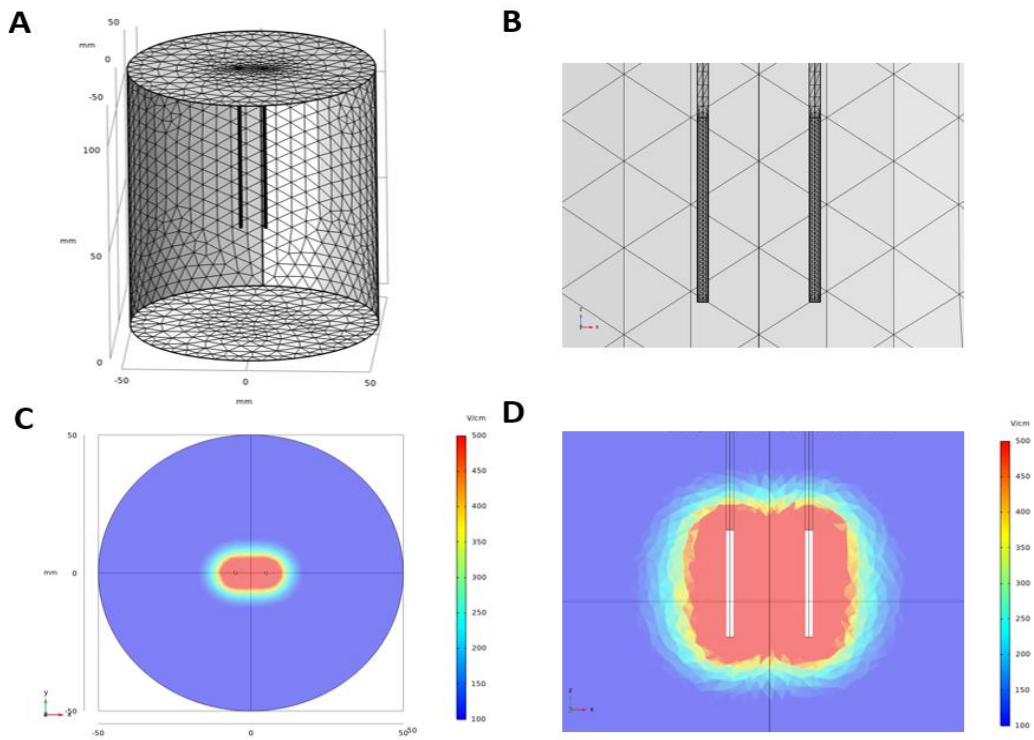


**Figure 6.1. Schematic of the HF-PFA treatment to the beagle prostate tissue.**

(A) HF-PFA generator (EPO-IRE<sup>®</sup> System, The Standard Co., Ltd., Republic of Korea) (B) Monopolar electrodes with 15 mm exposed stainless steel and 10 mm distance between electrodes (EPO probe, The Standard Co., Ltd.) (C) cross-section simulation from Openfoam software (The Standard Co., Ltd.). (D) longitudinal section simulation (E) Placement of needles prior to HF-PFA procedure in prostate tissue. (F) Identification of prostate tissue prior to the HF-PFA procedure under ultrasound guidance. The white arrow identifies the prostate. (G) Ultrasound-guided HF-PFA ablation of prostate tissue. The white arrowheads identified the needle electrode.

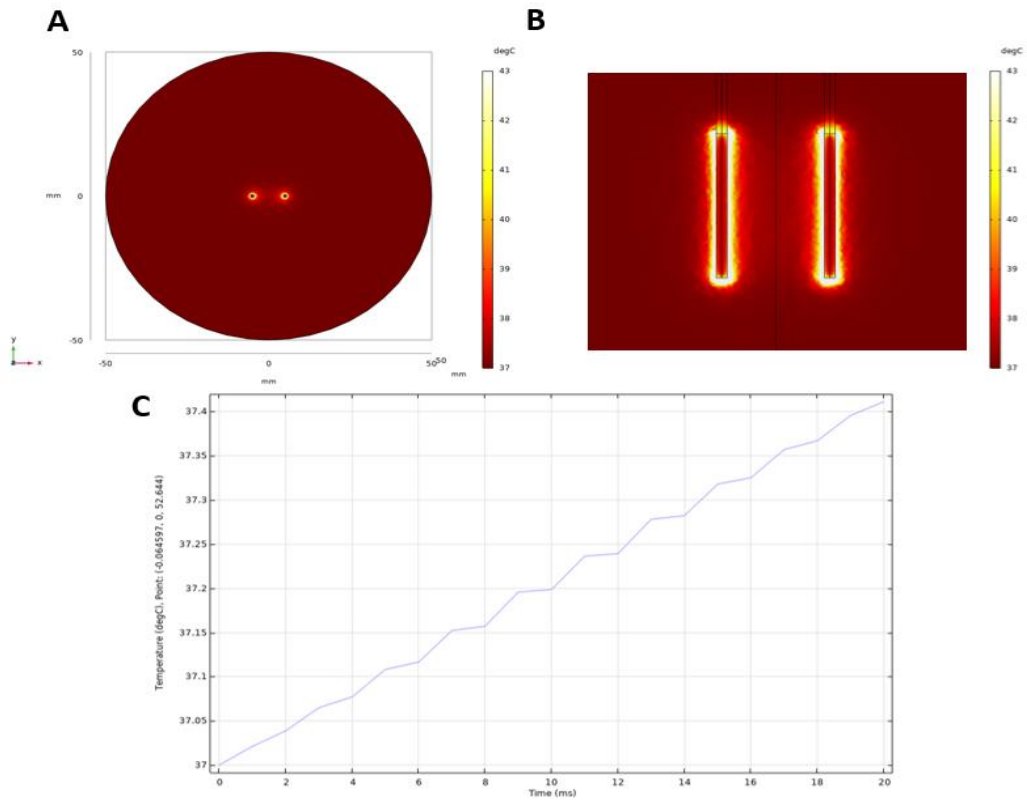
**Table 6.1. Electrical conditions of HF-PFA to ablate the beagle prostate tissue.**

	<b>Control</b>	<b>Group 1 (4 hours)</b>	<b>Group 2 (7 days)</b>	<b>Group 3 (4 weeks)</b>
Electric field	Only penetration	1800 V/cm		
Pulse number		90		
Pulse width		100 $\mu$ s		
Pulse interval		2 ms		
Burst (Pulse group)		10 pulses x 9 times		
Burst interval		10 s		
Electrode Distance		10 mm		
Electrode Exposure		15 mm		



**Figure 6.2. Simulation of electric field by HF-PFA at the prostate model in the COMSOL Multiphysics 5.6.**

(A) Meshed geometry of monopolar electrodes inserted into the prostate (B) Detailed meshes in the electrodes. (C) The electric field strength at the cross-section direction to the electrodes at the prostate when applied 1800 V between electrodes. (D) The electric field strength at the longitudinal direction to the electrodes.



**Figure 6.3. Simulation of electric field by HF-PFA at the prostate model in the COMSOL Multiphysics 5.6.**

(A) Thermal distribution at the cross-section direction to the electrodes at the prostate when applied 1800 V, 100  $\mu$ s width of 10 pulses between electrodes. (B) Thermal distribution at the longitudinal direction to the electrodes at the same condition. (C) Temperature changes at the midpoint between the electrodes over time.

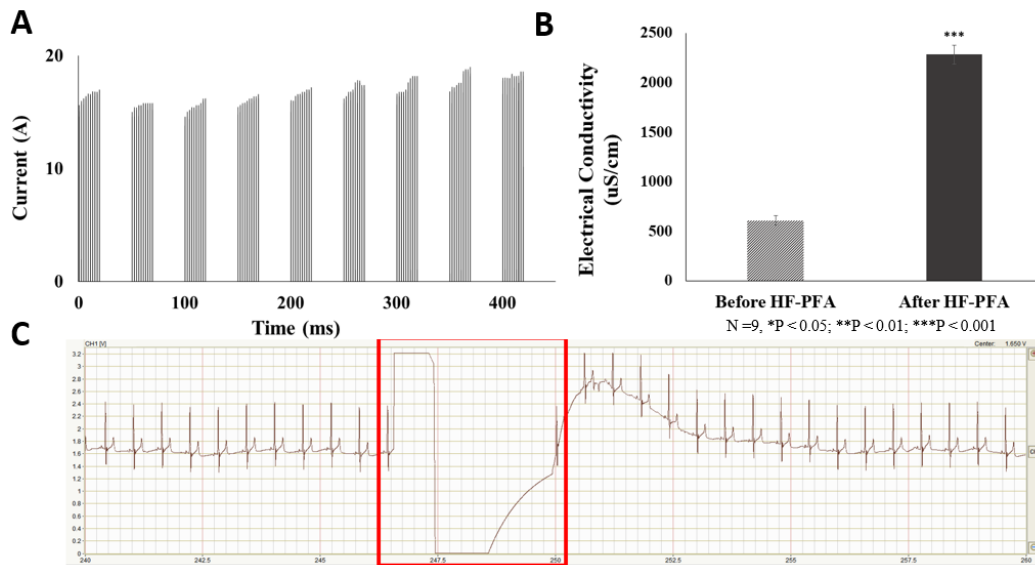
**Table 6.2. Geometrical parameters of the beagle prostate with the electrodes and physical parameters of the HF-PFA for COMSOL simulation.**

<b>Parameters</b>	<b>Value</b>
Radius of the prostate	50 [mm]
Height of the prostate	100 [mm]
Diameter of electrode	1 [mm]
Exposed length of electrode	15 [cm]
Ambient temperature	309.5 [K]
Natural convection in the air	25 [W/(m <sup>2</sup> *K)]
Applied voltage between electrodes	1800 [V/cm]
Pulse width	100 [us]
Pulse interval	2 [ms]
Pulse number	10



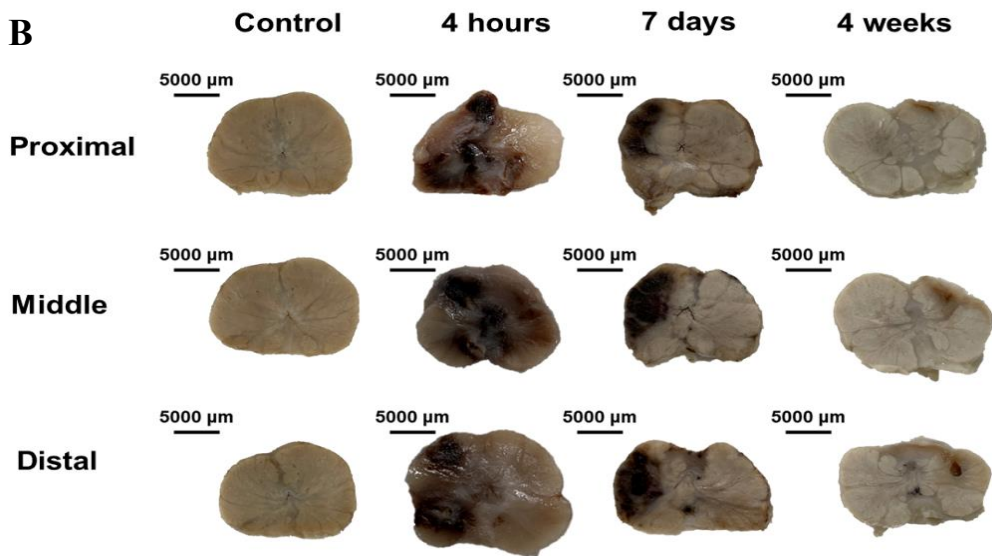
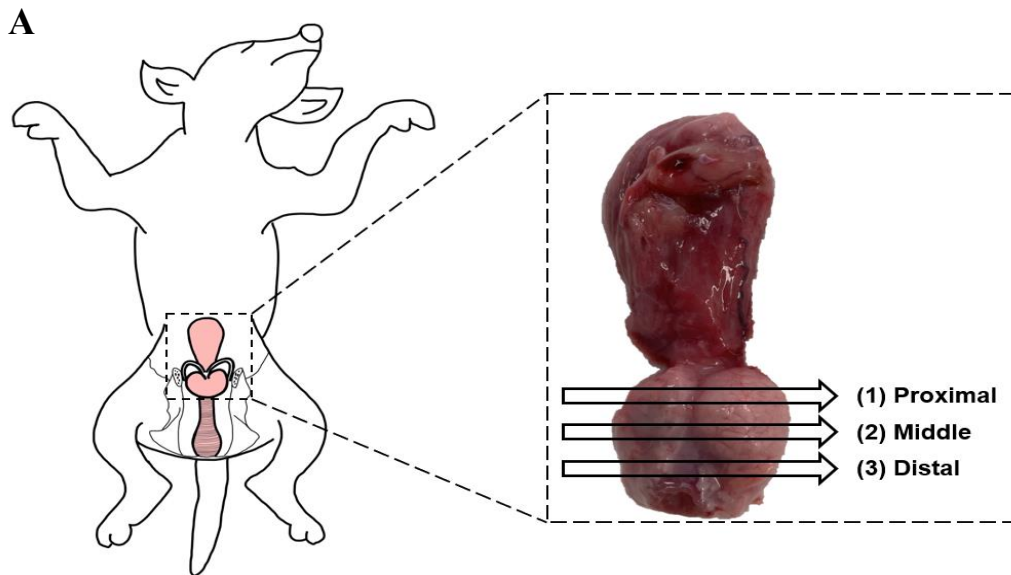
**Table 6.3. Material properties of the beagle prostate for COMSOL simulation.**

<b>Parameters</b>	<b>Value</b>
Electrical conductivity	0.13 [S/m]
Density	1045 [kg/m <sup>3</sup> ]
Heat capacity	3760 [J/(kg*K)]
Thermal conductivity	0.51 [W/(m*K)]
Relative permittivity	53



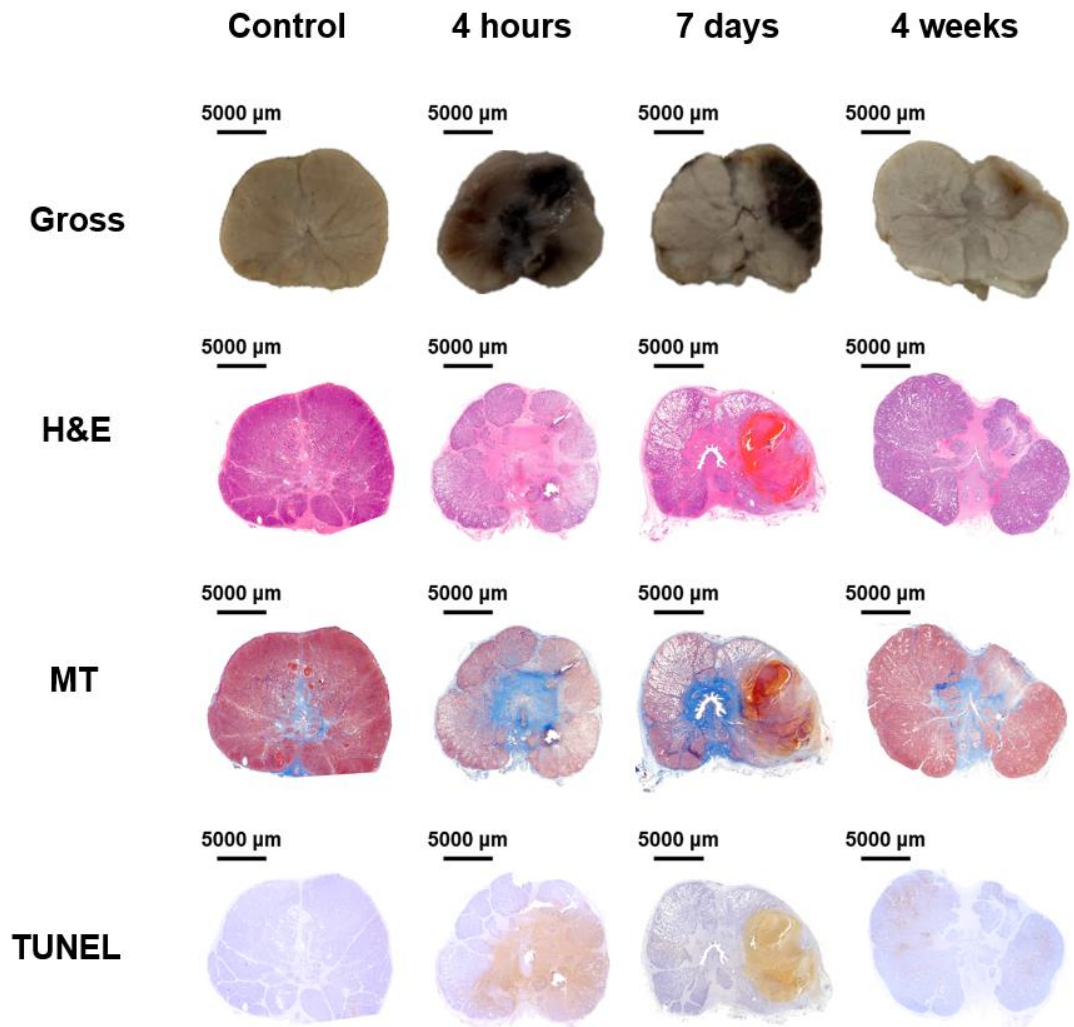
**Figure 6.4. Current, electrical conductivity changes of the prostate and ECG of the beagles after HF-PFA.**

(A) Current graph of 10 pulses of 9 groups (Interval times between group pulses were omitted due to comparably long time; about 10 s). (B) The electrical conductivity of prostate tissue was 3.76 folded after HF-PFA. Treatment time was  $420 \pm 190$  seconds. N = 9, \*P < 0.05; \*\*P < 0.01; \*\*\*P < 0.001. (C) ECG of the beagle after HF-PFA (71<sup>th</sup>-80<sup>th</sup> pulsing, Red box).



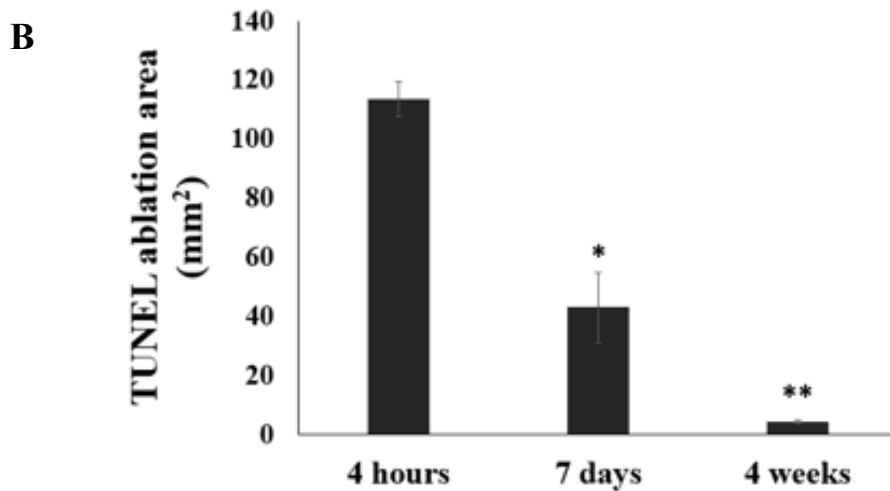
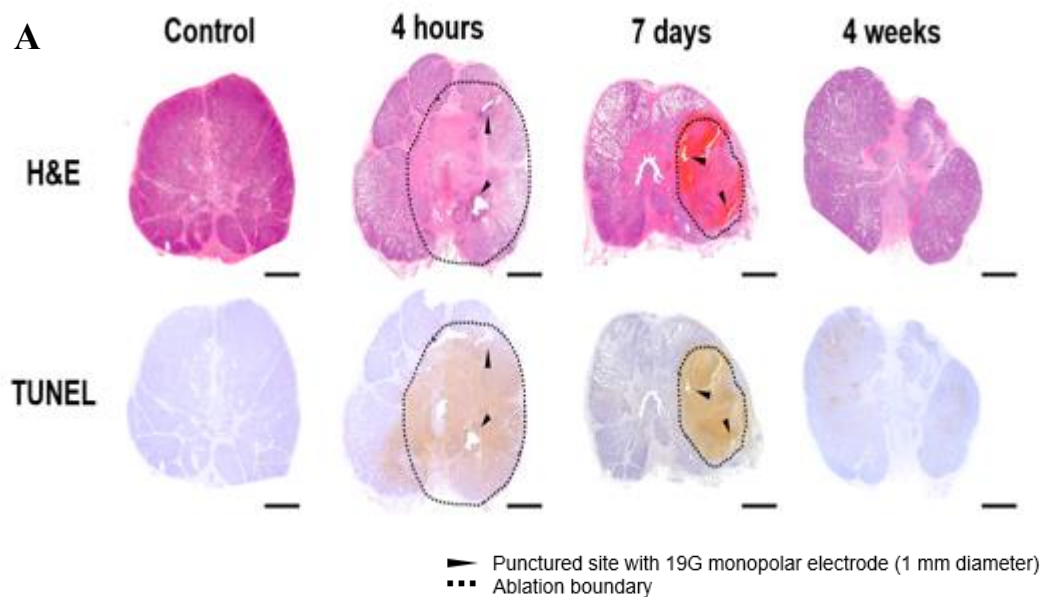
**Figure 6.5. Location of tissue samples and gross changes of the prostate after HF-PFA over time.**

(A) Prostate tissue samples showing the proximal (1), middle (2), and distal (3) location ablated by HF-PFA. (B) Representative photomicrographs of gross prostate tissue at different time points.



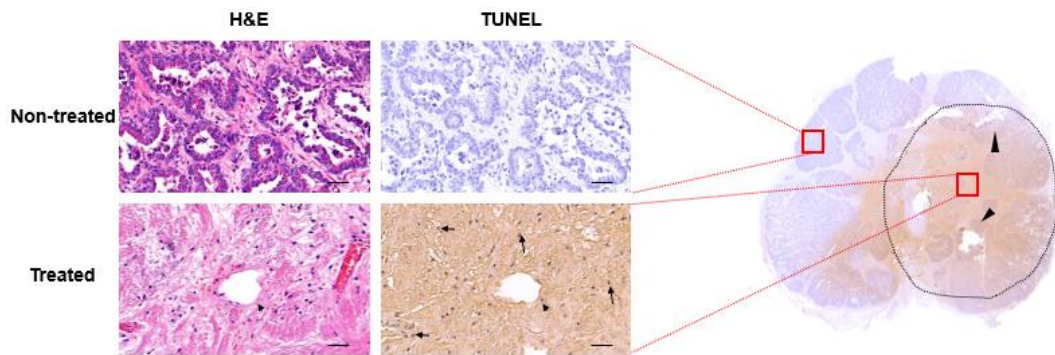
**Figure 6.6. Gross and histological findings of the prostate after HF-PFA over time.**

Representative photomicrographs of gross, H&E, MT histomorphological analysis, and TUNEL assay of prostate tissue specimens from the dogs (magnification, x2).



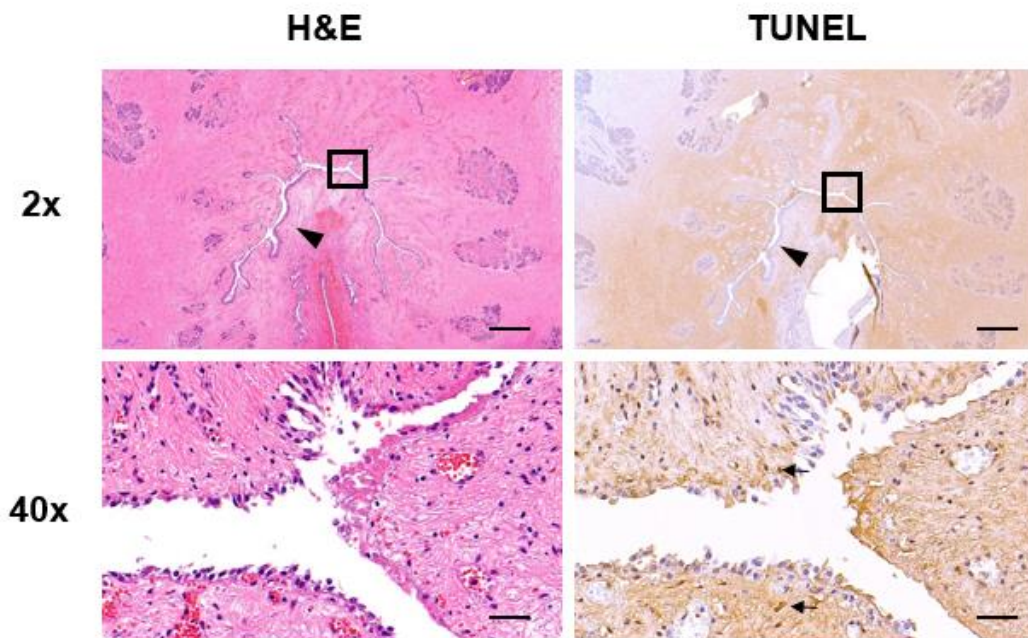
**Figure 6.7. Changes in TUNEL stained areas after HF-PFA over time**

(A) Histological changes of the beagle prostate after HF-PFA. Scale bar, 5 mm; magnification, x0.2. (B) Histogram of TUNEL stained area after HF-PFA. N=3, \*P < 0.05; \*\*P < 0.01; \*\*\*P < 0.001.



**Figure 6.8. Detailed comparison of histological findings to compare ablation area.**

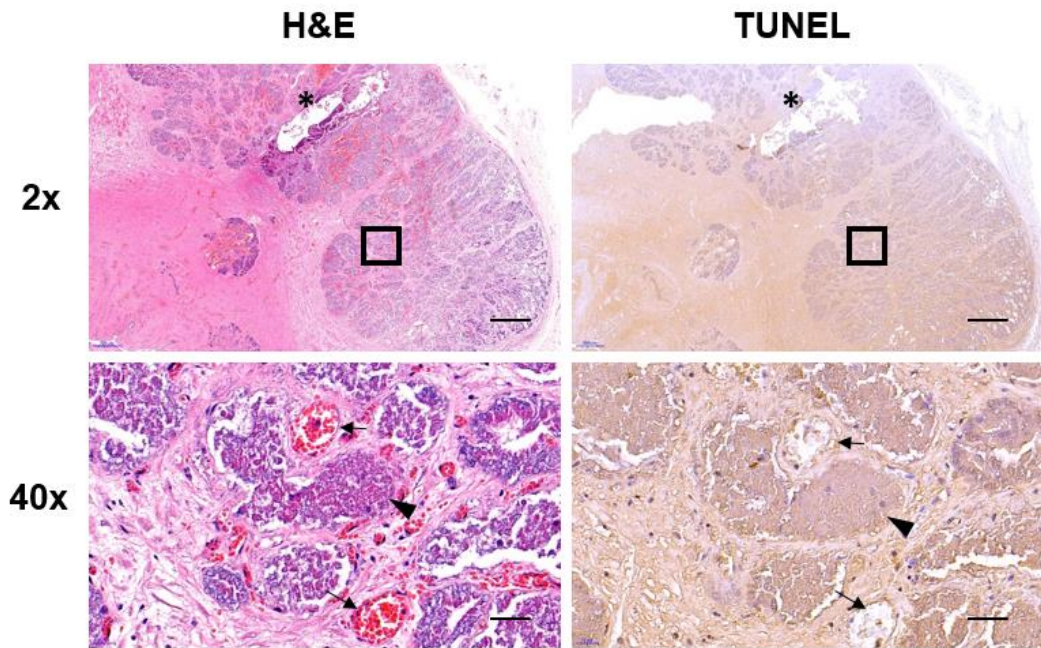
TUNEL result 4 hours after HF-PFA showed apoptotic cell death in the treated area (Arrow). Prostatic duct structure was preserved (Arrowhead). Scale bar, 50  $\mu\text{m}$ ; magnification, x0.2.



**Figure 6.9. Preservation of urethra tissue after HF-PFA.**

H&E, TUNEL result 4 hours after HF-PFA showed the preservation of urethra tissue (Arrowhead). Scale bar, 1 mm; magnification, x2. Magnified images showed apoptotic cell death of endothelial cells sparing the structure (Arrows). Images achieved from inbox in the 2x images. Scale bar, 50  $\mu$ m; magnification, x40.

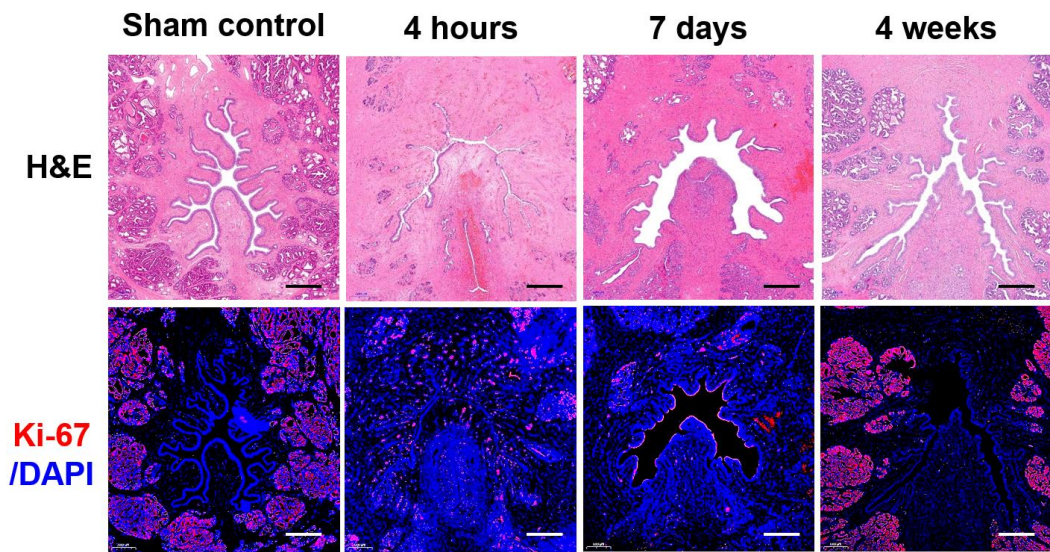




**Figure 6.10. Preservation of prostatic gland and vessels after HF-PFA.**

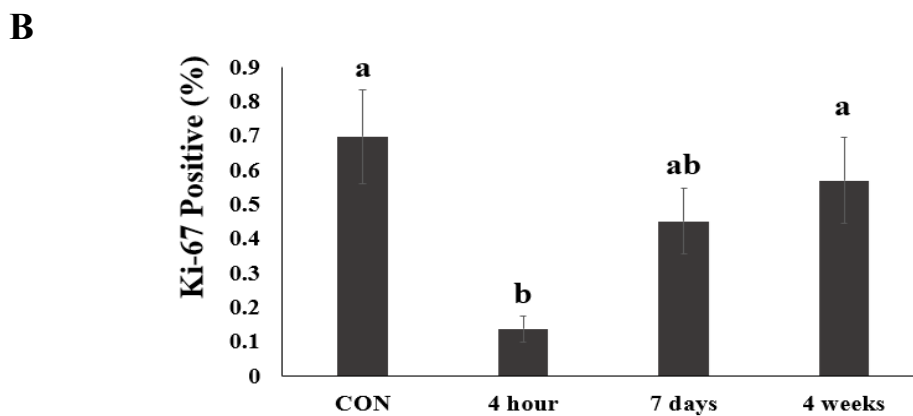
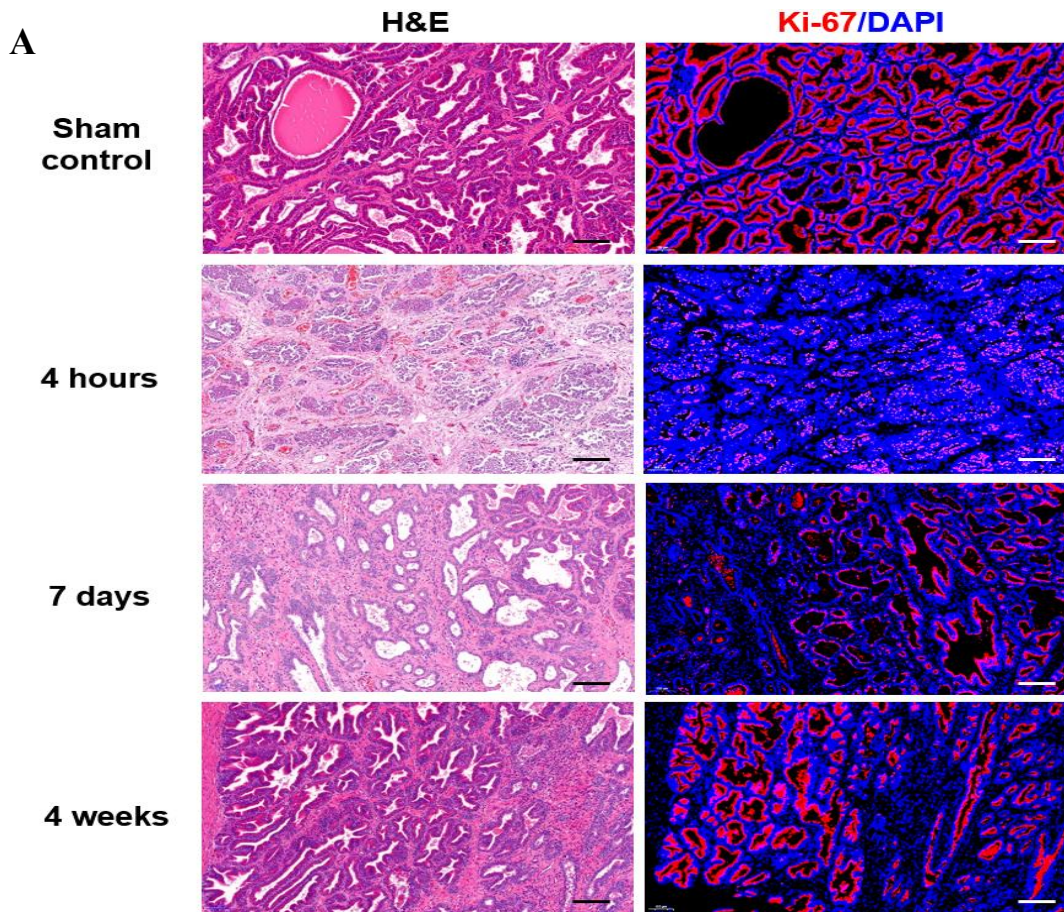
H&E, TUNEL histological analysis 4 hours after HF-PFA showed the prostatic gland and duct were preserved at the periphery of the punctured site with the electrodes (asterisk). Scale bar, 1 mm; magnification, x2. Magnified images showed prostatic gland (arrowheads) and vessels (arrows) were preserved. Images achieved from inbox in the 2x images. Scale bar, 50  $\mu$ m; magnification, x40.





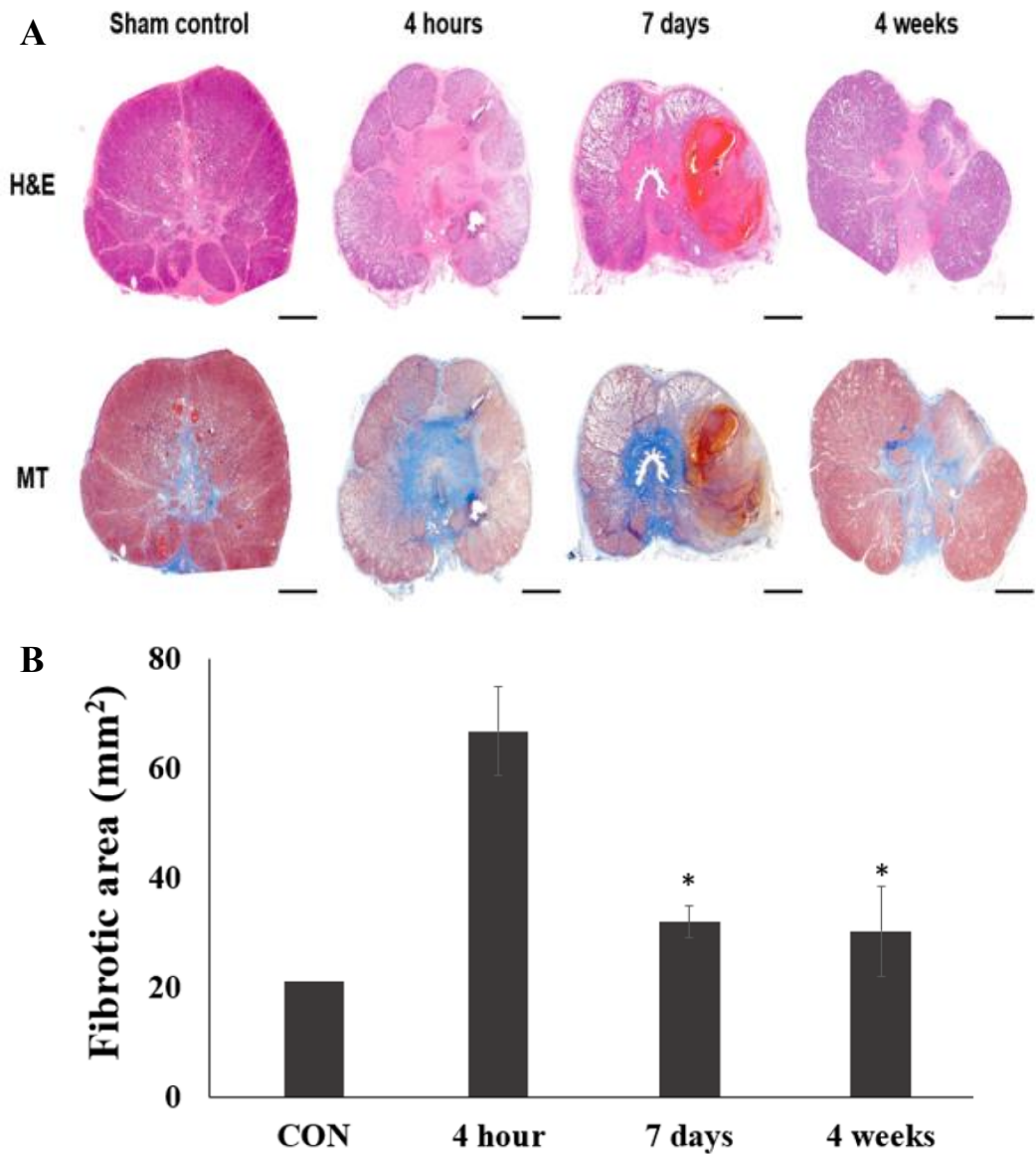
**Figure 6.11. Regeneration of the urothelium cells after HF-PFA.**

H&E, IHC of Ki-67 histological analysis 4 hours, 7 days, and 4 weeks after HF-PFA compared to sham control showed the urothelium cells were regenerated over time. Scale bar, 1 mm; magnification, x2.



**Figure 6.12. Regeneration of the prostatic gland after HF-PFA.**

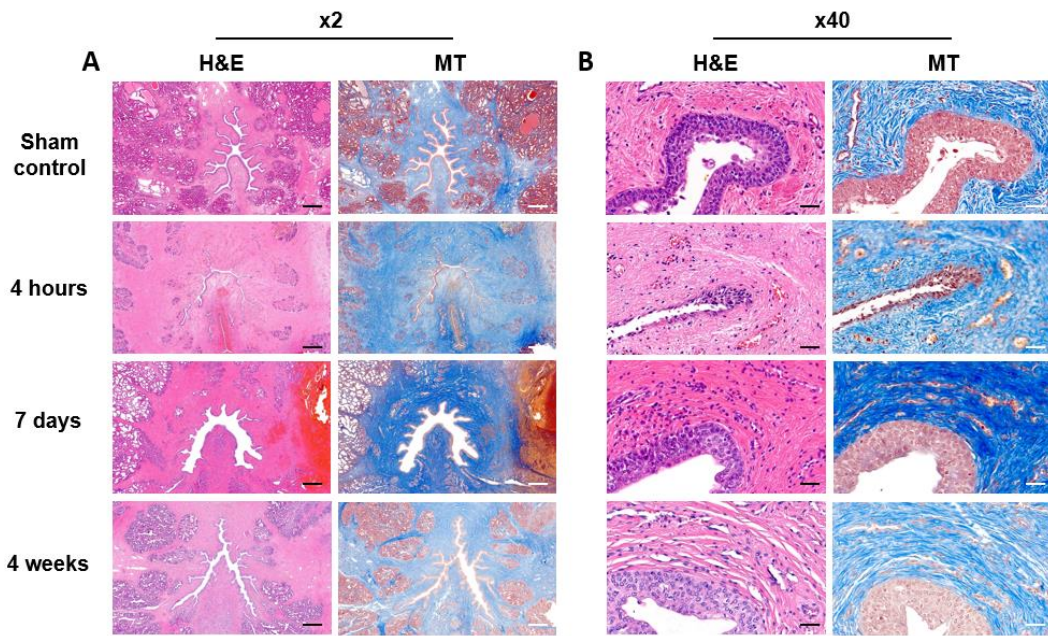
(A) Regeneration of the beagle prostatic gland after HF-PFA. Scale bar, 0.2 mm; magnification, x10. (B) Histogram of Ki-67 positive areas after HF-PFA. N=3, \*P<0.05; \*\*P<0.01; \*\*\*P<0.001.



**Figure 6.13. Changes in the fibrotic area after HF-PFA over time.**

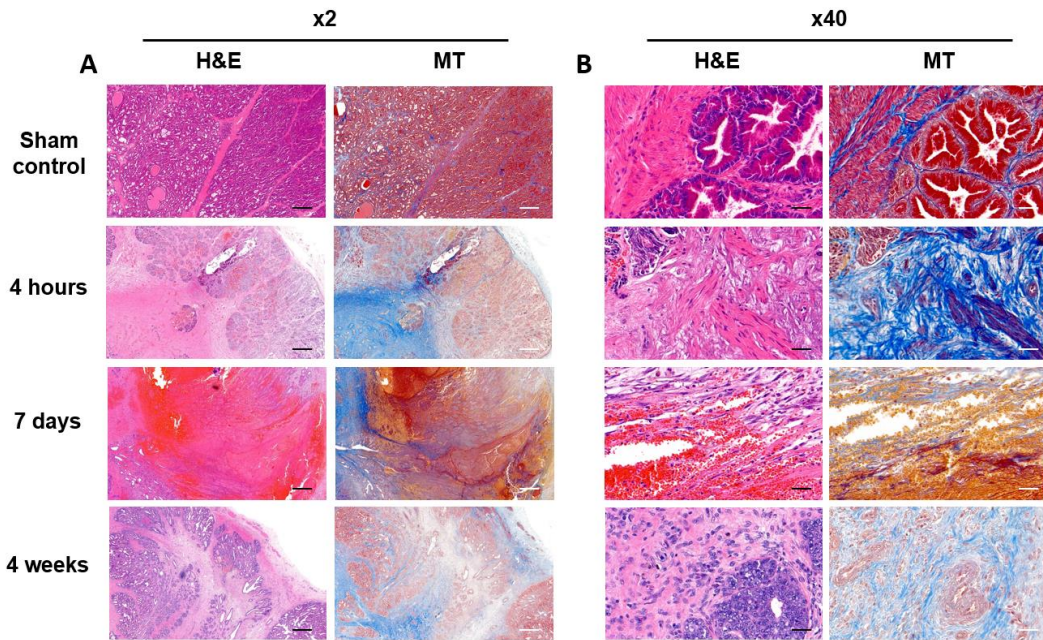
(A) Histological changes of the beagle prostate after HF-PFA. Scale bar, 5 mm; magnification, x0.2. (B) Histogram of fibrotic area after HF-PFA. N=3, \*P < 0.05; \*\*P < 0.01; \*\*\*P < 0.001.





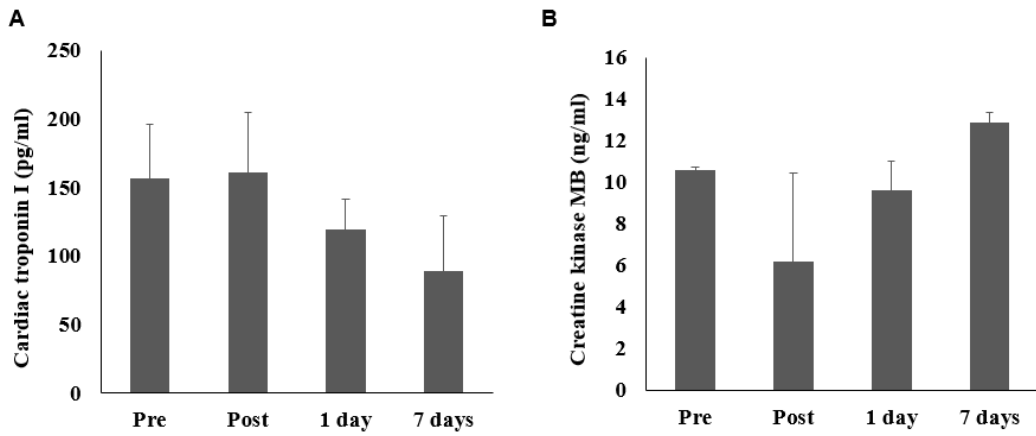
**Figure 6.14. Fibrotic areas around the urethra after HF-PFA over time.**

**(A)** Fibrotic areas around the urethra. Scale bar, 5 mm; magnification, x2. **(B)** Magnified images. Scale bar, 250  $\mu$ m; magnification, x40.



**Figure 6.15. Fibrotic areas around the HF-PFA treated area over time.**

**(A)** Fibrotic areas around the HF-PFA treated area. Scale bar, 5 mm; magnification, x2. **(B)** Magnified images. Scale bar, 250  $\mu$ m; magnification, x40.



**Figure 6.16. Biochemistry of the beagles after HF-PFA over time.**

(A) Cardiac troponin I levels (B) Creatine kinase MB levels in beagle serum. N=2, \*P < 0.05; \*\*P < 0.01; \*\*\*P < 0.001

## Chapter 7. Conclusions

In this dissertation, high-voltage high-frequency pulsed field ablation (HF-PFA) was developed to ablate the locally advanced solid tumor (LAST). First, a novel evaluation method was developed to evaluate electroporated areas caused by HF-PFA on the potato model. It takes about 12 hours to evaluate the HF-PFA ablated areas using a common method of polyphenol oxidation. Using our 2,3,5-triphenyltetrazolium chloride (TTC) method, the electroporated areas can be assessed within 3 hours and reversibly electroporated areas also can be observed, which makes it possible to predict the HF-PFA affected zone in the drug delivery or gene transfection research field. The various HF-PFA conditions such as voltage, pulse number, pulse width, pulse interval for *in-vitro*, *in-vivo* studies were indirectly performed and prescreened using the TTC method on the potato model. Second, an *in-vitro* 3D culture model of cancer cells was constructed using agarose gel to investigate the tissue scaffold and regeneration ability of HF-PFA based on a tissue engineering perspective. Decellularization was induced by HF-PFA on the gel and regeneration was induced by perfusion bioreactor with adipose-derived mesenchymal stem cells (ADMSC). Decellularization was evaluated using a live and dead cell assay kit with a fluorescence microscope and hematoxylin and eosin (H&E). Nerve regeneration was evaluated using immunocytochemistry (ICC) of Tuj1. Third, cell apoptosis of human prostate cancer tissue was studied using HF-PFA. Human prostate cancer tissues were induced on the skin of the nude mouse and HF-PFA was performed on the cancer tissue with monopolar electrodes. The cell apoptosis markers, cleaved caspase-3, and BCL-2 were upregulated after HF-PFA with the weight of cancer tissue decreasing over time. HF-PFA had an effect to induce cell apoptosis and reduce the mass of cancer tissue. Finally,

the decellularization and tissue regeneration process after HF-PFA were investigated in the *in-vivo* experiment using prostate tissue of canine. Cell apoptosis and decellularization process was maximized 4 hours after HF-PFA and the recellularization was observed 7 days after HF-PFA. The prostate tissue was almost regenerated with minor fibrosis at 4 weeks.

In the results, HF-PFA successfully fabricated decellularized tissue scaffold to ablate LAST with cell apoptosis and provided the environments for rapid and proper tissue regeneration. Therefore, HF-PFA can be utilized in the field of tissue engineering and regenerative medicine and promotes the rapid and accurate ablation of LAST in clinical surgery to enhance the quality of life.



## Abstract (Korean)

펄스 전기장 절제(PFA)는 국소 진행성 고형암을 치료하기 위한 국소 조직 절제 방법으로, 마이크로초의 짧은 고전압 전기 펄스를 사용하여 세포막을 비가역적으로 천공하여 세포의 비가역적인 사멸을 초래한다. 고주파 절제(RFA), 마이크로파, 고강도 집적 초음파(HIFU) 및 초저온 절제와 같은 열을 초래하는 절제법과 달리 PFA 는 열 발생이 최소화된 비열적 절제법으로 오직 세포만을 사멸하고, 세포외기질(ECM), 혈관, 신경 및 도관과 같은 비세포성 조직은 보존하여 빠른 조직 재생 및 조직 기능의 보존을 가능하게 한다. 따라서 PFA 는 국소 진행성 췌장암(LAPC), 국소 진행성 전립선암(LAPRC) 및 간세포 암종(HCC)과 같은 국소 진행성 고형 종양(LAST)에 대한 다른 열적 국소 절제 방식의 대안으로 또는 항암 화학 요법의 보조 요법으로 제시된다. 대부분의 연구는 저주파 펄스 펄드 절제(LF-PFA)를 사용한 임상 및 전임상 시험에 집중되었다. 그러나, 고주파 펄스 펄드 절제(HF-PFA)를 사용하여 조직의 탈세포 및 조직 재생을 조사하기 위해 조직 공학 관점에서 접근한 연구는 전무하다.

본 논문에서는 감자 모델에서 HF-PFA 에 의해 전기천공된 영역을 평가하여 LAST 를 성공적으로 제거하기 위한 최적의 조건을 사전 선별하는 방법을 개발하였다. 또한, 체외 3D 배양 모델에서 HF-PFA 를 이용한 탈세포화된 조직 지지체를 제작하고 탈세포화된 지지체에서 인간 지방유래줄기세포 (hADMSC)의 신경 조직 분화능을 조사하였다. HF-PFA 시스템 및 전극은 (주)더스탠다드(군포시, 한국)에서 제조하였다. HF-PFA 를 사용하여 인간 전립선암 조직의 세포 사멸을 연구하였다. 마지막으로 개의 전립선 조직을 이용한 생체 내 실험에서 HF-PFA 후 탈세포화 및 조직 재생 과정을 재확인하였다. 연구의 기초가 되는 가설은 HF-PFA 가 (i) 세포 사멸로 LAST 를 제거하기 위해 탈세포화된 조직

스캐폴드를 유도할 수 있고, (ii) 신속하고 적절한 조직 재생을 위한 환경을 제공할 수 있다는 것이다.

논문 연구의 주요 결과는 다음과 같이 요약될 수 있다. 첫째, 감자 모델에서 PFA 로 인한 전기천공 영역을 평가하기 위한 새로운 평가 방법이 개발되었다. 기존 연구들에서 널리 차용된 폴리페놀 산화를 통한 멜라닌 색소 침착법을 이용하여 PFA 를 통한 탈세포 영역을 평가하는 데 약 12 시간이 걸린다. 반면, 본 연구에서 새롭게 제시한 2,3,5-triphenyltetrazolium chloride(TTC) 방법을 사용하면 탈세포 영역을 3 시간 이내에 평가할 수 있으며 가역적으로 전기천공 된 영역도 추가적으로 관찰할 수 있어 약물 전달 또는 유전자 형질감염 등 분야에서 요구되는 PFA 로 인한 가역적 전기천공 영역을 예측할 수 있다. 생체 외, 생체 내 연구를 위한 HF-PFA 의 전압, 펄스 수, 펄스 폭, 펄스 간격 조건을 감자 모델에서 TTC 방법을 사용하여 간접적으로 수행하고 사전 선별했다. 둘째, 암세포의 체외 3D 배양 모델을 아가로스 겔, 매트릭스를 사용하여 제작하고 조직 공학적 관점을 기반으로 HF-PFA 의 탈세포 지지체 유도 및 조직 재생 능력을 조사하였다. HF-PFA 에 의해 3D 하이드로겔의 탈세포화가 유도되었고 지방유래 중간엽 줄기세포(ADMSC)가 탈세포화된 지지체에 로딩되어 관류식 생물반응기로 분화배양배지를 순환하며 배양되었다. 탈세포화는 형광 현미경을 통해 live & dead cell kit 를 사용하여 평가되었다. 헤마톡실린 및 에오신(H&E) 염색, Tuj1 과 같은 신경 조직 재생 마커의 면역세포화학염색(ICC)을 사용하여 재세포화를 평가하였다. 셋째, HF-PFA 를 사용하여 인간 전립선암 조직의 세포 사멸을 연구하였다. 인간의 전립선암 조직은 누드 마우스의 피부에 유도되었고 HF-PFA 는 단극성 전극으로 암 조직에 수행되었다. 세포 사멸 마커인 절단된 caspase-3 및 BCL-2 는 HF-PFA 후에 상향 조절되었고 암 조직의 무게는 시간이 지남에 따라 감소했다. HF-PFA 는 세포 사멸을 유도하고

암 조직의 질량을 줄이는 효과가 있었다. 마지막으로, 개의 전립선 조직을 이용한 생체 내 실험에서 HF-PFA 이후의 탈세포화 및 조직 재생 과정을 조사하였다. 세포 사멸 및 탈세포화 과정은 HF-PFA 4 시간 후에 극대화되었고 재생세포화는 HF-PFA 7 일 후에 관찰되었다. 전립선 조직은 4 주에 약간의 섬유증과 함께 거의 재생되었다.

결론적으로, HF-PFA 는 세포 사멸로 LAST 를 제거하기 위해 탈세포화된 조직 지지체를 성공적으로 유도하고 신속하고 적절한 조직 재생을 위한 환경을 제공했다. 따라서 HF-PFA 는 조직공학 및 재생의학 분야에서 활용될 수 있으며 임상 수술에서 LAST 의 신속하고 정확한 절제를 촉진하여 삶의 질을 향상시킬 수 있을 것으로 보인다.

주요어: 고주파 펄스 필드 절제, 국소 진행성 고형암, 탈세포화, 조직 재생

학 번: 2013-23254

## References

- [1] J.A. Nollet, Recherches Sur Les Causes Particulieres Des Phénomènes Électriques, Et sur les effets nuisibles ou avantageux qu'on peut en attendre, Guerin & Delatour, 1764.
- [2] H. Antoni, A. Chilbert, D. Sweeney, J.P. Reilly, Applied bioelectricity: From electrical stimulation to electrophathology, JP Reilly. (1998) 12–72.
- [3] E.D. WEINBERG, G.E. WARD, Diathermy and regeneration of bone, Arch. Surg. 28 (1934) 1121–1129.
- [4] R. V Christie, C.A.L. Binger, AN EXPERIMENTAL STUDY OF DIATHERMY: IV. Evidence for the Penetration of High Frequency Currents through the Living Body., J. Exp. Med. 46 (1927) 715–734.
- [5] Gm. McKinley, B.M. Duggar, Short electric wave radiation in biology, Biol. Eff. Radiat. 1 (1936) 541–558.
- [6] R. Davalos, B. Rubinsky, Tissue ablation with irreversible electroporation, (2011).
- [7] R. V Davalos, L.M. Mir, B. Rubinsky, Tissue ablation with irreversible electroporation, Ann. Biomed. Eng. 33 (2005) 223–231.
- [8] G. Onik, P. Mikus, B. Rubinsky, Irreversible electroporation: implications for prostate ablation, Technol. Cancer Res. Treat. 6 (2007) 295–300.
- [9] J. Rubinsky, G. Onik, P. Mikus, B. Rubinsky, Optimal parameters for the

- destruction of prostate cancer using irreversible electroporation, *J. Urol.* 180 (2008) 2668–2674.
- [10] A. Ivorra, B. Rubinsky, Historical review of irreversible electroporation in medicine, in: *Irreversible Electroporation*, Springer, 2010: pp. 1–21.
- [11] R.C.G. Martin, D. Kwon, S. Chalikonda, M. Sellers, E. Kotz, C. Scoggins, K.M. McMasters, K. Watkins, Treatment of 200 locally advanced (stage III) pancreatic adenocarcinoma patients with irreversible electroporation: safety and efficacy, *Ann. Surg.* 262 (2015) 486–494.
- [12] J. Pinero, M. Lopez-Baena, T. Ortiz, F. Cortes, Apoptotic and necrotic cell death are both induced by electroporation in HL60 human promyeloid leukaemia cells, *Apoptosis.* 2 (1997) 330–336.
- [13] F. Hofmann, H. Ohnimus, C. Scheller, W. Strupp, U. Zimmermann, C. Jassoy, Electric field pulses can induce apoptosis, *J. Membr. Biol.* 169 (1999) 103–109.
- [14] T. Kotnik, D. Miklavčič, Analytical description of transmembrane voltage induced by electric fields on spheroidal cells, *Biophys. J.* 79 (2000) 670–679.
- [15] J. Gimsa, D. Wachner, Analytical description of the transmembrane voltage induced on arbitrarily oriented ellipsoidal and cylindrical cells, *Biophys. J.* 81 (2001) 1888–1896.
- [16] S. Čorović, M. Pavlin, D. Miklavčič, Analytical and numerical quantification and comparison of the local electric field in the tissue for different electrode configurations, *Biomed. Eng. Online.* 6 (2007) 37. <https://doi.org/10.1186/1475->

925X-6-37.

- [17] R. Langer, J. Vacanti, Tissue engineering, *Sci. (American Assoc. Adv. Sci.* 260 (1993) 920–926.
- [18] A. Jaklenec, A. Stamp, E. Deweerdt, A. Sherwin, R. Langer, Progress in the Tissue Engineering and Stem Cell Industry “Are we there yet?,” *Tissue Eng. Part B. Rev.* 18 (2012) 155–166.
- [19] N. Almouemen, H.M. Kelly, C. O’Leary, Tissue Engineering: Understanding the Role of Biomaterials and Biophysical Forces on Cell Functionality Through Computational and Structural Biotechnology Analytical Methods, *Comput. Struct. Biotechnol. J.* 17 (2019) 591–598.  
<https://doi.org/10.1016/j.csbj.2019.04.008>.
- [20] M. Phillips, E. Maor, B. Rubinsky, Principles of tissue engineering with nonthermal irreversible electroporation, *J. Heat Transfer.* 133 (2011) 1–8.  
<https://doi.org/10.1115/1.4002301>.
- [21] M. Phillips, E. Maor, B. Rubinsky, Nonthermal irreversible electroporation for tissue decellularization, *J. Biomech. Eng.* 132 (2010) 1–8.  
<https://doi.org/10.1115/1.4001882>.
- [22] C. Jiang, R. V Davalos, J.C. Bischof, A Review of Basic to Clinical Studies of Irreversible Electroporation Therapy, *IEEE Trans. Biomed. Eng.* 62 (2015) 4–20.  
<https://doi.org/10.1109/TBME.2014.2367543>.
- [23] I.K. Nederland, Netherlands Comprehensive Cancer Organisation, Netherlands

Cancer Regist. Age Gend. (2014).

- [24] P.J. Loehrer Sr, Y. Feng, H. Cardenes, L. Wagner, J.M. Brell, D. Cella, P. Flynn, R.K. Ramanathan, C.H. Crane, S.R. Alberts, Gemcitabine alone versus gemcitabine plus radiotherapy in patients with locally advanced pancreatic cancer: an Eastern Cooperative Oncology Group trial, *J. Clin. Oncol.* 29 (2011) 4105.
- [25] J.E. Niederhuber, M.F. Brennan, H.R. Menck, The national cancer data base report on pancreatic cancer, *Cancer.* 76 (1995) 1671–1677.
- [26] H.J. Scheffer, A.G.M. Stam, B. Geboers, L.G.P.H. Vroomen, A. Ruarus, B. de Bruijn, M.P. van den Tol, G. Kazemier, M.R. Meijerink, T.D. de Gruijl, Irreversible electroporation of locally advanced pancreatic cancer transiently alleviates immune suppression and creates a window for antitumor T cell activation, *Oncoimmunology.* 8 (2019) 1652532.
- [27] H.J. Scheffer, L.G.P.H. Vroomen, M.C. de Jong, M.C.A.M. Melenhorst, B.M. Zonderhuis, F. Daams, J.A. Vogel, M.G.H. Besselink, C. van Kuijk, J. Witvliet, Ablation of locally advanced pancreatic cancer with percutaneous irreversible electroporation: results of the phase I/II PANFIRE study, *Radiology.* 282 (2017) 585–597.
- [28] C. Niessen, L.P. Beyer, B. Pregler, M. Dollinger, B. Trabold, H.J. Schlitt, E.M. Jung, C. Stroszczyński, P. Wiggermann, Percutaneous ablation of hepatic tumors using irreversible electroporation: a prospective safety and midterm efficacy study

- in 34 patients, *J. Vasc. Interv. Radiol.* 27 (2016) 480–486.
- [29] C. Månsson, M. Bergensfeldt, R. Brahmstaedt, B.-M. Karlson, P. Nygren, A. Nilsson, Safety and preliminary efficacy of ultrasound-guided percutaneous irreversible electroporation for treatment of localized pancreatic cancer, *Anticancer Res.* 34 (2014) 289–293.
- [30] B. Geboers, H.J. Scheffer, P.M. Graybill, A.H. Ruarus, S. Nieuwenhuizen, R.S. Puijk, P.M. van den Tol, R. V Davalos, B. Rubinsky, T.D. de Gruijl, High-voltage electrical pulses in oncology: irreversible electroporation, electrochemotherapy, gene electrotransfer, electrofusion, and electroimmunotherapy, *Radiology.* 295 (2020) 254–272.
- [31] L. Vroomen, E.N. Petre, F.H. Cornelis, S.B. Solomon, G. Srimathveeravalli, Irreversible electroporation and thermal ablation of tumors in the liver, lung, kidney and bone: What are the differences?, *Diagn. Interv. Imaging.* 98 (2017) 609–617.
- [32] J.A. Vogel, E. Van Veldhuisen, P. Agnass, J. Crezee, F. Dijk, J. Verheij, T.M. Van Gulik, M.R. Meijerink, L.G. Vroomen, K.P. Van Lienden, Time-dependent impact of irreversible electroporation on pancreas, liver, blood vessels and nerves: a systematic review of experimental studies, *PLoS One.* 11 (2016) e0166987.
- [33] K.F. Chu, D.E. Dupuy, Thermal ablation of tumours: biological mechanisms and advances in therapy, *Nat. Rev. Cancer.* 14 (2014) 199–208.
- [34] B.E. Bulvik, N. Rozenblum, S. Gourevich, M. Ahmed, A. V Andriyanov, E.



- Galun, S.N. Goldberg, Irreversible electroporation versus radiofrequency ablation: a comparison of local and systemic effects in a small-animal model, *Radiology*. 280 (2016) 413–424.
- [35] S.B. White, Z. Zhang, J. Chen, V.R. Gogineni, A.C. Larson, Early immunologic response of irreversible electroporation versus cryoablation in a rodent model of pancreatic cancer, *J. Vasc. Interv. Radiol.* 29 (2018) 1764–1769.
- [36] Q. Shao, S. O’Flanagan, T. Lam, P. Roy, F. Pelaez, B.J. Burbach, S.M. Azarin, Y. Shimizu, J.C. Bischof, Engineering T cell response to cancer antigens by choice of focal therapeutic conditions, *Int. J. Hyperth.* 36 (2019) 130–138.
- [37] D. Moris, N. Machairas, D.I. Tsilimigras, A. Prodromidou, A. Ejaz, M. Weiss, N. Hasemaki, E. Felekouras, T.M. Pawlik, Systematic review of surgical and percutaneous irreversible electroporation in the treatment of locally advanced pancreatic cancer, *Ann. Surg. Oncol.* 26 (2019) 1657–1668.
- [38] S. Paiella, G. Butturini, I. Frigerio, R. Salvia, G. Armatura, M. Bacchion, M. Fontana, E. Martone, C. Bassi, Safety and feasibility of Irreversible Electroporation (IRE) in patients with locally advanced pancreatic cancer: results of a prospective study, *Dig. Surg.* 32 (2015) 90–97.
- [39] M.D. Kluger, I. Epelboym, B.A. Schrope, K. Mahendraraj, E.M. Hecht, J. Susman, J.L. Weintraub, J.A. Chabot, Single-institution experience with irreversible electroporation for T4 pancreatic cancer: first 50 patients, *Ann. Surg. Oncol.* 23 (2016) 1736–1743.

- [40] L. Lambert, J. Horejs, Z. Krska, D. Hoskovec, L. Petruzelka, T. Krechler, P. Kriz, J. Briza, Treatment of locally advanced pancreatic cancer by percutaneous and intraoperative irreversible electroporation: general hospital cancer center experience., *Neoplasma*. 63 (2016) 269–273.
- [41] C. Månsson, R. Brahmstaedt, A. Nilsson, P. Nygren, B.-M. Karlson, Percutaneous irreversible electroporation for treatment of locally advanced pancreatic cancer following chemotherapy or radiochemotherapy, *Eur. J. Surg. Oncol.* 42 (2016) 1401–1406.
- [42] D. Stillström, H. Nilsson, M. Jesse, M. Peterhans, E. Jonas, J. Freedman, A new technique for minimally invasive irreversible electroporation of tumors in the head and body of the pancreas, *Surg. Endosc.* 31 (2017) 1982–1985.
- [43] J.A. Vogel, S.J. Rombouts, T. de Rooij, O.M. van Delden, M.G. Dijkgraaf, T.M. van Gulik, J.E. van Hooft, H.W. van Laarhoven, R.C. Martin, A. Schoorlemmer, Induction chemotherapy followed by resection or irreversible electroporation in locally advanced pancreatic cancer (IMPALA): a prospective cohort study, *Ann. Surg. Oncol.* 24 (2017) 2734–2743.
- [44] M.P. Belfiore, F.M. Ronza, F. Romano, G. Pietro Ianniello, G. De Lucia, C. Gallo, C. Marsicano, T.L. Di Gennaro, G. Belfiore, Percutaneous CT-guided irreversible electroporation followed by chemotherapy as a novel neoadjuvant protocol in locally advanced pancreatic cancer: our preliminary experience, *Int. J. Surg.* 21 (2015) S34–S39.

- [45] G. Narayanan, P.J. Hosein, I.C. Beulaygue, T. Froud, H.J. Scheffer, S.R. Venkat, A.M. Echenique, E.C. Hevert, A.S. Livingstone, C.M. Rocha-Lima, Percutaneous image-guided irreversible electroporation for the treatment of unresectable, locally advanced pancreatic adenocarcinoma, *J. Vasc. Interv. Radiol.* 28 (2017) 342–348.
- [46] J. Spiliotis, N. Kopanakis, A. Terras, E. Efstathiou, Irreversible electroporation for Stage III locally advanced pancreatic cancer: Single-center experience., *J. BUON. Off. J. Balk. Union Oncol.* 23 (2018) 1203–1204.
- [47] K. Sugimoto, F. Moriyasu, Y. Kobayashi, K. Saito, H. Takeuchi, S. Ogawa, M. Ando, T. Sano, T. Mori, Y. Furuichi, Irreversible electroporation for nonthermal tumor ablation in patients with hepatocellular carcinoma: initial clinical experience in Japan, *Jpn. J. Radiol.* 33 (2015) 424–432.
- [48] E. Leen, J. Picard, J. Stebbing, M. Abel, T. Dhillon, H. Wasan, Percutaneous irreversible electroporation with systemic treatment for locally advanced pancreatic adenocarcinoma, *J. Gastrointest. Oncol.* 9 (2018) 275.
- [49] A.H. Ruarus, L.G.P.H. Vroomen, B. Geboers, E. van Veldhuisen, R.S. Puijk, S. Nieuwenhuizen, M.G. Besselink, B.M. Zonderhuis, G. Kazemier, T.D. de Gruijl, Percutaneous irreversible electroporation in locally advanced and recurrent pancreatic cancer (PANFIRE-2): a multicenter, prospective, single-arm, phase II study, *Radiology.* 294 (2020) 212–220.
- [50] M. Perera, N. Krishnananthan, U. Lindner, N. Lawrentschuk, An update on focal

- therapy for prostate cancer, *Nat. Rev. Urol.* 13 (2016) 641–653.
- [51] M. Valerio, Y. Cerantola, S.E. Eggener, H. Lepor, T.J. Polascik, A. Villers, M. Emberton, New and established technology in focal ablation of the prostate: a systematic review, *Eur. Urol.* 71 (2017) 17–34.
- [52] J.W. Davis, Re: Medium-term Oncologic Outcomes in a Large Cohort of Men Treated with Focal or Hemi-ablation Using High-intensity Focused Ultrasonography for Primary Localized Prostate Cancer, *Eur. Urol.* 77 (2020).
- [53] S. Guillaumier, M. Peters, M. Arya, N. Afzal, S. Charman, T. Dudderidge, F. Hosking-Jervis, R.G. Hindley, H. Lewi, N. McCartan, A multicentre study of 5-year outcomes following focal therapy in treating clinically significant nonmetastatic prostate cancer, *Eur. Urol.* 74 (2018) 422–429.
- [54] M.S. Mathew, A. Oto, MRI-guided focal therapy of prostate cancer, *Futur. Oncol.* 13 (2017) 537–549.
- [55] A. Blazevski, M.J. Scheltema, A. Amin, J.E. Thompson, N. Lawrentschuk, P.D. Stricker, Irreversible electroporation (IRE): a narrative review of the development of IRE from the laboratory to a prostate cancer treatment, (2019).
- [56] C.L. Dickinson, M. Valerio, H.U. Ahmed, A. Freeman, C. Allen, M. Emberton, 584 Early clinical experience of focal therapy for localised prostate cancer using irreversible electroporation, *Eur. Urol. Suppl.* 12 (2013) e584.  
[https://doi.org/10.1016/s1569-9056\(13\)61067-2](https://doi.org/10.1016/s1569-9056(13)61067-2).
- [57] M. Valerio, L. Dickinson, A. Ali, N. Ramachadran, I. Donaldson, N. McCartan, A.

- Freeman, H.U. Ahmed, M. Emberton, Nanoknife Electroporation Ablation Trial: A Prospective Development Study Investigating Focal Irreversible Electroporation for Localized Prostate Cancer, *J. Urol.* 197 (2017) 647–654. <https://doi.org/10.1016/j.juro.2016.09.091>.
- [58] E. Guenther, N. Klein, S. Zapf, S. Weil, C. Schlosser, B. Rubinsky, M.K. Stehling, Prostate cancer treatment with Irreversible Electroporation (IRE): Safety, efficacy and clinical experience in 471 treatments, *PLoS One.* 14 (2019) 1–15. <https://doi.org/10.1371/journal.pone.0215093>.
- [59] M. Valerio, P.D. Stricker, H.U. Ahmed, L. Dickinson, L. Ponsky, R. Shnier, C. Allen, M. Emberton, Initial assessment of safety and clinical feasibility of irreversible electroporation in the focal treatment of prostate cancer, *Prostate Cancer Prostatic Dis.* 17 (2014) 343–347. <https://doi.org/10.1038/pcan.2014.33>.
- [60] R. Ganzer, V.K.A. Arthanareeswaran, H.U. Ahmed, A. Cestari, P. Rischmann, G. Salomon, D. Teber, E. Liatsikos, J.U. Stolzenburg, E. Barret, Which technology to select for primary focal treatment of prostate cancer?-European Section of Urotechnology (ESUT) position statement, *Prostate Cancer Prostatic Dis.* 21 (2018) 175–186. <https://doi.org/10.1038/s41391-018-0042-0>.
- [61] F. Ting, M. Tran, M. Böhm, A. Siriwardana, P.J. Van Leeuwen, A.M. Haynes, W. Delprado, R. Shnier, P.D. Stricker, Focal irreversible electroporation for prostate cancer: Functional outcomes and short-term oncological control, *Prostate Cancer Prostatic Dis.* 19 (2016) 46–52. <https://doi.org/10.1038/pcan.2015.47>.

- [62] M. Valerio, L. Dickinson, A. Ali, N. Ramachandran, I. Donaldson, A. Freeman, H.U. Ahmed, M. Emberton, A prospective development study investigating focal irreversible electroporation in men with localised prostate cancer: Nanoknife electroporation ablation trial (NEAT), *Contemp. Clin. Trials*. 39 (2014) 57–65. <https://doi.org/10.1016/j.cct.2014.07.006>.
- [63] G. Onik, P. Mikus, B. Rubinsky, Irreversible electroporation: Implications for prostate ablation, *Technol. Cancer Res. Treat.* 6 (2007) 295–300. <https://doi.org/10.1177/153303460700600405>.
- [64] R.E. Neal, J.L. Millar, H. Kavnoudias, P. Royce, F. Rosenfeldt, A. Pham, R. Smith, R. V. Davalos, K.R. Thomson, In vivo characterization and numerical simulation of prostate properties for non-thermal irreversible electroporation ablation, *Prostate*. 74 (2014) 458–468. <https://doi.org/10.1002/pros.22760>.
- [65] W. van den Bos, D.M. de Bruin, R.R. Jurhill, C.D. Savci-Heijink, B.G. Muller, I.M. Varkarakis, A. Skolarikos, P.J. Zondervan, M.P. Laguna-Pes, H. Wijkstra, T.M. de Reijke, J.J.M.C.H. de la Rosette, The correlation between the electrode configuration and histopathology of irreversible electroporation ablations in prostate cancer patients, *World J. Urol.* 34 (2016) 657–664. <https://doi.org/10.1007/s00345-015-1661-x>.
- [66] M. Valerio, L. Dickinson, A. Ali, N. Ramachadran, I. Donaldson, N. Mccartan, A. Freeman, H.U. Ahmed, M. Emberton, Nanoknife Electroporation Ablation Trial: A Prospective Development Study Investigating Focal Irreversible Electroporation for Localized Prostate Cancer, *J. Urol.* 197 (2017) 647–654.

<https://doi.org/10.1016/j.juro.2016.09.091>.

- [67] J.M. Llovet, R.K. Kelley, A. Villanueva, A.G. Singal, E. Pikarsky, S. Roayaie, R. Lencioni, K. Koike, J. Zucman-Rossi, R.S. Finn, Hepatocellular carcinoma., *Nat Rev Dis Prim.* (2021) 6.
- [68] W.H. Organization, Projections of mortality and causes of death, 2016 to 2060, (2016).
- [69] A. Forner, A.J. Hessheimer, M.I. Real, J. Bruix, Treatment of hepatocellular carcinoma, *Crit. Rev. Oncol. Hematol.* 60 (2006) 89–98.
- [70] R. Lencioni, L. Crocetti, Local-regional treatment of hepatocellular carcinoma, *Radiology.* 262 (2012) 43–58.
- [71] P.R. Galle, A. Forner, J.M. Llovet, V. Mazzaferro, F. Piscaglia, J.L. Raoul, Electronic address: easloffice@ easloffice. eu; European Association for the Study of the Liver. EASL Clinical Practice Guidelines: management of hepatocellular carcinoma, *J Hepatol.* 69 (2018) 182–236.
- [72] A. Zimmerman, D. Grand, K.P. Charpentier, Irreversible electroporation of hepatocellular carcinoma: patient selection and perspectives, *J. Hepatocell. Carcinoma.* 4 (2017) 49.
- [73] G. Narayanan, T. Froud, K. Lo, K.J. Barbery, E. Perez-Rojas, J. Yrizarry, Pain analysis in patients with hepatocellular carcinoma: Irreversible electroporation versus radiofrequency ablation - Initial observations, *Cardiovasc. Intervent. Radiol.* 36 (2013) 176–182. <https://doi.org/10.1007/s00270-012-0426-9>.

- [74] S.A. Padia, G.E. Johnson, R.S. Yeung, J.O. Park, D.S. Hippe, M.J. Kogut, Irreversible electroporation in patients with hepatocellular carcinoma: Immediate versus delayed findings at mr imaging, *Radiology*. 278 (2016) 285–294. <https://doi.org/10.1148/radiol.2015150031>.
- [75] W. Cheung, H. Kavnoudias, S. Roberts, B. Szkandera, W. Kemp, K.R. Thomson, Irreversible electroporation for unresectable hepatocellular carcinoma: Initial experience and review of safety and outcomes, *Technol. Cancer Res. Treat.* 12 (2013) 233–241. <https://doi.org/10.7785/tcrt.2012.500317>.
- [76] W. Cheung, H. Kavnoudias, S. Roberts, B. Szkandera, W. Kemp, K.R. Thomson, Irreversible electroporation for unresectable hepatocellular carcinoma: initial experience and review of safety and outcomes, *Technol. Cancer Res. Treat.* 12 (2013) 233–241.
- [77] P. Philips, D. Hays, R.C.G. Martin, Irreversible electroporation ablation (IRE) of unresectable soft tissue tumors: Learning curve evaluation in the first 150 patients treated, *PLoS One*. 8 (2013) 1–9. <https://doi.org/10.1371/journal.pone.0076260>.
- [78] R. Cannon, S. Ellis, D. Hayes, G. Narayanan, R.C.G. Martin, Safety and early efficacy of irreversible electroporation for hepatic tumors in proximity to vital structures, *J. Surg. Oncol.* 107 (2013) 544–549. <https://doi.org/10.1002/jso.23280>.
- [79] M. Dollinger, L.P. Beyer, M. Haimerl, C. Niessen, E.M. Jung, F. Zeman, C. Stroszczynski, P. Wiggermann, Adverse effects of irreversible electroporation of malignant liver tumors under CT fluoroscopic guidance: A single-center



experience, *Diagnostic Interv. Radiol.* 21 (2015) 471–475.

<https://doi.org/10.5152/dir.2015.14442>.

- [80] B. Kos, P. Voigt, D. Miklavcic, M. Moche, Careful treatment planning enables safe ablation of liver tumors adjacent to major blood vessels by percutaneous irreversible electroporation (IRE), *Radiol. Oncol.* 49 (2015) 234–241.

<https://doi.org/10.1515/raon-2015-0031>.

- [81] T. Froud, S.R. Venkat, K.J. Barbery, A. Gunjan, G. Narayanan, Liver Function Tests Following Irreversible Electroporation of Liver Tumors: Experience in 174 Procedures, *Tech. Vasc. Interv. Radiol.* 18 (2015) 140–146.

<https://doi.org/10.1053/j.tvir.2015.06.004>.

- [82] A. Eller, A. Schmid, J. Schmidt, M. May, M. Brand, M. Saake, M. Uder, M. Lell, Local Control of Perivascular Malignant Liver Lesions Using Percutaneous Irreversible Electroporation: Initial Experiences, *Cardiovasc. Intervent. Radiol.* 38 (2015) 152–159. <https://doi.org/10.1007/s00270-014-0898-x>.

- [83] C. Niessen, L.P. Beyer, B. Pregler, M. Dollinger, B. Trabold, H.J. Schlitt, E.M. Jung, C. Stroszczynski, P. Wiggermann, Percutaneous ablation of hepatic tumors using irreversible electroporation: A prospective safety and midterm efficacy study in 34 patients, *J. Vasc. Interv. Radiol.* 27 (2016) 480–486.

<https://doi.org/10.1016/j.jvir.2015.12.025>.

- [84] L.P. Beyer, B. Pregler, K. Michalik, C. Niessen, M. Dollinger, M. Müller, H.J. Schlitt, C. Stroszczynski, P. Wiggermann, Evaluation of a robotic system for

- irreversible electroporation (IRE) of malignant liver tumors: initial results, *Int. J. Comput. Assist. Radiol. Surg.* 12 (2017) 803–809.
- [85] B. Rubinsky, G. Onik, P. Mikus, Irreversible electroporation: a new ablation modality—clinical implications, *Technol. Cancer Res. Treat.* 6 (2007) 37–48.
- [86] L. Miller, J. Leor, B. Rubinsky, Cancer cells ablation with irreversible electroporation, *Technol. Cancer Res. Treat.* 4 (2005) 699–705.
- [87] N. Iida, Y. Nakamoto, T. Baba, H. Nakagawa, E. Mizukoshi, M. Naito, N. Mukaida, S. Kaneko, Antitumor effect after radiofrequency ablation of murine hepatoma is augmented by an active variant of CC chemokine ligand 3/macrophage inflammatory protein-1 $\alpha$ , *Cancer Res.* 70 (2010) 6556–6565.
- [88] C.L. Brace, J.L. Hinshaw, M.G. Lubner, Thermal ablation for the treatment of abdominal tumors, *JoVE (Journal Vis. Exp.)* (2011) e2596.
- [89] M. Phillips, E. Maor, B. Rubinsky, Nonthermal irreversible electroporation for tissue decellularization, *J. Biomech. Eng.* 132 (2010).
- [90] B. Rubinsky, Irreversible electroporation in medicine, *Technol. Cancer Res. Treat.* 6 (2007) 255–259. <https://doi.org/10.1177/153303460700600401>.
- [91] E. Maor, A. Ivorra, D. Ph, J. Leor, B. Rubinsky, D. Ph, The Effect of Irreversible Electroporation on Blood Vessels, 6 (2007) 307–312. <https://doi.org/10.1177/153303460700600407>.
- [92] H.J. Scheffer, K. Nielsen, M.C. De Jong, A.A.J.M. Van Tilborg, J.M. Vieveen, A.

- Bouwman, S. Meijer, C. Van Kuijk, P. Van Den Tol, M.R. Meijerink, Irreversible electroporation for nonthermal tumor ablation in the clinical setting: A systematic review of safety and efficacy, *J. Vasc. Interv. Radiol.* 25 (2014) 997–1011.  
<https://doi.org/10.1016/j.jvir.2014.01.028>.
- [93] S.P. Bhonsle, C.B. Arena, D.C. Sweeney, R. V Davalos, Mitigation of impedance changes due to electroporation therapy using bursts of high-frequency bipolar pulses, *Biomed. Eng. Online.* 14 (2015) S3.
- [94] L.G. Campana, F. Dughiero, M. Forzan, C.R. Rossi, E. Sieni, A prototype of a flexible grid electrode to treat widespread superficial tumors by means of Electrochemotherapy, *Radiol. Oncol.* 50 (2016) 49–57.  
<https://doi.org/10.1515/raon-2016-0013>.
- [95] S. Dong, C. Yao, Y. Zhao, Y. Lv, H. Liu, Parameters optimization of bipolar high frequency pulses on tissue ablation and inhibiting muscle contraction, *IEEE Trans. Dielectr. Electr. Insul.* 25 (2018) 207–216.  
<https://doi.org/10.1109/TDEI.2018.006303>.
- [96] Y. Lv, Y. Zhang, B. Rubinsky, Molecular and histological study on the effects of electrolytic electroporation on the liver, *Bioelectrochemistry.* 125 (2019) 79–89.  
<https://doi.org/10.1016/j.bioelechem.2018.09.007>.
- [97] Y. Lv, C. Yao, B. Rubinsky, A Conceivable Mechanism Responsible for the Synergy of High and Low Voltage Irreversible Electroporation Pulses, *Ann. Biomed. Eng.* 47 (2019) 1552–1563. <https://doi.org/10.1007/s10439-019-02258->

5.

- [98] P. Muneta, Enzymatic blackening in potatoes: Influence of pH on dopachrome oxidation, *Am. Potato J.* 54 (1977) 387–393.
- [99] Y. Zhao, H. Liu, S.P. Bhonsle, Y. Wang, R. V. Davalos, C. Yao, Ablation outcome of irreversible electroporation on potato monitored by impedance spectrum under multi-electrode system, *Biomed. Eng. Online.* 17 (2018) 1–13. <https://doi.org/10.1186/s12938-018-0562-9>.
- [100] A. Barabasch, M. Distelmaier, P. Heil, N.A. Krämer, C.K. Kuhl, P. Bruners, Magnetic Resonance Imaging Findings after Percutaneous Irreversible Electroporation of Liver Metastases: A Systematic Longitudinal Study, *Invest. Radiol.* 52 (2017) 23–29. <https://doi.org/10.1097/RLI.0000000000000301>.
- [101] Q. Castellví, J. Banús, A. Ivorra, 3D assessment of irreversible electroporation treatments in vegetal models, *IFMBE Proc.* 53 (2016) 294–297. [https://doi.org/10.1007/978-981-287-817-5\\_65](https://doi.org/10.1007/978-981-287-817-5_65).
- [102] J. NORDMANN, R. NORDMANN, O. GAUCHERY, [Determination of the dehydrogenase activity of mitochondria by means of 2,3,5-triphenyltetrazolium chloride], *Bull. Soc. Chim. Biol. (Paris)*. 33 (1951) 1826–1836.
- [103] L.E. Towill, P. Mazur, Studies on the reduction of 2,3,5-triphenyltetrazolium chloride as a viability assay for plant tissue cultures, *Can. J. Bot.* 53 (1975) 1097–1102. <https://doi.org/10.1139/b75-129>.
- [104] K.P. Charpentier, F. Wolf, L. Noble, B. Winn, M. Resnick, D.E. Dupuy,

- Irreversible electroporation of the pancreas in swine: A pilot study, *Hpb*. 12 (2010) 348–351. <https://doi.org/10.1111/j.1477-2574.2010.00174.x>.
- [105] F. Faridnia, D.J. Burritt, P.J. Bremer, I. Oey, Innovative approach to determine the effect of pulsed electric fields on the microstructure of whole potato tubers: Use of cell viability, microscopic images and ionic leakage measurements, *Food Res. Int.* 77 (2015) 556–564. <https://doi.org/10.1016/j.foodres.2015.08.028>.
- [106] A. Mohammadzadeh, P. Farnia, K. Ghazvini, M. Behdani, T. Rashed, J. Ghanaat, Rapid and low-cost colorimetric method using 2,3,5-triphenyltetrazolium chloride for detection of multidrug-resistant *Mycobacterium tuberculosis*, *J. Med. Microbiol.* 55 (2006) 1657–1659. <https://doi.org/https://doi.org/10.1099/jmm.0.46442-0>.
- [107] C.K. Sung, H.B. Kim, J.H. Jung, K.Y. Baik, K.W. Moon, H. Kim, J. Yi, J.H. Chung, Histological and Mathematical Analysis of the Irreversibly Electroporated Liver Tissue, 16 (2017) 488–496. <https://doi.org/10.1177/1533034616640642>.
- [108] G. Merola, R. Fusco, E. Di Bernardo, V. D’alessio, F. Izzo, V. Granata, D. Contartese, M. Cadossi, A. Audenino, G.P. Gallo, Design and characterization of a minimally invasive bipolar electrode for electroporation, *Biology (Basel)*. 9 (2020) 1–24. <https://doi.org/10.3390/biology9090303>.
- [109] J.A. Berkenbrock, G. Brasil Pintarelli, A. de Castro Antônio Júnior, D.O.H. Suzuki, Verification of Electroporation Models Using the Potato Tuber as In Vitro Simulation, *J. Med. Biol. Eng.* 39 (2019) 224–229.

<https://doi.org/10.1007/s40846-018-0408-8>.

- [110] H.-B. Kim, C.-K. Sung, K.Y. Baik, K.-W. Moon, H.-S. Kim, J.-H. Yi, J.-H. Jung, M.-H. Moon, O.-K. Choi, Changes of apoptosis in tumor tissues with time after irreversible electroporation, *Biochem. Biophys. Res. Commun.* 435 (2013) 651–656.
- [111] J.M. Lee, H.S. Choi, H.J. Chun, E.S. Kim, B. Keum, Y.S. Seo, Y.T. Jeon, H.S. Lee, S.H. Um, C.D. Kim, EUS-guided irreversible electroporation using endoscopic needle-electrode in porcine pancreas, *Surg. Endosc.* 33 (2019) 658–662.
- [112] T. Miklovic, E.L. Latouche, M.R. DeWitt, R. V. Davalos, M.B. Sano, A Comprehensive Characterization of Parameters Affecting High-Frequency Irreversible Electroporation Lesions, *Ann. Biomed. Eng.* 45 (2017) 2524–2534. <https://doi.org/10.1007/s10439-017-1889-2>.
- [113] G. Saulis, M.S. Venslauskas, J. Naktinis, Kinetics of pore resealing in cell membranes after electroporation, *J. Electroanal. Chem. Interfacial Electrochem.* 321 (1991) 1–13. [https://doi.org/10.1016/0022-0728\(91\)85564-6](https://doi.org/10.1016/0022-0728(91)85564-6).
- [114] E. Kun, L.G. Abood, Colorimetric Estimation of Succinic Dehydrogenase by Triphenyltetrazolium Chloride Published by : American Association for the Advancement of Science Stable URL : <https://www.jstor.org/stable/1676167> American Association for the Advancement of Science is , 109 (1949) 144–146.
- [115] C.N. Joshi, S.K. Jain, P.S.R. Murthy, An optimized triphenyltetrazolium chloride

method for identification of cerebral infarcts, *Brain Res. Protoc.* 13 (2004) 11–17.

<https://doi.org/https://doi.org/10.1016/j.brainresprot.2003.12.001>.

- [116] A.R. Deipolyi, A. Golberg, M.L. Yarmush, R.S. Arellano, R. Oklu, Irreversible electroporation: evolution of a laboratory technique in interventional oncology, *Diagnostic Interv. Radiol.* 20 (2014) 147.
- [117] T. Kotnik, P. Kramar, G. Pucihar, D. Miklavcic, M. Tarek, Cell membrane electroporation-Part 1: The phenomenon, *IEEE Electr. Insul. Mag.* 28 (2012) 14–23.
- [118] B. López-Alonso, A. Hernáez, H. Sarnago, A. Naval, A. Güemes, C. Junquera, J.M. Burdío, T. Castiella, E. Monleón, J. Gracia-Llanes, Histopathological and ultrastructural changes after electroporation in pig liver using parallel-plate electrodes and high-performance generator, *Sci. Rep.* 9 (2019) 1–12.
- [119] S. Bensalem, D. Pareau, B. Cinquin, O. Français, B. Le Pioufle, F. Lopes, Impact of pulsed electric fields and mechanical compressions on the permeability and structure of *Chlamydomonas reinhardtii* cells, *Sci. Rep.* 10 (2020) 1–11.
- [120] Y. Zhen, M. Radulovic, M. Vietri, H. Stenmark, Sealing holes in cellular membranes, *EMBO J.* (2021) e106922.
- [121] Y. Zhao, S. Bhonsle, S. Dong, Y. Lv, H. Liu, A. Safaai-Jazi, R. V. Davalos, C. Yao, Characterization of conductivity changes during high-frequency irreversible electroporation for treatment planning, *IEEE Trans. Biomed. Eng.* 65 (2018) 1810–1819. <https://doi.org/10.1109/TBME.2017.2778101>.

- [122] A. Baah-Dwomoh, A. Rolong, P. Gatenholm, R. V. Davalos, The feasibility of using irreversible electroporation to introduce pores in bacterial cellulose scaffolds for tissue engineering, *Appl. Microbiol. Biotechnol.* 99 (2015) 4785–4794. <https://doi.org/10.1007/s00253-015-6445-0>.
- [123] G. Pucihar, L.M. Mir, D. Miklavčič, The effect of pulse repetition frequency on the uptake into electropermeabilized cells in vitro with possible applications in electrochemotherapy, *Bioelectrochemistry.* 57 (2002) 167–172. [https://doi.org/10.1016/S1567-5394\(02\)00116-0](https://doi.org/10.1016/S1567-5394(02)00116-0).
- [124] B. Rubinsky, *Irreversible electroporation*, Springer Science & Business Media, (2009), p.33
- [125] D. Miklavčič, *Handbook of electroporation*, (2017), p.358
- [126] D.E. Clapham, Calcium signaling, *Cell.* 131 (2007) 1047–1058.
- [127] N.S.M. Yusof, E. Supriyanto, D.E.O. Dewi, Investigation of electrochemical characterization of agarose gel for model of human head correlated to lightning currents, in: 2016 Int. Conf. Robot. Autom. Sci., IEEE, 2016: pp. 1–6.
- [128] N. Soto-Reyes, A.L. Temis-Pérez, A. López-Malo, R. Rojas-Laguna, M.E. Sosa-Morales, Effects of shape and size of agar gels on heating uniformity during pulsed microwave treatment, *J. Food Sci.* 80 (2015) E1021–E1025.
- [129] H. Kato, K. Yoshimura, M. Kuroda, A. Yoshida, K. Hanamoto, S. Kawasaki, K. Shibuya, Y. Yamamoto, M. Tsunoda, M. Takemoto, Development of a phantom compatible for MRI and hyperthermia using carrageenan gel—relationship



- between dielectric properties and NaCl concentration, *Int. J. Hyperth.* 20 (2004) 529–538.
- [130] S. Oh, C.M. Collins, Experimental Temperature and Specific Absorption Rate Mapping Using MRI in a Transmit-receive Head Coil at 3.0 T, in: *Prog. Electromagn. Res. Symp. Abstr.*, 2008.
- [131] D.A. Siegel, M.E. O’Neil, T.B. Richards, N.F. Dowling, H.K. Weir, Prostate cancer incidence and survival, by stage and race/ethnicity—United States, 2001–2017, *Morb. Mortal. Wkly. Rep.* 69 (2020) 1473.
- [132] A. Bill-Axelson, L. Holmberg, H. Garmo, J.R. Rider, K. Taari, C. Busch, S. Nordling, M. Häggman, S.-O. Andersson, A. Spångberg, Radical prostatectomy or watchful waiting in early prostate cancer, *N. Engl. J. Med.* 370 (2014) 932–942.
- [133] T.J. Wilt, M.K. Brawer, K.M. Jones, M.J. Barry, W.J. Aronson, S. Fox, J.R. Gingrich, J.T. Wei, P. Gilhooly, B.M. Grob, Radical prostatectomy versus observation for localized prostate cancer, *N Engl J Med.* 367 (2012) 203–213.
- [134] M.G. Sanda, R.L. Dunn, J. Michalski, H.M. Sandler, L. Northouse, L. Hembroff, X. Lin, T.K. Greenfield, M.S. Litwin, C.S. Saigal, Quality of life and satisfaction with outcome among prostate-cancer survivors, *N. Engl. J. Med.* 358 (2008) 1250–1261.
- [135] L. Cao, Z. Yang, L. Qi, M. Chen, Robot-assisted and laparoscopic vs open radical prostatectomy in clinically localized prostate cancer: perioperative, functional,

and oncological outcomes: a systematic review and meta-analysis, *Medicine* (Baltimore). 98 (2019).

- [136] M.J. Resnick, T. Koyama, K.-H. Fan, P.C. Albertsen, M. Goodman, A.S. Hamilton, R.M. Hoffman, A.L. Potosky, J.L. Stanford, A.M. Stroup, Long-term functional outcomes after treatment for localized prostate cancer, *N Engl J Med.* 368 (2013) 436–445.
- [137] M. Ahdoot, A.H. Lebastchi, B. Turkbey, B. Wood, P.A. Pinto, Contemporary treatments in prostate cancer focal therapy, *Curr. Opin. Oncol.* 31 (2019) 200.
- [138] V. Kasivisvanathan, M. Emberton, H.U. Ahmed, Focal therapy for prostate cancer: rationale and treatment opportunities, *Clin. Oncol.* 25 (2013) 461–473.
- [139] A.T.U. Din, Irreversible Electroporation for liver tumors: A review of literature, *Cureus.* 11 (2019).
- [140] G. Narayanan, Irreversible electroporation, in: *Semin. Intervent. Radiol.*, Thieme Medical Publishers, 2015: pp. 349–355.
- [141] A. Karagiannis, J. Varkarakis, Irreversible Electroporation for the Ablation of Prostate Cancer, *Curr. Urol. Rep.* 20 (2019) 63. <https://doi.org/10.1007/s11934-019-0929-x>.
- [142] J. Rubinsky, G. Onik, P. Mikus, B. Rubinsky, Optimal Parameters for the Destruction of Prostate Cancer Using Irreversible Electroporation, *J. Urol.* 180 (2008) 2668–2674. <https://doi.org/10.1016/j.juro.2008.08.003>.

- [143] A. Deodhar, T. Dickfeld, G.W. Single, W.C. Hamilton Jr, R.H. Thornton, C.T. Sofocleous, M. Maybody, M. Gónen, B. Rubinsky, S.B. Solomon, Irreversible electroporation near the heart: ventricular arrhythmias can be prevented with ECG synchronization, *Am. J. Roentgenol.* 196 (2011) W330–W335.
- [144] B. Lim, H.B. Kim, S. Jeong, S.H. Kim, J.M. Kang, Y. Park, D.S. Won, J.W. Kim, D.S. Ryu, Y. Kim, J.H. Park, C.S. Kim, Novel platinum bipolar electrode for irreversible electroporation in prostate cancer : preclinical study in the beagle prostate, *Sci. Rep.* (2021) 1–9. <https://doi.org/10.1038/s41598-021-96734-5>.
- [145] J.A. Cerqueira, W.A.Z. Restan, M.G. Fonseca, L.A. Catananti, M.L.M. de Almeida, W.H.F. Junior, G.T. Pereira, A.C. Carciofi, G. de Camargo Ferraz, Intense exercise and endurance-training program influence serum kinetics of muscle and cardiac biomarkers in dogs, *Res. Vet. Sci.* 121 (2018) 31–39. <https://doi.org/10.1016/j.rvsc.2018.10.004>.
- [146] Leading article Necrosis and apoptosis in the gastrointestinal tract, *Nature.* (1995) 165–167.
- [147] H. Sung, J. Ferlay, R.L. Siegel, M. Laversanne, I. Soerjomataram, A. Jemal, F. Bray, Global Cancer Statistics 2020: GLOBOCAN Estimates of Incidence and Mortality Worldwide for 36 Cancers in 185 Countries, *CA. Cancer J. Clin.* 71 (2021) 209–249. <https://doi.org/10.3322/caac.21660>.
- [148] Z. Qin, J. Jiang, G. Long, B. Lindgren, J.C. Bischof, Irreversible electroporation: An in vivo study with dorsal skin fold chamber, *Ann. Biomed. Eng.* 41 (2013)

619–629. <https://doi.org/10.1007/s10439-012-0686-1>.

- [149] P.A. Garcia, J.H. Rossmeisl, R.E. Neal, T.L. Ellis, R. V Davalos, A parametric study delineating irreversible electroporation from thermal damage based on a minimally invasive intracranial procedure, *Biomed. Eng. Online*. 10 (2011) 1–22.